

# Looking into the hearts of Bok globules: MM and submm continuum images of isolated star-forming cores

R. Launhardt

*Max Planck Institute for Astronomy, Königstuhl 17, D-69117 Heidelberg, Germany*

rl@mpia.de

and

D. Nutter, D. Ward-Thompson

*School of Physics and Astronomy, Cardiff University, Queens Buildings, The Parade, Cardiff, CF24 3AA, UK*

and

T. L. Bourke

*Harvard-Smithsonian Center for Astrophysics, 60 Garden Street, Cambridge, MA 02138, USA*

and

Th. Henning, T. Khanzadyan<sup>1</sup>, M. Schmalzl, S. Wolf<sup>2</sup>

*Max Planck Institute for Astronomy, Königstuhl 17, D-69117 Heidelberg, Germany*

and

R. Zylka

*Institut de Radio Astronomie Millimétrique, 300 Rue de la Piscine, Domaine Universitaire, 38406 Saint Martin d'Hères, France*

## ABSTRACT

We present the results of a comprehensive infrared, submillimetre, and millimetre continuum emission study of isolated low-mass star-forming cores in 32 Bok globules, with the aim to investigate the process of star formation in these regions. The submillimetre and millimetre dust continuum emission maps together with the spectral energy distributions are used to model and derive the physical properties of the star-forming cores, such as luminosities, sizes, masses, densities, etc. Comparisons with ground-based near-infrared and space-based mid and far-infrared images from Spitzer are used to reveal the stellar content of the Bok globules, association of embedded young stellar objects with the submm dust cores, and the evolutionary stages of the individual sources. Submm dust continuum emission was detected in 26 out of the 32 globule cores observed. For 18 globules with detected (sub)mm cores we derive evolutionary stages and physical parameters of the embedded sources. We identify nine starless cores, most of which are presumably prestellar, nine Class 0 protostars, and twelve Class I YSOs. Specific source properties like bolometric temperature, core size, and central densities are discussed as function of evolutionary stage. We find that at least two thirds (16 out of 24) of the star-forming globules studied here show evidence of forming multiple stars on scales between 1,000 and 50,000 AU. However, we also find that most of these small protostar and star groups are comprised of sources with different evolutionary stages, suggesting a picture of slow and sequential star formation in isolated globules.

*Subject headings:* dust, extinction — infrared: stars — ISM: clouds — stars: formation — submillimeter: ISM

## 1. Introduction

Different aspects of star formation can be studied on different size scales and in different environments. The large-scale distribution of star-forming regions and the relation between molecular cloud life cycles, galactic spiral density waves, and star formation can be studied by observing nearby galaxies (e.g. Brouillet et al. 1998; Scheepmaker et al. 2009). The stellar initial mass function (IMF), which is needed to interpret these data, is usually derived from rich young stellar clusters in our own Galaxy (e.g. Kroupa 2002; Chabrier 2003). Dense star-forming dark cloud complexes such as the Orion and Ophiuchus molecular clouds are the places to study the relation between the molecular core mass spectrum (CMF) and the interstellar IMF (e.g. Motte et al. 1998; Nutter & Ward-Thompson 2007; Simpson et al. 2008; Goodwin et al. 2008).

Nearby and more isolated star-forming cores, such as Bok globules, are the best places to study in detail the initial properties of individual star-forming cores, their chemical evolution, kinematic structure, and the physics of their collapse and fragmentation (e.g., Clemens & Barvainis 1988; Bourke et al. 1995a; Launhardt & Henning 1997; Launhardt et al. 1997; Henning & Launhardt 1998; Ward-Thompson et al. 2007; Stutz et al. 2008). Bok globules are small, simply-structured, relatively isolated, opaque molecular clouds that often contain only one or two star-forming core. They are often not completely isolated, but reside in the filamentary outskirts of larger dark cloud complexes (Launhardt & Henning 1997), a fact that may tell something about their origin. With their size, mass, densities, etc., Bok globules resemble small clumps in larger molecular clouds (cf. Bergin & Tafalla 2007), only that they lack the surrounding cloud. Table 1 summarizes the average general properties of typical Bok globules and their star-forming cores.

Although they are the most simple star-forming molecular clouds, many globules deviate considerably from spherical geometry. They are often cometary or irregularly shaped. The dense star-forming cores are not always located at the center of the globule, but in cometary-shaped globules are often located closer

to the sharper rim at the “head” side (e.g., Launhardt 1996). Similarly, pre-stellar cores, which are the earliest stage of star formation (Ward-Thompson et al. 1994, 2007) often appear to be fragmentary and filamentary. However, the protostellar cores and envelopes of the more evolved Class 0 & I YSOs (Lada 1987; André et al. 1993) are more spherically symmetric, which can be understood as a result of the gravitational collapse of the inner dense  $R \sim 5000$  AU region. Many of these isolated cores were found to be the sources of bipolar molecular outflows, indicating the presence of embedded protostars (e.g., Yun & Clemens 1994b; Ward-Thompson et al. 1995; Bontemps et al. 1996).

In order to investigate the star-forming potential and evolutionary stages of Bok globules in the solar neighbourhood, we had surveyed a large number of globules for signs of star-forming cores, using as tracers, e.g., the mm dust continuum emission (Launhardt 1996; Launhardt & Henning 1997; Henning & Launhardt 1998; Launhardt et al. 1998),  $\text{NH}_3$  (Bourke et al. 1995b) or CS line emission (Launhardt et al. 1998).

In this paper we present a submillimetre and millimetre – hereafter (sub)mm – continuum study of 32 Bok globules, which were identified from these previous surveys as promising candidates for globules with currently ongoing star formation. The (sub)mm maps are complemented by deep near-infrared (NIR) images and NIR to mm spectral energy distributions (SEDs). In Sect. 2, we describe the observations and data reduction. In Sect. 3, we present the NIR and (sub)mm images, SEDs, and results on multiplicity, physical parameters, and evolutionary stages. In Sect. 4, we discuss in particular the source properties as function of evolutionary stage and the results on multiplicity. In Sect. 5, we describe and discuss the individual globules, and Sect. 6 summarizes the main results of this study.

## 2. Observations and data reduction

A total of 32 Bok globules were studied using a combination of NIR and (sub)mm continuum observations. Coordinates, distances, and observation summary of these sources are given in Table 2. Although many of the globules appear in different catalogues and thus often have several names assigned, we use throughout this paper the CB name and number introduced by Clemens & Barvainis (1988) for northern sources, and the BHR name and number introduced by

<sup>1</sup>Dept. Experimental Physics, National University of Ireland Galway, Galway, Ireland

<sup>2</sup>University of Kiel, Institute of Theoretical Physics and Astrophysics, Leibnizstrasse 15, 24098 Kiel, Germany

Bourke et al. (1995a) for southern sources.

## 2.1. (Sub)millimetre continuum observations

Submillimetre and millimetre dust continuum observations at  $450\mu\text{m}$ ,  $850\mu\text{m}$ , and  $1.3\text{ mm}$  were performed during several observing runs between 1994 and 2002 at the 15-m James Clerk Maxwell Telescope<sup>1</sup> (JCMT) on Mauna Kea, Hawaii, at the 30-m Institut de Radio Astronomie Millimetrique (IRAM) telescope on Pico Veleta, Spain, and at the 15-m Swedish-ESO Submillimetre Telescope (SEST) on La Silla, Chile.

Observations at  $1.3\text{ mm}$  of the northern sources were carried out during four observing runs between April 1994 and March 1997 using the MPIFR 7-channel (1994–95) and 19-channel (1996–97) bolometer arrays (Kreysa et al. 1998) at the IRAM 30-m telescope. The maps were obtained with the standard double-beam technique described by Emerson et al. (1979). The telescope was scanned continuously at  $4''/\text{sec}$  in azimuth while the wobbling secondary, operating at  $2\text{ Hz}$  with a chopper throw of  $30''$  along the scan direction, generated the dual beams. Scan lengths and map sizes were adapted to source sizes to provide sufficient baseline for background determination. Individual scan maps of a source, which were later combined, were obtained at different hour angles in order to reduce scanning effects.

Observations at  $1.3\text{ mm}$  of southern sources were carried out in September and November 2002 at the Swedish/ESO Submillimetre Telescope (SEST) at La Silla in Chile, using the 37-channel bolometer array SIMBA (SEST Imaging Bolometer Array). Since SIMBA was used without a wobbling secondary mirror, several fast-scanning maps (at  $80''/\text{sec}$ ) were obtained for each field at different hour angles to reduce scanning effects. Source BHR 71 was already observed in 1995 with the MPIFR single-channel bolometer at SEST (Bourke et al. 1997). Individual maps at different hour angles were obtained with the same double-beam mapping technique used at the 30-m telescope, but by employing the SEST focal plane chopper.

The submillimetre observations were carried out during three observing runs between August 1997 and September 2001 using the Submillimetre Common User Bolometer Array (SCUBA) on the JCMT. The observations were conducted simultaneously at  $850$

and  $450\mu\text{m}$  using a 64-point jiggle pattern to create fully sampled maps of  $2.3'$  diameter fields around the coordinate centers (for more details, see Holland et al. 1999). Time-dependent variations in the sky emission were removed by chopping the secondary mirror at  $7.8\text{ Hz}$  with a chop throw of  $120''$  in azimuth. During the 2000 and 2001 observations, we also obtained  $850\mu\text{m}$  polarization maps of six globule cores (see Henning et al. 2001; Wolf et al. 2003). In addition, the JCMT archive, operated by the Canadian Astronomy Data Centre (CADC), was searched for additional data for the sources observed at  $1.3\text{ mm}$ . One of the sources (CB224) was observed using SCUBA in the scan-mapping mode. In this observing mode, the array is rastered across the sky to produce a rectangular map several arcminutes in extent. Variations in sky emission are again removed by chopping the secondary mirror, though six chop configurations are used, chopping in  $30$ ,  $44$  and  $68''$  in both RA and Dec (Jenness et al. 1998).

During all observing runs, the atmospheric transmission was determined using the ‘skydip’ method, which were performed every 2–3 hours. At the JCMT, we also used polynomial fits to the  $225\text{ GHz}$  atmospheric opacity data which was measured by the Caltech Submillimeter Observatory (CSO) radiometer. Average zenith optical depths for each run are listed in Table 3.

Telescope pointing and focus were checked regularly by observing strong standard continuum point sources. Pointing was found to be repeatable within  $\approx 3''$  at the IRAM 30-m telescope and the JCMT, and  $\approx 5''$  at SEST. For flux calibration, maps of Uranus, Mars, Neptune, or different secondary calibrators (Sandell 1994) were obtained during each shift and at different elevations. Observing parameters for all runs are summarized in Table 3.

## 2.2. Reduction and calibration of the (sub)millimetre data

$1.3\text{ mm}$  bolometer maps observed using the IRAM 30-m and SEST telescopes were reduced and analyzed with the MOPSI<sup>2</sup> software package. The chopped dual-beam scan maps were flat-fielded, corrected for atmospheric extinction, de-spiked, baseline subtracted, and processed with an advanced sky

<sup>1</sup>JCMT is operated by the JAC, Hawaii, on behalf of the UK STFC, The Netherlands OSR, and the Canadian NRC.

<sup>2</sup>MOPSI (Mapping On-Off Pointing Skydip Infrared) is a software package for infrared, millimetre, and radio data reduction that has been developed and is updated by R. Zylka.

noise algorithm. The double-beam maps were then restored into single-beam maps using the Emerson-Klein-Haslam algorithm (Emerson et al. 1979). The individual maps were averaged with corresponding weights and converted into the equatorial coordinate system. The SIMBA fastscan maps were reduced according to the instructions in the SIMBA Observer’s Handbook (2002; see also Chini et al. 2003, Appendix A).

The SCUBA 450  $\mu\text{m}$  and 850  $\mu\text{m}$  jiggle maps were reduced with the SURF package (SCUBA User reduction Facility, Jenness & Lightfoot 1998). The individual maps were flat-fielded, corrected for extinction, processed with a sky-noise routine (Jenness et al. 1998), and combined. The SCUBA scan maps were processed in a similar manner, before removing the dual-beam function. Finally, the maps from the six different chop configurations were combined in Fourier space, weighting each to minimize noise on spatial scales corresponding to the chop throw (Jenness et al. 1998; Holland et al. 1999).

The data were calibrated using nightly observations of either primary planetary calibrators, or secondary calibrators when a planet was unavailable. Main beam flux calibration factors for all maps were computed by integrating over the main antenna beam in the planet maps, assuming planet brightness temperatures listed by Orton et al. (1986) and Griffin & Orton (1993) and correcting for the error beams (see below). The flux densities of the secondary calibrators were taken from Sandell (1994). The statistical scatter of the 1.3 mm flux calibration factors derived from all IRAM 30-m and SEST data was found to be  $\approx 6\%$ . Due to the uncertainty of the adopted planet temperatures and uncertainties in the flux integration procedure, we estimate that the total calibration uncertainty is  $\pm 15\%$  at 1.3 mm,  $\pm 20\%$  at 850  $\mu\text{m}$ , and  $\pm 30\%$  at 450  $\mu\text{m}$ . Typical  $1\sigma$  noise levels (off-source) in the final maps are  $5.5 \pm 1.3$  mJy/beam (IRAM 30-m) and  $20 \pm 5$  mJy/beam (SEST) at 1.3 mm,  $\sim 20$  mJy/beam at 850  $\mu\text{m}$ , and  $\sim 200$  mJy/beam at 450  $\mu\text{m}$ , respectively.

For each instrument and observing run, the average beam size full-width at half maximum (FWHM) was determined from the flux calibration maps, mostly on Uranus, taking into account the intrinsic size of the planet disk (see Table 3). The secondary calibrators are less well characterized, and so on nights when planetary beam-maps were unavailable, the average beam FWHM for the entire data-set is quoted in Table 3. Error beams at 1.3 mm and 850  $\mu\text{m}$  were found to be

negligible, but at 450  $\mu\text{m}$  a significant error beam was found to contribute up to  $\sim 50\%$  of the flux density. Note that the main beam flux calibration accounts for this (to first order). Flux density measurements in the final maps were done using the GILDAS<sup>3</sup> software and are described in Sect. 3.1.

For weak and extended sources, the integrated flux density and the derived source size also depend on the map size, the curvature of the extended flux density distribution, and the method of baseline subtraction, since the sources are always observed against a more extended emission background originating from the parental molecular cloud.

### 2.3. Near-infrared observations

We use the NIR images only for overlays with the (sub)mm maps, to identify which core is associated with a star or NIR nebula, and for discussion of evolutionary stages. NIR photometry is not described in this paper, but we use the fluxes for the SEDs where relevant. To this end, NIR observations of the globules listed in Table 2 were performed during five observing runs between December 1993 and October 2003 at the 3.5m telescope on Calar Alto, Spain and at the MPG/ESO 2.2-m telescope on La Silla, Chile. Observing parameters for all runs are compiled in Table 4. Images were obtained in standard dithering mode with 4 to 5 positions per field. Flat field calibrations were obtained each night via dome flats using difference frames of integrations with a halogen lamp on and off. Sets of photometric standard stars from lists by Elias et al. (1982) and Hawarden et al. (2001) were observed during each night, but the calibration for most sources was done by using 2MASS catalogue fluxes for stars in the fields.

The data were reduced using a combination of the IRAF<sup>4</sup> “Experimental Deep Infrared Mosaicking Software” (XDIMSUM<sup>5</sup>) and Starlink Project packages. For photometric calibration, zero-points were derived from observed standard stars of each night. Then, magnitudes for individual objects were derived using

<sup>3</sup><http://www.iram.fr/IRAMFR/GILDAS>

<sup>4</sup>IRAF is distributed by the NOAO, which are operated by the Association of Universities for Research in Astronomy, Inc., under cooperative agreement with the National Science Foundation.

<sup>5</sup>XDIMSUM is a variant of the DIMSUM package (V3: August 19, 2002) developed firstly by Eisenhardt et al. (1996)

GAIA<sup>6</sup> with the embedded PHOTOM<sup>7</sup> package. The average  $3\sigma$  point source detection limit in all three NIR bands is  $\sim 19$  mag. Only sources that are associated with a dense globule core (i.e. a (sub)mm source) are considered in this paper.

For astrometric calibration of mosaicked frames we used the Guide Star Catalogue II<sup>8</sup> and the SIMBAD<sup>9</sup>. The resulting typical positional accuracy is better  $0''.8$  ( $1\sigma$  rms).

## 2.4. *Spitzer* data

All sources listed in Table 2 were observed by *Spitzer* within different programs, most with *IRAC* and *MIPS*, except CB 17 SW, BHR 58, BHR 137, and CB 224. The relevant data were obtained from the *Spitzer* Science Center (SCC) Archive. In particular, we retrieved, where available, *IRAC* maps at 3.6, 4.5, 5.8, and  $8\mu\text{m}$  and *MIPS* scan maps at 24, 70, and  $160\mu\text{m}$ . The data were processed by the SCC using their standard pipeline to produce Post-Basic Calibration Data (P-BCD) images. Photometry was done in IDL by applying aperture photometry, where the aperture corrections available at the instruments webpage were used. The conversion from P-BCD units ( $\text{MJy sr}^{-1}$ ) to flux density was achieved by applying Quick Point Source Photometry as described online. The overall flux calibration and flux measurement accuracy is estimated by the SSC to be accurate to within 20%.

## 3. Results

### 3.1. (Sub)millimetre continuum maps

In Figs. 1 through 24, we present the (sub)mm maps, together with NIR K-band images for each of the sources listed in Table 2 (sources with only upper limits are not shown). Digital Sky-Survey (DSS2)<sup>10</sup>

<sup>6</sup>GAIA is provided by Starlink, and is a derivative of the Skycat catalogue and image display tool, developed as part of the VLT project at ESO. Skycat is free software under the terms of the GNU copyright.

<sup>7</sup>The PHOTOM photometry package is provided by Starlink

<sup>8</sup>The Guide Star Catalogue II is a joint project of the STSI and the Osservatorio Astronomico di Torino. STSI is operated by the Association of Universities for Research in Astronomy, for the NASA under contract NAS5-26555.

<sup>9</sup>SIMBAD is an online database, operated at CDS, Strasbourg, France

<sup>10</sup>The Digitized Sky Survey was produced at the Space Telescope Science Institute under US Government grant NAG W-2166. The images of these surveys are based on the photographic data obtained using the Oschin Schmidt Telescope on Palomar Mountain and the

optical images of the globules are also shown, together with the submm contours ( $850\mu\text{m}$  or  $1.3\text{ mm}$ ) and the boundaries of the submm maps, to illustrate their overall morphology and the relative location of the dense cores within the globules. Note that in the case of SCUBA jiggle maps the entire mapped region is indicated, while in the case of IRAM (dual-beam) or SEST scan maps only the area from which the mm emission was restored is marked. In addition, SEDs, including fluxes from optical wavelengths up to  $3\text{ mm}$ , are shown for those sources where we could compile sufficient data and associate them unambiguously to one source.

(Sub)mm flux densities are summarized in Table 5. The center coordinates for each dust core were derived from gaussian fits to the  $1.3\text{ mm}$  intensity maps after decomposition into extended envelope and individual compact components. For some sources (marked in Table 5), the peak position was derived from the  $850\mu\text{m}$  maps. The peak intensity  $I_{\nu}^{\text{peak}}$  of each compact component is given in Columns 3, 5 and 7 of Table 5 in units of  $\text{Jy/beam}$ . The beam size is also quoted here in parentheses. Note that the maps of some extended sources (e.g., CB 246) were convolved with a larger gaussian beam to increase the SNR. We also quote the total integrated flux density,  $S_{\nu}^{\text{tot}}$ , for each source. This was derived by integrating within a polygon enclosing the (closed)  $2\sigma$  contour. If there is one or more compact sources within a larger envelope, we also give the integrated flux densities of the compact sources, derived after fitting and subtracting the extended envelope from the maps. We do not list individual error bars for the flux densities, because uncertainties are mostly dominated by the calibration uncertainties (see Sect. 2.2). However, for extended sources, the uncertainty is dominated by the size of the area from which emission could be recovered above the  $2\sigma$ -level, which in turn depends on the curvature of the emission background, the ratios of the angular sizes of the beam, the source, and the chop throw, as well as on the SNR in the map. In general, the relative fraction of recovered to total actual flux increases from faint extended to strong compact, and from nearby to distant sources.

### 3.2. Association of sub(mm) and infrared sources

When compiling SEDs and attempting to model and interpret the observational results, it is important

UK Schmidt Telescope.

to reveal which of the sources and flux densities detected at different wavelengths, with different angular resolution, apertures, and astrometric precision, are actually physically associated and which ones have different origins. For this reason, we overlay the (sub)mm maps on the optical (DSS) and NIR images, show the IRAS point source position error ellipses where applicable, and also inspect the *Spitzer* maps where available (see 2.4).

We found the following associations between NIR/MIR sources and mm cores: No NIR sources brighter than 0.02 mJy ( $\approx 19$  mag) at  $2.2\,\mu\text{m}$  or  $\approx 1$  mJy at  $4.5\,\mu\text{m}$  are detected in CB 17-SMM1 and 2, CB 130-SMM2, CB 232-SMM, CB 243-SMM1 and 2, and CB 246. However, since local dust extinction, source morphology, and projection effects (e.g., the alignment between the line of sight and outflow cavities) play a major role at these early evolutionary stages, this detection limit cannot be directly converted into an upper limit for the mass or luminosity of possible embedded sources. No K-band emission, but faint NIR sources with steeply rising NIR SEDs peaking at  $\approx 4\ldots 6\,\mu\text{m}$  have been found in BHR 55, BHR 86, CB 68, and CB 199. Extended NIR nebulosities, in several cases NIR jets, but no star-like objects were detected in CB 26, BHR 12-SMM1 and SMM2, BHR 36, BHR 71, CB 130-SMM1, CB 224-SMM1, CB 230, and CB 244-SMM1. A single red star or compact star-like NIR source, in some cases with extended nebulosity, was detected at the mm peak position in CB 6, CB 188, and CB 224-SMM2. Several NIR sources or clusters, respectively, are associated with the (sub)mm cores in CB 34, CB 54, CB 205, and CB 240. The situation is somewhat inconclusive in CB 58 and BHR 137, where it is not clear if the NIR sources are actually associated with the mm core or not.

The following (sub)mm cores have very nearby, but most likely not directly associated NIR/MIR sources and the flux measurements could not always be disentangled: CB 17 has an IRAS point source and a *Spitzer*-detected low-luminosity IR point source that is clearly not associated with the mm core (Fig. 2). CB 130-SMM1 is a strong and slightly extended submm source with a small NIR nebula at the mm peak position. A very nearby ( $14''$ ) strong and pointlike IR source (IRS) could not be completely disentangled from SMM1, but does not seem to exhibit detectable mm emission on its own. CB 232 and CB 243 both have bright reddened stars within the area of the mm emission, but clearly offset and not associated with the

main mm peak.

### 3.3. Multiplicity

Although the (sub)mm maps are not sensitive to spatial scales that cover the peak of the binary star separation distribution (20–100 AU; Duquennoy & Mayor 1991), we find that at least 16 out of 24 globules with detected (sub)mm emission show signatures of multiplicity at scales larger than  $\approx 1,000$  AU, out to 80,000 AU (0.4 pc; see Table 6). This includes prestellar and protostellar double cores resolved in the mm dust continuum (e.g., CB 17, CB 130, CB 246, BHR 12), unresolved protostellar cores where NIR or MIR observations have revealed a secondary embedded source (e.g., CB 230, BHR 71), prestellar or protostellar cores where NIR/MIR observations have revealed sources that are significantly offset from the (sub)mm peak and that are most likely not embedded in these cores (e.g., CB 17, CB 130, CB 232, CB 243; see Fig. 28), as well as large dust cores that are associated with clusters of NIR sources, presumably young stars that formed from the same globule (e.g., CB 34, CB 54, CB 205). Nine of these 24 globules were resolved to have two or more cores in the (sub)mm dust emission maps (see Table 6). However, only three of these double cores have projected separations  $< 10,000$  AU (CB 17, BHR 12, and CB 130). Separations  $> 10,000$  AU are probably not relevant for the formation of bound stellar systems.

Altogether, we find that at least two thirds (16 out of 24) of the star-forming globules studied here show evidence of forming multiple stars, either in multiple star-forming cores, wide embedded binaries, or small star clusters. The fraction of closer binaries formed from unresolved (sub)mm cores might be higher, but remains unknown from this study (cf. Maury et al. 2010).

### 3.4. Spectral Energy Distributions

Spectral Energy Distributions (SEDs) were compiled from aperture photometry in the (sub)mm maps (Table 5) and NIR images (Figures 1–24) presented in this work (Sects. 3.1 and 3.2), the 2MASS catalogue, the IRAS point source catalogue, pipeline-calibrated *Spitzer* IRAC and MIPS maps, and other publicly available databases and literature papers. We do not explicitly list all flux values which we have compiled, but show in Figs. 1 through 23 the SEDs for those sources where we are confident that the measure-

ments represent one source or, in some cases, physically related, mostly unresolved double sources (e.g., CB 230). Note that we actually show the energy density ( $\nu S_\nu$ ) and not the flux density ( $S_\nu$ ). We do not show SEDs for sources where we either do not have enough data points (e.g., BHR 137, CB 246) or where the (sub)mm emission is associated with multiple NIR sources (e.g., CB 34, CB 54, CB 58, CB 205, CB 240). For the other sources, we indicate in the figure captions and in Table 7 whether we use the total (sub)mm fluxes or only one compact component. Non-detections are indicated by down-arrows as  $3\sigma$  upper limits. Flux values that derive from apertures smaller than the expected emission region (e.g., single-point measurements with the JCMT-UKT14 bolometer) or interferometric measurements, which are not sensitive for extended emission, are indicated by up-arrows as lower limits. A comprehensive overview of all SEDs, ordered by evolutionary stage (see Sect. 3.5) is shown in Fig. 25.

In order to derive luminosities and bolometric temperatures, we first interpolated and then integrated the SEDs, always assuming spherical symmetry. In the case of, e.g., bipolar NIR reflection nebulae, this may lead to either an under-estimate of the NIR luminosity (e.g., CB 26, Fig. 3) or an overestimate (e.g., CB 230, Fig. 19), depending on the inclination with respect to the line-of-sight. However, all sources studied in this paper emit the majority of their total energy at much longer wavelengths, where the radiation is reprocessed by dust, so that the general results derived here are not significantly affected by the simplifying assumption of spherical symmetry. Interpolation between the measured flux densities was done by a  $\chi^2$  grey-body fit to all points at  $\lambda \geq 100\mu\text{m}$  and by simple logarithmic interpolation between all points at  $\lambda \leq 100\mu\text{m}$ . Free parameters in the grey-body fits were the dust temperature, source size, and optical depth. The (sub)mm spectral index of the dust emissivity was fixed to  $\beta = 1.8$  (see Sect. 3.6). Fitted dust temperatures were in the range 15 K (CB 17-SMM) to 53 K (CB 224-SMM2), with mean values of 33 K for Class 0 sources and 42 K for Class I sources (see Sect. 3.5).

Note, however, that we use these fits only to derive an approximate interpolation for integrating the SEDs. In particular, we do not use the dust temperatures or source size from these grey-body fits because the derived effective temperatures are usually dominated by small contributions from either embedded

heating sources or externally heated very small grains in the envelopes. Thus, they usually do not represent the mass-averaged dust temperature. Instead, we use fixed mass-averaged dust temperatures as function of evolutionary stage (see Sect. 3.6) and derive source sizes directly from the (sub)mm maps.

### 3.5. Evolutionary stages

We use a combination of different diagnostics to derive the evolutionary stages of the globule cores. We do not attempt to classify those cores of distant globules that are associated with clusters of NIR sources and for which the NIR, FIR (IRAS), and (sub)mm emission could not be uniquely associated (e.g., CB 34, CB 54, CB 58, CB 205, CB 240). Sources for which we have barely more information than a mm flux (e.g., BHR 58, BHR 137) are also not considered here. For the other sources, we analyze the following tracers of evolutionary stage:

1. The ratio of submm to bolometric luminosity,  $L_{\text{submm}} / L_{\text{bol}}$ , where  $L_{\text{submm}}$  is measured longward of  $350\mu\text{m}$ , which roughly reflects the ratio of envelope to stellar mass,  $M_{\text{env}} / M_*$  (André et al. 1993). André et al. (2000) propose to use  $L_{\text{submm}} / L_{\text{bol}} > 0.5\%$  as a threshold for Class 0 protostars, reflecting  $M_{\text{env}} / M_* > 1$ .
2. The bolometric temperature,  $T_{\text{bol}}$  (Myers & Ladd 1993), which is defined by the temperature of a blackbody having the same mean frequency (ratio of the first and the zeroth moment of the SED) as the observed continuum spectrum. Chen et al. (1995) and Myers et al. (1998) derive the boundary between Class 0 and Class I YSOs to be at  $T_{\text{bol}} \sim 70$  K. Note that we use the interpolated SEDs (see Sect. 3.4) with flux values at all wavelengths to compute  $T_{\text{bol}}$  and luminosities, rather than just the actual data points. The latter approach could lead to significant biases if the SED is not well-sampled (cf. Enoch et al. 2009).
3. The IR spectral index,  $\alpha_{\text{IR}} = -d \log(\nu F_\nu) / d \log \nu$  (Lada 1987), which characterizes the IR excess with respect to stellar blackbodies. Where sufficient data are available, we calculate  $\alpha_{\text{IR}}$  between  $\lambda = 2.2$  and  $24\mu\text{m}$ , thus avoiding to characterize only the NIR/MIR nebulosity “bump” in the Class 0 SEDs (see below), the possible

influence of the silicon absorption, and the low-resolution *IRAS* measurements at 12 and 25  $\mu\text{m}$ , which are prone to confusion problems. Quantitatively, we follow André & Montmerle (1994) and use  $\alpha_{\text{IR}} = 0$  as boundary between Class I and II. No well-defined boundary exists for Class 0 sources since only *Spitzer* lead to the detection of the NIR/MIR emission in many of them.

Along with these three quantitative classification criteria, we evaluate the morphology of the NIR emission and the presence of molecular outflows. The first one can be either direct star light, indicating that the circumstellar emission originates either from an optically thin envelope or a phase-on disk, or diffuse nebulosity, indicating, e.g., scattered light from outflow cavities in an otherwise optically thick envelope. The presence of a molecular outflow is an indicator of an embedded source that distinguishes protostars from prestellar cores. Two notes of caution are: (i) the non-detection of an outflow does not prove the absence of an embedded protostar, in particular as we have no homogeneous high-sensitivity, high-angular resolution outflow survey at hand, and (ii) the driving source of an outflow is not necessarily identical with the (sub)mm source - this must be verified in each individual case.

The applicability and drawbacks of the classification criteria mentioned above has been discussed in detail by Enoch et al. (2009). An analysis of our data confirms the finding of these authors in that  $\alpha_{\text{IR}}$  does not correlate well with  $T_{\text{bol}}$  and embeddedness for Class 0 and embedded Class I sources. The deep NIR images, in particular those from *Spitzer*, show that most of even the youngest Class 0 sources already have a small NIR nebulosity associated. This can also be clearly seen in the compilation of SEDs shown in Fig. 25. We attribute this to the fact that the amount of NIR/MIR flux seen from such an embedded object largely depends on the alignment between the line of sight and the outflow cavity, allowing or not a direct view onto the hot dust in the inner protostellar core and/or forward-scattered light in the outflow cavity. Therefore, we only list the  $\alpha_{\text{IR}}$  values in Table 7, but do not use them for the classification of evolutionary stages.

We find that all sources, for which we could compile meaningful SEDs, have  $L_{\text{submm}} / L_{\text{bol}} \geq 0.8\%$  (Table 7), i.e., according to the criterion proposed by André et al. (2000) they would all be Class 0 sources. The bolometric temperature, although reflecting sim-

ilar properties of the SEDs, appears to be a more reliable indicator of the evolutionary stage than the  $L_{\text{submm}} / L_{\text{bol}}$  ratio, as it is less sensitive to the amount of extended envelope emission recovered in the submm maps (see Sect. 4.1). We therefore use the bolometric temperature as the main discriminator between Class 0 protostars and Class I YSOs, along with the other supporting indicators mentioned above (cf. Enoch et al. 2009).

The derived evolutionary stages, along with other source properties, for 18 globules are summarized in Table 7. Figure 26 shows the  $L_{\text{submm}} / L_{\text{bol}}$  ratio vs.  $T_{\text{bol}}$  for these sources. In total, we identified nine starless cores, presumably prestellar, in six globules, nine Class 0 protostars in nine globules, and twelve Class I YSOs in eleven globules. Interestingly, seven globules contain co-existing sources at different evolutionary stages (see discussion in Sect. 4.2). Six globules were not detected at (sub)mm wavelengths, and for the submm cores in eight globules we could not or did not attempt to derive an evolutionary stage because we either had insufficient data, or the available data indicated that several sources with possibly different evolutionary stages contribute to the partially unresolved flux measurements.

### 3.6. Physical parameters of the star-forming cores

The following physical source quantities are derived from the (sub)mm continuum maps and the SEDs: bolometric and submm luminosities (Sect. 3.5), source sizes, masses, beam-averaged peak column densities, and source-averaged volume densities.

FWHM mean source sizes ( $\sqrt{ab}$ ) are simply derived by measuring the angular diameters of the 50% contours in the 850  $\mu\text{m}$  or 1.3 mm maps (after decomposition into envelope and compact core, where applicable), deconvolving them with beam size, and applying the distances listed in Table 2. The results are listed in Table 7.

To calculate masses, densities, and column densities, we adopt mass-averaged mean dust temperatures that depend on the evolutionary stage of the source (Sect. 3.5). Quantitatively, we follow Motte & André (2001), Shirley et al. (2002), and Young et al. (2003), who have derived mean mass-averaged isothermal dust temperatures from radiative transfer models for samples of starless cores, Class 0 protostars, and envelopes of Class I YSOs. We use here  $\langle T_d \rangle = 10$  K for starless (prestellar) cores,  $\langle T_d \rangle = 15$  K for Class 0 pro-



tostars, and  $\langle T_d \rangle = 20$  K for the envelopes of Class I YSOs. The first dust temperature map directly derived from new *Herschel* data of the Bok globule CB 244 with its two embedded cores confirms the validity of these temperature assumptions (Stutz et al. 2010). The adopted temperatures and resulting masses for each source are listed in Table 7.

Assuming optically thin isothermal dust emission, the hydrogen gas mass  $M_H = M(\text{H}) + 2 M(\text{H}_2)$  is calculated from the (sub)mm flux density by

$$M_H = \frac{S_\nu D^2}{\kappa_d(\nu) B_\nu(\nu, T_d)} \left( \frac{M_H}{M_d} \right). \quad (1)$$

Here,  $\nu$  is the observing frequency,  $S_\nu$  the observed flux density from the region of interest,  $D$  is the distance to the source,  $\kappa_d(\nu)$  is the dust opacity,  $B_\nu(\nu, T_d)$  the Planck function,  $T_d$  the dust temperature, and  $M_H/M_d$  the hydrogen-to-dust mass ratio. Throughout this paper, we use a hydrogen-to-dust mass ratio of  $M_H/M_d = 110$  and a dust opacity of  $\kappa_d(\lambda) = \kappa_d(1.3\text{mm}) \times (\lambda/1.3\text{mm})^{-1.8}$  with  $\kappa_d(1.3\text{mm}) = 0.5 \text{ cm}^2 \text{ g}^{-1}$  (Ossenkopf & Henning 1994, uncoagulated MRN dust grains with thin ice mantles), a that is value typical for dense and cold molecular cloud cores and intermediate between the opacities usually adopted for unprocessed interstellar grains in the diffuse gas (e.g., Draine & Lee 1984) and for processed and coagulated grains in protoplanetary disks (e.g., Beckwith et al. 2000).

We derive total Hydrogen masses of  $1 - 20 M_\odot$  for prestellar cores,  $0.5 - 10 M_\odot$  for Class 0 protostars, and  $0.11 - 1 M_\odot$  for Class I YSOs (not counting the extended envelopes; see Table 7). The total gas mass, accounting for helium and heavy elements, amounts then to  $M_g \approx 1.36 M_H$ .

The beam-averaged peak Hydrogen column density  $N_H = N(\text{H}) + 2 N(\text{H}_2)$  was derived from the observed peak flux densities by

$$N_H = \frac{I_\nu}{\kappa_d(\nu) \Omega_B B_\nu(\nu, T_d)} \frac{1}{m_H} \left( \frac{M_H}{M_d} \right), \quad (2)$$

where  $I_\nu$  is the peak flux density (Table 5),  $\Omega_B = 1.133 \theta_B^2$  the beam solid angle,  $\theta_B$  the beam FWHM size, and  $m_H$  is the the proton mass. The resulting beam-averaged peak column densities are also listed in Table 7.

Assuming that the sources have the same extent along the line of sight as the mean size perpendicular to the line of sight, the source-averaged volume density

of hydrogen atoms,  $n_H = n(\text{H}) + 2 n(\text{H}_2)$ , was calculated by

$$n_H = \frac{M_H}{m_H V}, \quad (3)$$

with  $V \sim \pi/6 d_S^3$  being the volume of the source, and  $d_S$  the FWHM size listed in Table 7. The resulting densities are listed in Table 7. Note that these are source-averaged densities and the local peak densities in sources with density gradients can be orders of magnitude higher.

In an earlier paper, we had also derived radial density profiles for most of the globule cores by fitting ray-traced and beam-convolved model cores to the radially averaged (sub)mm data at all three wavelengths (Launhardt 2005). The extended dataset presented in this paper would certainly permit to derive better-constrained density profiles for many globules cores. However, as in this previous paper, such an analysis would be hampered by the fact that we have to assume temperature profiles, since the (sub)mm data provide only weak constraints. In particular for the prestellar cores, which do not have a central heating source and may have a positive radial temperature gradient, this can introduce significant biases and may lead to an underestimation of the density gradient. Since we expect to obtain soon *Herschel* data for many of the sources presented here, which will provide direct constraints on the temperature profiles, we postpone the derivation and analysis of the radial density profiles to a succeeding paper.

## 4. Discussion

### 4.1. Source properties as function of evolutionary stage

Being relatively nearby and isolated, the cores of Bok globules are the best-suited places to observe the properties and evolution of individual low-mass star-forming cores. However, this isolation, which makes them such good targets, may also alter the core properties and evolutionary process as compared to the more representative (for general star formation), but harder to observe, star-forming cores in clustered regions. Some of the most obvious differences in environmental conditions are the interstellar radiation field, which is not shielded by the surrounding cloud, the missing external pressure due to the lack of inter-core gas, and the lack of turbulence input from the surrounding cloud.

The most obvious changes in core properties during the evolution from prestellar cores, through collapsing

protostars, towards Class I YSOs are expected to be seen in the core size, central core density, ratio of core mass to envelope mass, and contribution of the central (proto)star to the source luminosity at shorter wavelengths. The latter two effects have been used in the form of parameters  $L_{\text{submm}}/L_{\text{bol}}$  and  $T_{\text{bol}}$  as main criteria to identify the evolutionary stage of the sources (Sect. 3.5).

In Figure 26, we show a plot of  $L_{\text{submm}}/L_{\text{bol}}$  vs.  $T_{\text{bol}}$  for the sources compiled in Table 7. We find that all sources with  $T_{\text{bol}} < 70$  K, the empirical boundary between Class 0 protostars and Class I YSOs proposed by Myers et al. (1998), have  $L_{\text{submm}}/L_{\text{bol}} > 2\%$ . Within the Class 0 phase, there seems to be no significant correlation between the two parameters and no obvious evolution from lower to higher values of  $T_{\text{bol}}$ . This may reflect the fact that during this early phase, the optically thick envelope dominates over the still very low-mass and low-luminosity central protostar. However, there is a relatively large spread in  $L_{\text{submm}}/L_{\text{bol}}$  ratios, probably reflecting the fact that during this phase the mass of the infalling envelope is relatively quickly reduced.

The more evolved (Class I) YSOs in our sample have bolometric temperatures between 100 K and 350 K and  $L_{\text{submm}}/L_{\text{bol}} \sim 0.8 \dots 3.5\%$  (see Fig. 26). All sources with NIR nebulosities but no visible stars have  $L_{\text{submm}}/L_{\text{bol}} \geq 1.6\%$  and extended (resolved) (sub)mm emission. These sources are probably less-evolved, envelope-dominated Class I YSOs. The three sources with  $L_{\text{submm}}/L_{\text{bol}} \leq 1.3\%$  (CB 188, CB 224-SMM2, CB232-IRS1) all have visible stars and compact (sub)mm emission arising presumably from circumstellar disks. These sources probably represent the more evolved, disk-dominated Class I YSOs. We take these findings as tentative indication that the  $L_{\text{submm}}/L_{\text{bol}}$  ratio, as indicator of envelope dispersal, may better trace the evolution within the Class 0 and Class I phases than  $T_{\text{bol}}$ .

Two of the Class I sources in our sample have double-peaked SEDs with NIR nebulosities and  $\alpha_{\text{IR}} < 0$  (CB 26, CB 230), which would indicate Class II. However, the IR emission seems completely originating from scattered light and the IR fluxes and morphology seem dictated by projection effects. For CB 26, a massive edge-on protoplanetary disk with a remnant envelope, Launhardt & Sargent (2001) derive an age of  $\approx 1$  Myr. CB 230, with a more massive envelope and less-developed disk(s) (Launhardt 2001), is most likely younger. We therefore classify these two

sources as “Class I” in Table 7, despite the fact that they have  $\alpha_{\text{IR}} < 0$ .

To verify these relations between  $T_{\text{bol}}$ ,  $L_{\text{submm}}/L_{\text{bol}}$ , and evolutionary stages, we have compared our sample of globule cores to the sample of Class 0 protostars from André et al. (2000). Plotting these sources into the same diagramme (not shown here) shows a different picture. While none of the globules sources have both  $T_{\text{bol}} < 70$  K and  $L_{\text{submm}}/L_{\text{bol}} < 2\%$ , numerous protostars from the André sample do populate this region. The two different source samples have similar distance distributions, and in each case, both nearby and more distant sources are distributed evenly around the  $L_{\text{submm}}/L_{\text{bol}}$  vs.  $T_{\text{bol}}$  plot. Therefore there is no evidence to suggest that limited resolution or sensitivity for either of the samples is causing the discrepancy. Similarly, there is no evidence that any particular aspect of the morphology of a Bok globule is causing this discrepancy between the two samples. As none of the above characteristics can possibly cause a systematic shift of the Bok globules in the  $L_{\text{submm}}/L_{\text{bol}}$  vs.  $T_{\text{bol}}$  diagramme, we conclude that the absence of globule cores with both low  $T_{\text{bol}}$  and low  $L_{\text{submm}}/L_{\text{bol}}$ -ratios is a real effect, caused by the systematic environmental differences between the cores of Bok globules and protostars located in larger molecular clouds mentioned at the beginning of this section.

The outer boundary of a protostellar core that is embedded in a larger molecular cloud is generally judged to be where its envelope merges with the surrounding cloud material, or the envelope of an adjacent object. In contrast, the column density profile of a globule core continuously decreases towards the “edge” of the small cloud, making it more difficult to distinguish between the core and the surrounding cloud, both physically and observationally, as the envelope (cloud) emission is usually not chopped away in the small globules. This has the effect of making the detected envelopes larger and elevating the submm luminosity as compared to dense cores embedded in larger clouds. It is therefore possible that the cutoff in  $L_{\text{submm}}/L_{\text{bol}}$ , used to differentiate between Class 0 protostars and Class I YSOs should be raised from 0.5% in the case of protostars in larger molecular clouds, to  $\approx 2\%$  in the case of isolated Bok globules, to account for their larger envelope of cold dust. The value of 2% is chosen as this is the lowest value of  $L_{\text{submm}}/L_{\text{bol}}$  in the observed sample of globule cores with  $T_{\text{bol}} < 70$  K. Although we cannot present a modified quantitative physical model (cf. André et al. 1993), we think that this different cut-

off value for  $L_{\text{smm}}/L_{\text{bol}}$  still represents the point where the mass of the infalling protostellar envelope is equal to that of the accreting protostar, but it accounts for the contribution from the extended envelope which can no longer be clearly distinguished from the protostellar core.

We conclude that  $T_{\text{bol}}$  appears to be the most reliable parameter to discriminate between Class 0 protostars and Class I YSOs, with no hint for a systematic difference between sources in isolated globules and those embedded in larger molecular clouds. On the other hand, the evolution during the Class 0 phase and during the Class I phase may probably be better traced by the  $L_{\text{smm}}/L_{\text{bol}}$  ratio. Despite the fact that the two parameters are not completely independent, this can be understood as a consequence of  $T_{\text{bol}}$  being more sensitive to a flux contribution at shorter (NIR) wavelength from a central heating source, while  $L_{\text{smm}}/L_{\text{bol}}$  is more sensitive to the size and mass of the cold envelope.

We have also determined the mean FWHM core sizes and the mean source-averaged volume densities (see Table 7) of the three evolutionary subgroups. We find that the mean core sizes decrease from  $\approx 8,000$  AU for prestellar cores, to  $\approx 3,000$  AU for Class 0 protostars, to  $< 2,000$  AU for Class I YSOs (Fig. 27). We also find that the Class I YSOs usually have extended envelopes with a mean diameter of  $20,000$  AU. The source sizes of the Class 0 protostars might be somewhat underestimated since we did not decompose the sources into central point source (the warm protostar) and envelope before measuring the FWHM size. The source-averaged volume densities,  $n_{\text{H}}$ , increase from  $1 \times 10^7 \text{ cm}^{-3}$  for prestellar cores, to  $7 \times 10^7 \text{ cm}^{-3}$  for Class 0 protostars. At these high densities, one can in general assume that gas and dust temperatures are coupled. For the cores of the Class I YSOs, which are mostly unresolved and presumably contain significant flux contributions from circumstellar disks, we derive a lower limit to the mean density of  $> 8 \times 10^7 \text{ cm}^{-3}$ . The extended remnant envelopes of the Class I YSOs have a mean density of  $7 \times 10^4 \text{ cm}^{-3}$ .

#### 4.2. Multiple and sequential star formation in globules

One interesting aspect of the combined results for multiplicity and evolutionary stages is that the large majority of the globules with signs of multiple star formation shows evidence of non-coeval, possibly

sequential star formation. This includes neighbouring mm sources with obviously different evolutionary stages (e.g., BHR 12, CB 130, CB 224), prestellar or protostellar cores with nearby IR sources, presumably more evolved protostars or Class I YSOs (e.g., CB 17, CB 130, CB 232, CB 243), as well as NIR star clusters next to large (sub)mm cores with the potential to form more stars (e.g., CB 34, CB 54, BHR 137) (see Table 7). In only three globules we find (approximately) coeval pairs, ranging from multiple pre-stellar cores in CB 246, embedded Class 0 protostars in BHR 71, to a pair of embedded Class I YSOs in CB 230.

The most interesting sources in this respect are shown in Fig. 28. CB 17 contains two prestellar cores and one low-luminosity Class I YSO within  $5,000$  AU (projected separation). CB 130 contains three sources within  $9,000$  AU, all with different evolutionary stages. A Class 0 protostellar core is flanked by a prestellar core at  $6,000$  AU to the west, and by a Class I or II YSO at  $3,000$  AU to the east. CB 232 and CB 243 both contain a prestellar core with a Class I YSO within  $7,000$  AU.

This widespread non-coevality suggests that the multiple sources observed here have in general not formed by gravitational fragmentation of collapsing protostellar cores (e.g., Bonnell & Bate 2006), but rather by initial turbulent fragmentation prior to the collapse phase (e.g., Padoan & Nordlund 2002), followed by a relatively independent evolution of the individual fragments. Whether or not the first forming star can trigger collapse of the other fragment(s) and thus lead to small-scale sequential star formation cannot be directly answered by this study. The lack of close coeval pairs can be understood as an observational bias as our study is in general not sensitive to size scales  $< 1,000$  AU, which would be more relevant to the first mechanism. Consequently, we cannot draw direct conclusions on the frequency of bound binary stars formed in isolated Bok globules (cf. Maury et al. 2010).

These findings also call for special attention when compiling SEDs and attempting to derive source properties from flux measurements with insufficient angular resolution. One may easily end up classifying the combined SED of a prestellar core and a nearby, more evolved YSO as a Class 0 protostar (see, e.g., CB 243, Fig. 22f).

## 5. Description of individual globules

In this section, we describe in somewhat more detail the individual globules, their morphology and physical properties, and discuss the evolutionary stages of the embedded sources. Distance references are not given in the text, but are compiled in Table 2. Globule sizes and morphology are summarized in Table 6 and properties and evolutionary stages of the embedded sources are summarized in Table 7.

**CB 4** is a small, roundish, and relatively isolated dark globule at a somewhat uncertain distance. Although Wood et al. (1994) assumed a distance of 200 pc to the Cas A dark clouds in this region of the sky, we follow the analysis of Dickman & Clemens (1983) who derived a distance of 600 pc. This latter value is also close to the distance of the “-12 km s<sup>-1</sup>” clouds (800 pc; Dame et al. 1987) with which Launhardt & Henning (1997) associated the globules CB 4 and CB 6. CB 4 is associated with an IRAS point source, located at its southern rim, which is detected at 100  $\mu$ m only. There is no further evidence of an embedded source, including the *Spitzer* maps up to 160  $\mu$ m. Deep IRAS aperture photometry and molecular line studies showed that the globule is cold ( $\sim 7$  K) and has a relatively low mean density (Clemens et al. 1991; Kane et al. 1994; Turner et al. 1997). Despite its compact and dark appearance it thus rather resembles a cirrus cloud. CCD polarimetry of background stars revealed a faint and well-ordered magnetic field with a position angle (P.A.) of 71° (Sen et al. 2005), which is apparently coupled to the surrounding Galactic field (Kane et al. 1995). Our non-detection of compact thermal dust emission confirms the assumption that this globule does not seem to form stars.

**CB 6** (LBN 613; Fig. 1) is a small, cometary-shaped globule with a long diffuse tail, visible as scattered light cloudshine. It is located only a few degrees from CB 4 and has the same radial velocity. We therefore assign CB 6 the same distance (600 pc) as CB 4. At its centre, the globule harbours an embedded YSO with circumstellar dust emission and a conical reflection nebula (RNO 3; Cohen 1980; Eiroa et al. 1994), likely representing scattered light in an outflow cone from the embedded YSO. Indeed, broad line wings in CO (2-1) (Clemens et al. 1991) and CS (2-1) (Launhardt et al. 1998) indicate the presence of a molecular outflow from the YSO, but no outflow maps exist yet. Scapini & Codella (1996) searched for, but did not detect NH<sub>3</sub> and C<sub>2</sub>S. The evolutionary stage of the YSO is

controversial: while Clemens & Barvainis (1988) described it as Class III YSO, Launhardt et al. (1997) derived a  $L_{\text{bol}} / L_{\text{mm}}$  ratio indicative of a Class 0 protostar (André et al. 1993). Our (sub)mm continuum maps (Fig 1) show that the thermal dust emission is dominated by a compact source centered at the origin of the NIR nebula, indicating that the bulk of the mm dust emission does not originate from an optically thick envelope, but rather from a disk. The disk and the more extended envelope probably obscure the southern outflow lobe which is presumably pointed away from us. This morphology, combined with the bolometric temperature of  $T_{\text{bol}} \sim 180$  K let us conclude that this is a Class I YSO.

CB 6N is a small globule located  $\approx 10'$  north of CB 6. It has no IR source associated and we did not detect it at mm wavelengths, indicating that it does not contain a star-forming core.

**CB 17** (L 1389; Fig. 2) is a small and slightly cometary-shaped globule, located near Perseus and associated with the Lindblad ring (Lindblad et al. 1973). It has a long diffuse tail, pointing north-east and visible as cloudshine reflection. The distance of CB 17 was derived by Launhardt & Henning (1997) via association in projected space and radial velocity with other Lindblad Ring clouds. In the direction of CB 17, the Lindblad Ring structures have a mean distance from the Sun of  $\approx 300$  pc (Dame et al. 1987). HD 25347, a bright G5 III star at a distance of  $210 \pm 40$  pc (van Leeuwen 2007) is located about  $\approx 11'$  (0.65 pc at 200 pc) south of CB 17 and could be responsible for the cometary shape and diffuse cloudshine from the rim and tail of CB 17 if it is located at the same distance as the globule. Combining the possible associations of CB 17 with both the Lindblad Ring and HD 25347, and the distances and uncertainties involved, we adopt a distance of  $250 \pm 50$  pc for CB 17.

The roundish cloud core of CB 17 is associated with a dense submm core and a faint and cold IRAS point source (IRAS 04005+5647) that is detected only at 60 and 100  $\mu$ m. CB 17 has been studied extensively by various authors using different mm molecular line transitions. The core was found to have a mean kinetic gas temperature of  $T_{\text{kin}} \sim 10$  K and a virial mass of  $\approx 3 M_{\odot}$  (e.g., Lemme et al. 1996; Caselli et al. 2002, scaled to  $D = 250$  pc). Pavlyuchenkov et al. (2006) compared a number of different molecular line maps of CB 17 with chemodynamical models. They derive a chemical age of  $\approx 2$  Myr, as well as the relative rota-

tional, thermal and turbulent energies, concluding that the core will most likely fragment.

Indeed, our deep 1.3 mm continuum map (Fig. 2) shows a double core with  $14''$  separation and a common envelope, located at the south-western rim of the globule head. The low-SNR  $850\mu\text{m}$  SCUBA map can, however, not confirm the double-core nature, and the source remains undetected at  $450\mu\text{m}$ . The *Spitzer* IRAC maps show a  $8\mu\text{m}$  shadow that agrees in position and shape with the double core (Fig. 28). No emission is detected at wavelengths shorter than  $160\mu\text{m}$ , indicating these cores have no, or only very low-luminosity internal heating sources. Since the double core is resolved only in the 1.3 mm map, we compile the SED only for the combined core, which we call SMM. However, a faint point-like NIR/MIR source (IRS), that is clearly not directly detected in the (sub)mm continuum, is located  $\approx 10''$  northwest of SMM and just outside the  $8\mu\text{m}$  shadow, indicates the presence of a third, more evolved source in CB 17 (Fig. 28). This source dominates the emission at wavelengths shorter  $160\mu\text{m}$ , while SMM dominates at longer wavelengths. Although the MIPS3 map at  $160\mu\text{m}$  does not resolve the two positions, a slight shift of the peak position from IRS towards SMM indicates detectable emission from SMM at this wavelength. For compiling the SEDs, we assigned 15% of the total  $160\mu\text{m}$  flux to SMM, but our results depend only weakly on the adopted flux splitting. The morphology and SED of SMM ( $T_{\text{bol}} \approx 15\text{ K}$ ,  $L_{\text{SMM}} / L_{\text{bol}} > 30\%$ ) suggest this is a prestellar (double) core (cf. Caselli et al. 2002; Pavlyuchenkov et al. 2006). Source IRS, which is located at a projected separation of  $\sim 2000\text{ AU}$  from SMM2 within the same globule core, is tentatively classified as a low-luminosity Class I YSO protostar ( $T_{\text{bol}} > 55\text{ K}$ ,  $L_{\text{SMM}} / L_{\text{bol}} < 2.6\%$ ), although an outflow remains to be detected (Chen et al., in prep.). A faint and diffuse NIR nebula at the position of SMM2 is speculated to be related to IRS rather than to a source embedded in SMM2, although the nature of a faint compact NIR knot at the peak position of SMM2 remains unknown. We are currently analyzing interferometric molecular line maps, attempting to better constrain evolutionary stages and the kinematic relation of the three sources (Schmalzl et al., in prep.). CB 17 is thus one of those globules that contain two or more sources of different evolutionary stage with a few thousand AU (see Sect. 4.2 and Table 6).

CB 17 SW (L 1388) is a small elliptical globule

of similar size as CB 17, located  $\approx 12'$  south-west of CB 17. It has no IR source associated and we did not detect it at mm wavelengths, indicating that it does not contain a star-forming core.

**CB 26** (L 1439; Fig. 3) is a small, cometary-shaped, double-core Bok globule located  $\sim 10^\circ$  north of the Taurus-Auriga dark cloud, at a distance of  $\sim 140\text{ pc}$ . An IRAS point source and dense core with signatures of star formation is located at the south-west tip of the western globule core (Launhardt & Henning 1997). While the eastern globule core (at 4:56:20, 52:01:30, B1950, in Fig. 3) is visible as  $8\mu\text{m}$  shadow in the *Spitzer* IRAC maps, the IR source is located  $\approx 4'$  further west. The eastern globule core was not searched for mm emission, but the *Spitzer* maps also do not indicate the presence of an embedded source. OVRO observations at the IRAS position of the mm dust continuum emission and of the  $^{13}\text{CO}(1-0)$  line have revealed a nearly edge-on circumstellar disk of radius  $200\text{ AU}$  with Keplerian rotation (Launhardt & Sargent 2001), surrounding a very young (obscured) low-mass T Tauri star. It is associated with a small bipolar near-infrared (NIR) nebula bisected by a dark extinction lane at the position and orientation of the edge-on disk (Stecklum et al. 2004). The star and disk are surrounded by an optically thin asymmetric envelope with a well-ordered magnetic field directed along P.A.  $\sim 25^\circ$  (Henning et al. 2001). Furthermore, an Herbig-Haro object (HH 494) was identified by H $\alpha$  and S[II] narrow-band imaging,  $6.15\text{ arcmin}$  northwest of CB 26 at P.A.  $= 145^\circ$  (Stecklum et al. 2004). The HH object is thus perfectly aligned with the symmetry axis of the disk and the bipolar nebula. Recently, Launhardt et al. (2009) reported the discovery of a small collimated molecular outflow along the same direction, that appears to rotate about its polar axis. It is speculated that this rotation is related to the possible binarity of the central star. We are currently analyzing higher resolution interferometric CO maps, attempting to reveal the mechanism that drives this outflow rotation (Launhardt et al., in prep.). Due to the edge-on configuration, the bolometric luminosity listed in Table 7 is only a lower limit, while the  $L_{\text{SMM}} / L_{\text{bol}}$  ratio is an upper limit. Although the IR spectral index indicates a Class II source, the other evolutionary tracers and the estimated age of  $1\text{ Myr}$  (Launhardt et al. 2009) suggest it is a Class I YSO.

**CB 34** (Fig. 4) has the appearance of a Bok globule, but, with a distance of  $\sim 1.5\text{ kpc}$ , it is rather atypical and more massive than other Bok globules. It

has three dense cores and is associated with numerous young stars that seem to have formed from this cloud (Launhardt & Henning 1997; Alves et al. 1997; Huard et al. 2000). A water maser (Gómez et al. 2006) as well as several collimated outflows testify ongoing star formation activity. A bipolar CO outflow from cool gas (Yun & Clemens 1994b), shocked optical knots of atomic emission lines from radiative shocks (Herbig-Haro objects), as well as H<sub>2</sub> infrared jets (Yun & Clemens 1994a; Khanzadyan et al. 2002) have been reported. The chemical age of the globule was estimated to be  $> 10^5$  yr (Codella & Scappini 1998). The presence of a pre-main-sequence star, CB34FU, with an age of  $\sim 10^6$  yr supports this young age (Alves et al. 1997). Codella & Scappini (2003) studied the molecular gas of this globule and showed that the current star-formation activity is concentrated in the three main clumps which have sizes of  $\sim 0.25$  pc. Because of this complexity, we do not further investigate the individual sources in this globule, but only present our data.

**CB 39** is a small and not very opaque globule, located in direction of the Gemini OB1 cloud. It is associated with the well-known Herbig Ae/Be star HD 250550, the distance of which was derived with 700 pc. No mm dust continuum emission has been detected from this star, indicating that its circumstellar disk, if still present, cannot be very massive. Yun & Clemens (1994b) found a small, bipolar, low-velocity ( $\sim 3 \text{ km s}^{-1}$ ) CO outflow with not well-separated lobes. CB 39 has been observed in different molecular lines. It was detected in SO by Codella & Muders (1997) but not detected in CS by Launhardt et al. (1998). Sen et al. (2005) measured a magnetic field P.A. of  $150^\circ$ , based on the polarization of a number of background stars along the line of sight of the globule.

**CB 54** (LBN 1042; Fig. 5) is a relatively compact molecular cloud with the appearance of a Bok globule, but seems to be associated with the Vela OB1 cloud complex at a distance of 1.1 kpc. It contains a cluster of embedded young stars, visible on NIR images (Yun & Clemens 1994a; Yun 1996), as well as a cold IRAS point source (07020-1618) at the position of the mm peak and the embedded star cluster. CO observations revealed the presence of a collimated bipolar molecular outflow with well-separated lobes and centered on the IRAS point source (Yun & Clemens 1994b). This source is also associated with cm continuum emission (VLA AYO073; Yun et al. 1996). C<sup>18</sup>O observations suggests the presence of multiple cores with infall signatures (Wang et al. 1995). Gómez et al.

(2006) detected a water maser. Polarimetry of background starlight revealed a magnetic field with an average P.A. of  $116^\circ$  (Sen et al. 2005). Because of this complexity, we do not further investigate the individual sources in this globule, but only present our data.

**CB 58** (Fig. 6) is a relatively large, slightly elongated and cometary-shaped globule at a distance of 1.5 kpc. It is associated with IRAS point source 07161-2336 and the NIR images indicate the presence of several embedded YSOs. Afonso et al. (1998) concluded from HCN observations that the core represents a Class I evolutionary stage. Our (low-quality) mm dust continuum map suggests the presence of two dense cores in the head of the globule, where also the IRAS source and a number of reddened stars with associated nebulosities are located. However, none of the IR sources can be directly associated with one of the two dust clumps. Because of this complexity, we do not further investigate the individual sources in this globule, but only present our data.

**BHR 12** (CG 30, DC 253.3-1.6; Fig. 7) is a small, opaque, and very pronounced cometary globule with a bright rim, located in the Gum nebula region. The distance towards the Gum nebula clouds is somewhat uncertain, with estimates ranging from 200 pc (Knude et al. 1999) to 450 pc (Reipurth 1983). For consistency with earlier papers (e.g., Henning & Launhardt 1998), we use here 400 pc. The globule has an angular diameter of  $\sim 2.3'$  and its tail (which merges with the tail of CG 31) has a length of  $25'$  (Reipurth 1983). At its head side, CG 30 harbors two protostellar cores with a projected separation of  $\sim 20''$  ( $\sim 8000$  AU), embedded in a common envelope (Launhardt et al. 2000). The northern source (SMM 1, CG 30N) is associated with the IRAS point source 08076-3556 and a NIR source, which drives the Herbig-Haro flow HH 120 (see Hodapp & Ladd 1995, and references therein). The southern core (SMM 2, CG 30S; Launhardt et al. 2001) is the origin of a protostellar jet with position angle  $44^\circ$  (Hodapp & Ladd 1995), but no NIR counterpart is seen at this position. Both cores are detected in all IRAC bands (Chen et al. 2008b). The IRAC  $4.5 \mu\text{m}$  image also shows bipolar jets, which have been traced in CO(2–1) using the SMA (Chen et al. 2008a). Fig. 7 shows that the two cores are well resolved at 450 and  $850 \mu\text{m}$ , though they are surrounded by a common envelope. The cores are unresolved in our 1.3 mm map. The SED is well sampled for both cores, and shows that SMM 2 is colder or more heavily extincted than SMM 1. We classify SMM 1 as a Class I YSO, based

on its bolometric temperature (see Table 7). The low bolometric temperature of 50 K suggests that SMM 2 is a Class 0 protostar and thus younger than SMM 2. BHR 12 is thus one of those globules that contain two or more sources of different evolutionary stage within a few thousand AU (see Sect. 4.2 and Table 6).

**BHR 36** (DC 267.4-7.5; Fig. 8) is a cometary-shaped globule in the Vela sheet at a distance of 400 pc. A dense core, mapped at 1.3 mm continuum, is located at the head side of the globule. The mm emission peaks at the position of the IR source detected both by IRAS and *Spitzer* and at the center of a bipolar jet seen on NIR images. Two Herbig-Haro objects, HH46/47, are associated with a collimated bipolar outflow centered at this position (Dopita et al. 1982). From their observations of  $^{13}\text{CO}(2-1)$ , Löhrl et al. (2007) derive a total mass of  $255 \pm 60 M_{\odot}$  and a size of  $\sim 1.3$  pc for the entire globule. In their ammonia survey, Bourke et al. (1995b) obtain a mass of  $\sim 11 M_{\odot}$  within the central 0.3 pc for the dense core. They also derive a kinetic temperature of  $T_k = 18$  K in the centre. The chemical age of the globule was estimated to be  $\sim 0.1$  Myr (Cecchi-Pestellini et al. 2001). BHR 36 is too far south for the JCMT to observe. Like for the other southern globules, we are therefore limited to the 1.3 mm maps. The fit to the SED of this source indicates  $T_{\text{bol}}$  of  $\approx 150$  K (see Table 7). We therefore classify the embedded YSO as a Class I source.

**BHR 55** (DC 275+1.9; Fig. 9) is an average-sized, low-extinction globule, associated with the annulus of cometary globules in the Vela-Gum complex (Bourke et al. 1995a), though it has not a very pronounced cometary appearance. Bourke et al. (1995b) estimate the distance to the globule to be 300 pc by looking at the reddening of background stars. From ammonia observations, Bourke et al. (1995b) derive kinetic and rotational temperatures of 13 K and 12 K respectively, a central volume density of  $8.1 \times 10^3 \text{ cm}^{-3}$ , and a core mass of  $3.7 M_{\odot}$ . The globule is too far south to observe with JCMT, therefore only the 1.3 mm data constrain the long-wavelength end of the SED. The very compact (unresolved) mm source is associated with an IRAS point source (09449-5052), but has no near-infrared counterpart. Due to the lack of data at submm and MIR wavelengths, the SED is not well-constrained. However, the low  $T_{\text{bol}}$  of  $\approx 40$  K suggests this is a Class 0 protostar.

**BHR 71** (DC 297.7-2.8; Fig. 10) is a very opaque, elongated globule located near the southern Coalsack at an estimated distance of  $\sim 200$  pc. At its center, the

globule contains a dense protostellar core, which emits strong mm dust continuum emission and is detected by various instruments down to MIR wavelengths. Observations with higher angular resolution revealed that this is actually a double core (Myers & Mardones 1998) with two embedded IR sources, IRS 1 and IRS 2, separated by  $17''$  (3400 AU – Bourke 2001). Outflows are seen in the  $\text{H}_2 \nu = 1 - 2 \text{ S}(1)$  line emanating from both sources. A highly collimated molecular outflow has been detected (Bourke et al. 1997) which is associated with two Herbig-Haro objects (HH 320 and HH 321; Corporon & Reipurth 1997). Bourke (2001) and Parise et al. (2006) resolved it into two outflows, mapping CO and methanol, and found that the IRS 2 outflow is significantly hotter than the IRS 1 outflow. From  $^{13}\text{CO}(2-1)$  measurements, Löhrl et al. (2007) derived a mass of  $12 \pm 4 M_{\odot}$  for the entire cloud. From their ammonia measurements, Bourke et al. (1995b) derived a mass of  $2.2 M_{\odot}$  for the dense core and Bourke et al. (1997) derive  $2.4 M_{\odot}$  from the 1.3 mm dust continuum map. The 1.3 mm continuum image does not resolve the two sources, but the low  $T_{\text{bol}}$  of the combined SED indicates that at least IRS 1 (the brighter source at the mm peak position) is a Class 0 protostar. This is in agreement with earlier work (Bourke et al. 1997).

**BHR 86** (DC 303.8-14.2; Fig. 11) is a cometary-shaped globule located in the Chameleon dark cloud complex at a distance of 150 to 180 pc. Löhrl et al. (2007) carried out  $^{12}\text{CO}(2-1)$  observations and measured a size of  $15' \times 15'$  and a mass of  $19 \pm 4 M_{\odot}$ . From *ISO* observations, Lehtinen et al. (2005) derived central dust temperature of  $14 \pm 1$  K and a mass of  $2.7 M_{\odot}$  for the dense core and concluded that the embedded source is a Class 0/I transition object. They also showed that the main heating source of the dense core is not the embedded source, but the interstellar radiation field. From CS(2-1),  $\text{HCO}^+(1-0)$  and HCN(1-0) line profiles Lehtinen (1997) could classify BHR 86 as a core with simultaneous infall of dense gas in the centre and a non-collapsing envelope. They also detected a bipolar molecular outflow in  $^{12}\text{CO}(1-0)$ . NIR observations in  $JHK_s$  showed an exponential extinction profile with  $p = 2.29 \pm 0.08$  (Kainulainen et al. 2007). From the low bolometric temperature of  $\approx 60$  K, the high  $L_{\text{submm}} / L_{\text{bol}}$  ratio of  $\approx 6\%$ , and the absence of a NIR source we conclude this is a Class 0 protostar, which is in agreement with the *ISO* observations.

**CB 68** (L 146; Fig. 12) is a small, nearby, slightly cometary-shaped opaque Bok globule located in the

outskirts of the  $\rho$ Oph dark cloud complex at a distance of  $\sim 160$  pc. The dense core of the globule is associated with a cold IRAS point source (16544-1604) and exhibits strong, extended, but centrally peaked sub(mm) dust continuum emission (Launhardt & Henning 1997; Launhardt et al. 1998; Vallée et al. 2000). No NIR source is detected at  $2.2\mu\text{m}$ . The central source, which was classified as a Class 0 protostar (Launhardt & Henning 1997), drives a weak, but strongly collimated bipolar molecular outflow at P.A.  $142^\circ$  (Wu et al. 1996; Mardones et al. 1997; Vallée et al. 2000). Vallée et al. (2000) also performed submm continuum polarization measurements at  $850\mu\text{m}$  and found a large linear polarization of 10%, indicating that Bok globules can have well ordered magnetic fields, and suitable conditions for grain alignment. The SED, which is well-sampled between the 1.3 mm IRAM data and the NIR IRAC data, indicates a  $T_{\text{bol}}$  of  $\sim 50$  K (Table 7), confirming the classification as a Class 0 protostar (Fig. 26).

**BHR 137** (DC 344.6-04.3; Fig. 13) is a small, opaque, and elongated globule with a diffuse tail. The distance is somewhat uncertain. Vilas-Boas et al. (2000) associate the core with the nearby Scorpius region at a distance of 145 pc, whereas (Bourke et al. 1995b) derive a distance of 700 pc, based on measuring the reddening of background stars. We adopt here the latter distance estimate. At the northern rim of the globule, outside the dark core, there are several red stars with associated nebulosities. An IRAS point source (17181-4405) appears to be associated with the southern-most of these stars. For the dense core, which is located south of the nebulous stars and elongated north-south, Bourke et al. (1995b) estimate a lower mass limit  $8.7 M_\odot$  from  $\text{NH}_3$ . We derive a total mass of  $26 M_\odot$  from the 1.3 mm dust continuum map. BHR 137 was not observed by *Spitzer* and our observations do not permit to compile a reliable SED for this source. Therefore, we cannot evaluate the evolutionary stage of this core, although the high mass and lack of NIR sources at the position of the mm peak suggest a rather early evolutionary stage. Due to the large distance and low angular resolution of our SEST map, we can also not evaluate the possible multiplicity of this massive elongated dust core.

**CB 130** (L 507; Fig. 14) is a small, slightly elongated globule located in the Aquila rift at a distance of 200 pc. There is no IRAS point source associated with this globule. Launhardt & Henning (1997) detected only weak mm-continuum emission in its centre and

Yun et al. (1999) concluded from the weakness of the  $\text{HCN}(1-0)$  emission that there is no embedded YSO. Since there is also no evidence of outflows, the source was originally classified as a pre-stellar core by Launhardt & Henning (1997). However, our (sub)mm maps show that CB 130 is well detected in all bands (see Fig. 14). The core is resolved into two separate compact sources, separated by  $30''$  ( $\sim 6000$  AU) and surrounded by a common envelope. The brighter source, SMM 1, is associated with a faint NIR source, which is also detected by *Spitzer* up to  $24\mu\text{m}$  (there are no useable data at longer wavelengths). A very red star, which we call IRS, is located  $14''$  ( $\sim 3000$  AU) east of SMM 1 (Figs. 14b and 28). At  $24\mu\text{m}$ , this star is still 1.3 times brighter than the IR source associated with SMM 1. However, as none of the (sub)mm maps shows a local maximum at this position, source IRS does not seem to have detectable mm dust continuum emission associated. We conclude that the spatial coincidence between IRS and the dust core is a projection effect and the source is located outside the dust core. We could compile a SED for SMM 1, separating the fluxes from IRS at short wavelengths and from SMM 2 at (sub)mm wavelengths. The low  $T_{\text{bol}}$  of  $\sim 55$  K and high  $L_{\text{submm}} / L_{\text{bol}}$  ratio of  $\sim 10\%$  suggest SMM 1 is a Class 0 protostar, although the NIR/MIR SED is rather indicative of a Class I YSO (see Fig. 25). The IR SED of IRS ( $\alpha_{\text{IR}} = -0.7$ ) suggests this is a Class II YSO, but we don't have strong constraints on its FIR to (sub)mm SED. The (sub)mm SED of SMM 2 has a somewhat steeper slope than SMM 1 and there is no IR counterpart detected, indicating that this core does not have an embedded heating source. We therefore assume that this is a very low-mass prestellar core. CB 130 is thus one of those globules that contain two or more sources with different evolutionary stage within a few thousand AU (see Sect. 4.2 and Table 6).

**CB 188** (L 673-1; Fig. 15) is a small, roundish, and opaque globule with a detached diffuse tail. It is located towards Aquila at a distance of  $\sim 300$  pc and is associated with the Lindblad ring. The dense core of the globule is associated with a cold IRAS point source (19179+1129) and exhibits strong, extended, but centrally peaked sub(mm) dust continuum emission. At the peak of the mm emission and the IRAS position, there is a very red star, indicating that the bulk of the compact mm dust emission does not arise from an optically thick envelope, but rather from a circumstellar disk. The source drives a bipolar molecular outflow at P.A.  $= 75^\circ$  with a mass loss rate of



$\sim 6.6 \times 10^{-7} M_{\odot}/\text{yr}$  (Yun & Clemens 1994b). The red and blue lobe have a strong overlap, indicating that the source is seen almost pole-on. This is consistent with seeing a strong NIR source at the peak of the mm continuum emission. The source shows only weak  $\text{N}_2\text{H}^+(1-0)$  emission which can be caused by destruction due to CO, which is released from grain surfaces in outflows (Chen et al. 2007). Our fit to the SED, which is well-sampled between  $1.25 \mu\text{m}$  and  $3 \text{ mm}$ , indicates  $T_{\text{bol}} \approx 300 \text{ K}$ . We conclude that CB 188 SMM is a Class I YSO, exhibiting a relatively massive circumstellar disk, surrounded by an extended envelope. We thus confirm earlier classifications (e.g., Afonso et al. 1998).

**CB 199** (B 335, L 663; Fig. 16) is a roundish, very opaque, relatively isolated, and well-studied prototypical Bok globule, located towards Aquila (see Stutz et al. 2008, and references therein). Its distance was recently redetermined to be only  $90 - 120 \text{ pc}$  (Olofsson & Olofsson 2009). The globule contains a single compact core at its center, that is detected at far-infrared wavelengths and is very bright in the submillimetre range (Keene et al. 1983; Chandler et al. 1990). Zhou et al. (1993) have found evidence for mass infall onto the central source, which was confirmed by observations in a CO rare isotope (Chandler & Sargent 1993) and by CSS observations (Velusamy et al. 1995). The source drives a well-collimated bipolar molecular outflow (Frerking & Langer 1982). Furthermore, a number of HH objects have been detected both at optical wavelengths (Vrba et al. 1986; Reipurth et al. 1992) and in the  $1-0 \text{ S}(1)$  line of  $\text{H}_2$  (Hodapp 1998). This combination of characteristics that makes the central embedded source in B 335 one of the clearest examples of a Class 0 protostar. Gómez et al. (2006) found a water maser with a high velocity shift ( $\sim 30 \text{ km/s}$ ) compared to the cloud velocity. This could be evidence for a protoplanetary or young planetary disk. The low  $T_{\text{bol}}$  of  $37 \text{ K}$  that is derived from our fit to the SED corroborates the earlier classification.

**CB 205** (L 810; Fig. 17) has the appearance of a Bok globule, but, with a distance of  $2 \text{ kpc}$ , its apparent size of  $8'$  corresponds to a diameter of  $4.8 \text{ pc}$ . It is thus much larger and more massive than other Bok globules. SCUBA observations revealed the presence of a large submm core with two condensations, separated by  $\approx 45''$  (Huard et al. 2000). The first and more massive core (CB205-SMM1) coincides with the IRAS source 19433+2743 and has a mass of  $10 M_{\odot}$ . The total of mass of the dense core is estimated to be

$120 M_{\odot}$ . The cloud is known to harbour many optical and NIR sources. Neckel & Staude (1990) showed that at least 12 stars are associated with CB 205 and are located in the eastern part of the cloud. A very bright and red source (L 810 IRS) with a bolometric luminosity of  $890 L_{\odot}$  is the illumination source for a NIR nebula (Yun et al. 1993; Massi et al. 2004). This nebula is hourglass-shaped and has an extent in NS direction of  $20''$ . It has the same orientation as the molecular outflow, which shows a strong overlap of the blue and red lobes. The peak of  $^{13}\text{CO}$  intensity map coincides with the IRAS source (Yun & Clemens 1994b). In the western part, Codella et al. (2006) detected three Class 0 sources with enhanced high velocity outflow activity, suggesting that the star formation propagates through CB 205 as the NIR cluster represents a later evolutionary stage. Neckel et al. (1985) also found water maser emission of  $7.5 \text{ Jy}$  towards L 810, which could not be confirmed in later observations (Gómez et al. 2006). Although the entire source was classified as Class I source by Afonso et al. (1998), we find that this complexity does not allow us to construct meaningful SEDs or to reliably interpret a possible integrated SED. Therefore, we do not further investigate the individual sources in this globule or discuss its evolutionary stage, but only present our data.

**CB 224** (L 1100; Fig. 18) is a small, roundish globule with a large visible cloudshine halo (like most globules). It is located in the northern Cygnus region at  $d \sim 400 \text{ pc}$ . The core of the globule contains two mm sources, separated by  $\approx 35''$ , both detected at all three (sub)mm bands. The northeastern source (SMM 2) is associated with the cold IRAS source 20355+6343 and with a red star which is also seen at optical wavelengths. The SED of this source indicates a  $T_{\text{bol}}$  of  $340 \text{ K}$  and we classify this source as a Class I YSO. The southwestern source (SMM 1), which is the brighter mm source, is associated with a very faint and diffuse NIR nebula. This source drives a collimated  $^{13}\text{CO}$  bipolar outflow at P.A. =  $-120^\circ$  (Chen et al. 2007).  $\text{HCO}^+(1-0)$  observations clearly show evidence of infall towards the core center (De Vries et al. 2002). CB 224 was not observed with *Spitzer*. The SED is therefore not well-constrained at MIR/FIR wavelengths and we rely on aperture photometry in IRAS maps Gezari et al. (1999). The SED of this source indicates a  $T_{\text{bol}}$  of  $56 \text{ K}$  and we classify it as a Class 0 protostar.

**CB 230** (L 1177; Fig. 19) is a small, slightly cometary-shaped, bright-rimmed Bok globule lo-

cated in the Cepheus Flare region at a distance of  $\sim 400 \pm 100$  pc. The dark globule has a low-extinction tail, which is clearly visible on optical images by its cloudshine, that connects to the bright nebula Sh 2-136. At its southern rim, the globule contains a dense core that is associated with two NIR reflection nebulae, separated by  $\sim 10''$  (Yun 1996; Launhardt 1996, 2001). The brighter, western nebula (IRS 1), has a conical shape with the origin at the mm peak position. The fainter eastern nebula (IRS 2) is also located inside the mm core, but seems to exhibit much less dust emission than IRS 1. An IRAS point source (21169+6804) is located between the two NIR nebula, indicating that both sources contribute to the IRAS PSC fluxes. CB 230 was classified by Froebrich (2005) as a Class 0/I transition object. CB 230 was also observed in several molecular lines and was found to exhibit signatures of mass infall. Its virial mass was determined to be  $12 M_{\odot}$  (CS) and  $8 M_{\odot}$  ( $C^{18}O$ ), respectively (Launhardt et al. 1998; Launhardt 2001). The dense core is associated with a large-scale collimated CO outflow with  $6.6 \times 10^{-7} M_{\odot}/\text{yr}$  at P.A. =  $7^{\circ}$  and a dynamical age of  $\sim 2 \times 10^4$  yr (Yun & Clemens 1994b). This outflow was resolved by Launhardt (2001) into two misaligned bipolar flows, the stronger one originating at IRS 1 and the weaker one at IRS 2. The NIR nebulae can thus be interpreted as forward-scattered light emanating from those outflow cones that are directed towards us. Observations of [FeII] and weak  $H_2$  emission in the jet suggest the presence of fast, dissociative J-shocks (Massi et al. 2004). Magnetic field strength and projected direction in the dense core were derived by submm polarimetry to be  $B = 218 \pm 50 \mu\text{G}$  and P.A. =  $-67^{\circ}$ , respectively (Wolf et al. 2003). Earlier work by Vallée et al. (2000) is consistent with this picture. Since the two embedded sources are only resolved at wavelengths shorter  $25 \mu\text{m}$ , we cannot compile complete separate SEDs. However, the NIR luminosity ratio and the submm maps indicate that IRS 1 is the more massive and luminous source that dominates the SED at all wavelengths. The combined SED and the resulting  $T_{\text{bol}}$  of  $\approx 210$  K should thus be representative for IRS 1. While the bolometric temperatures and high  $L_{\text{submm}} / L_{\text{bol}}$  ratio suggests a Class I YSO with a significant envelope, the  $\alpha_{\text{IR}}$  value of the double-peaked SED indicates Class II (see discussion in Sect. 4.1). From the similarity of the NIR/MIR SEDs and the spatial proximity, we also conclude that IRS 2 is at the same evolutionary stage, but less massive, and has formed from the same initial core as IRS 1.

**CB 232** (B 158; Fig. 20) is a small, slightly cometary-shaped globule which is associated with the Sh 2-126 cloud at a distance of 600 pc. Using SCUBA observations, Huard et al. (1999) detected a submm double core with the two components having different evolutionary stages and masses of  $0.3 M_{\odot}$  and  $0.1 M_{\odot}$  respectively. The total mass was derived to be  $6 M_{\odot}$ . The more evolved object, which we call here IRS and which presumably can be associated with a nearby NIR star and IRAS source 21352+4307, was classified to be a Class I source (Yun & Clemens 1995). The main submm core (with no NIR counterpart; called here SMM) is a candidate Class 0 protostar. A bipolar outflow with poor collimation at P.A. =  $-30^{\circ}$  (Yun & Clemens 1994b) cannot clearly be associated with either of the two sources. The virial mass of the entire dense core was derived with  $42 M_{\odot}$  (CS) and  $16 M_{\odot}$  ( $C^{18}O$ ), respectively (Launhardt et al. 1998). CB 232 is also currently the smallest Bok globule that is known to harbour a water maser (Gómez et al. 2006). Although our submm maps, except for the low SNR  $450 \mu\text{m}$  map, do not resolve the two embedded sources (SMM and IRS1), we tried to decompose the emission into an extended envelope and two compact gaussian sources at the positions of the mm peak and the red star. The resulting individual source fluxes at  $850 \mu\text{m}$  are somewhat higher than estimated by Huard et al. (1999) and the relative uncertainty is of the order 50%, but they can be used to constrain the SED of source IRS fairly well. The *Spitzer* maps show that even at  $70 \mu\text{m}$  source IRS1 completely dominates and there is no trace of emission detected from the position of source SMM, indicating that the dust core has no or only a very low-luminosity internal heating source (see Fig. 28 for the  $24 \mu\text{m}$  image). Source SMM is thus more likely prestellar than protostellar. The SED for IRS1, which may contain some unknown but small contribution from SMM around  $100 \mu\text{m}$ , indicates a  $T_{\text{bol}}$  of  $\approx 170$  K. We classify IRS1 as a Class I YSO. A second IR source (IRS2), located  $\approx 40''$  south of SMM, is seen on all *Spitzer* images and seems to be associated with the globule, but we don't compile an SED or classify this source. CB 232 is one of those globules that contain two or more sources of different evolutionary stage within a few thousand AU (see Sect. 4.2 and Table 6).

**CB 240** (L 1192; Fig. 21) is a small, roundish globule with a diffuse tail, located in the Cepheus Flare region. Its distance is estimated to be  $\sim 500$  pc, but this is rather uncertain. IRAS source 22317+5816,

which has been identified as a Class II-D YSO (Yun & Clemens 1995), is located outside the visible boundary of the globule,  $\approx 2'$  to the south-east. In a NIR survey, Yun & Clemens (1994a) detected a red object at the IRAS position, but no nebulosity or evidence of multiplicity. Launhardt & Henning (1997), however, identify a cluster of young stars at the IRAS position (see Fig. 21b), and calculate the bolometric luminosity of the associated core to be  $7.3 L_{\odot}$ . CB 240 has been detected in a number of molecular transitions, including  $C^{18}O$ ,  $NH_3$ ,  $HCO^+$  and  $SO$  (Wang et al. 1995; Turner 1995a,b,c). No outflow has been detected from this source (Yun & Clemens 1992). CB 240 is detected in our dust continuum maps with a low signal-to-noise ratio at  $850 \mu m$  and  $1.3 mm$ . It is not detected at  $450 \mu m$ . Since the IRAS source and mm core is located outside the optical boundaries of the globule and is obviously composed of a small cluster of young stars with a diffuse common dust envelope, we cannot discriminate and classify individual sources. Therefore, we do not show a SED and do not further discuss this source here.

**CB 243** (L 1246; Fig. 21) is an opaque, very elongated, filamentary-like globule with a long dark tail pointing eastward, located at a distance of 700 pc in the Cep OB3 region. A head-like, very opaque extension at its western end contains a dense core that is currently forming one or more stars. Extended submm dust emission is traced from the entire western part of the globule, with two embedded compact sources: SMM 1 in the western head of the globule and SMM 2 towards the center of the globule (Visser et al. 2001). SMM 1 is associated with the IRAS source 23228+6320 and was classified a Class 0/I transition source (Froebrich 2005) with a bolometric luminosity of  $10 L_{\odot}$  (Launhardt & Henning 1997). Visser et al. (2001) also detected a molecular outflow from SMM 1 in  $^{12}CO(2-1)$ , with a dynamical age of  $4.6 \times 10^4$  yr and masses of  $0.004 M_{\odot}$  in the red and  $0.015 M_{\odot}$  in the blue lobe, respectively. Our data confirm the general morphology of the dust emission from this globule. However, we find that the dust core SMM1 is clearly offset by  $\sim 10''$  to the north-west with respect to IRS (see Fig. 21b). This offset is larger than the pointing uncertainty of the mm telescopes and is confirmed independently in both the IRAM and SCUBA maps. Unfortunately, the *Spitzer* IRAC maps cover only the bulk of the globule containing SMM2, but not the head with SMM 1. They show that SMM2 has an  $8 \mu m$  shadow and does not contain an embedded heating source. We therefore assume that SMM2 is a prestellar core. How-

ever, the MIPS  $24 \mu m$  map shows clearly that there is a point-like MIR source at the IRAS position close to SMM 1, but no emission is detected at the center position of SMM 1, indicating that the dust core has no or only a very low-luminosity internal heating source (see Fig. 28 for the  $24 \mu m$  image). Since we cannot separate the SEDs of the two sources (SMM 1 and IRS) and it is unclear from which of them the molecular outflow originates, we cannot clearly classify the sources in terms of their evolutionary stage. We can only speculate that IRS is a low to intermediate-mass Class I YSO that has most likely formed in CB 243, and that SMM 1 is most likely a  $5 - 10 M_{\odot}$  prestellar core. This of course also makes invalid the classification attempts by Visser et al. (2002) and Froebrich (2005), who assumed that all fluxes arise from one source. CB 243 is thus one of those globules that contain two or more sources of different evolutionary stage within a few thousand AU (see Sect. 4.2 and Table 6).

**CB 244** (L 1262; Fig. 23) is a medium-sized, slightly elongated globule located in the Cepheus region and most likely related to the Lindblad ring at a distance of  $\approx 200$  pc. The globule contains two (sub)mm cores, surrounded by extended envelopes. The brighter (at submm wavelengths) and more compact core (SMM 1) is associated with a faint NIR reflection nebula and a cold IRAS point source (23238+7401). The SED of this source is well-sampled between NIR and mm wavelengths and we derive  $T_{bol} \approx 70$  K. The source drives a collimated bipolar molecular outflow with total mass  $0.07 M_{\odot}$  (Terebey et al. 1989; Yun & Clemens 1994b). We confirm earlier classifications of CB 244 SMM 1 as a Class 0 protostar, although it is probably more evolved than, e.g., B 335. The second core, SMM 2, which is located  $\approx 90''$  (18,000 AU) north-west of SMM 1, is much less compact and only detected at low signal-to-noise in the  $850 \mu m$  and  $1.3 mm$  maps. There is no indication of an embedded source in this core. Rather, it is seen as a dark shadow in the  $8 \mu m$  IRAC 4 map (Tobin et al. 2010) and in the  $24 \mu m$  MIPS map (Stutz et al. 2010). We therefore assume that SMM 2 is a prestellar core (cf. Stutz et al. 2009). For the region between the two submm-cores, Wolf et al. (2003) observed an alignment of the polarization vectors parallel to the gas/dust bridge connecting the two cores. This could be a trace of mass infall along field lines in the early stages of star formation. In the outflow region around SMM 1, the polarization vectors tend to align with the direction of the outflow.

**CB 246** (L 1253; Fig. 24) is a medium-sized, dark, roundish globule with a narrow tail pointing southeast. It is most likely associated with the Lindblad ring, the distance to which in this direction is  $\sim 140$  pc. The globule has an extended complex core that is fragmented into at least two elongated sub-cores, but no compact embedded sources have been found. *Spitzer IRAC* images show the two sub-cores as strong  $8\mu\text{m}$  shadows. Lemme et al. (1996) and Codella & Scappini (1998) observed CB 246 in  $\text{C}_2\text{S}(2-1)$  and  $\text{NH}_3$ . They also identified the two sub-cores and derived their total mass with  $\approx 7 M_\odot$ . They conclude that this source as inactive, with neither a water maser nor molecular outflow. Crapsi et al. (2005) concluded from the observed low  $\text{N}_2\text{D}^+/\text{N}_2\text{H}^+$ -fraction that CB 246 is still in a very early evolutionary phase. Lee et al. (2001) classified CB 246 as having significant red excess, but no blue asymmetry in the CS spectra, indicating that the core has not begun to collapse. Recently, Sen et al. (2005) and Ward-Thompson et al. (2009) derived the orientation of the magnetic field by measuring the polarization of background stars. They find that the magnetic field has a mean angular offset from the short axis of the globule core of  $28 \pm 20$  deg. Like for other globule they have studied, this hints towards magnetic fields not governing the star formation in these clouds. Because the source is not detected at wavelengths shorter than  $450\mu\text{m}$ , we cannot compile a meaningful SED. We conclude that CB 246 contains at least two starless cores, possibly prestellar in nature, thus confirming earlier classifications. Sub-core SMM 2 is fairly elongated and might be fragmented into a chain of sub-clumps.

## 6. Summary and conclusions

We have studied the dense cores of 32 Bok globules and have obtained deep NIR images and (sub)mm dust continuum maps at up to three wavelengths (0.45, 0.85, and 1.3 mm). With the exception of a small control sample, all sources were selected from earlier surveys which identified them as good candidates for having ongoing star formation, i.e., this is not an unbiased survey. We also compiled SEDs, taking special care of separating the flux contributions from different neighbouring sources at different wavelengths, and fitted them to derive various source quantities and evolutionary stages of the sources. The main results of this study are:

1. We detected (sub)mm dust continuum cores in

26 out of the 32 globules observed. The tentative, low SNR, single-dish 1.3 mm continuum detections in CB 52 and BHR 41, published in and earlier paper, could not be confirmed.

2. Eight of the 26 globules with detected (sub)mm cores are not studied in further detail or evaluated in terms of their evolutionary stage because they were either at too large distances ( $> 1$  kpc) and multiple embedded sources were not resolved, or the (sub)mm maps were of too low quality, or we simply did not have enough data to draw any reliable conclusions.
3. In 18 globules with detected (sub)mm cores, we derived evolutionary stages and physical parameters of the embedded sources. In total, we identified nine starless cores, presumably prestellar, nine Class 0 protostars, and eleven Class I YSOs in these 18 globules.
4. We find that the bolometric temperature is the most reliable tracer to discriminate between Class 0 protostars and Class I YSOs and confirm the empirical boundary of 70 K. The spread of  $L_{\text{smm}} / L_{\text{bol}}$  ratios within the Class 0 and Class I groups is relatively large (2 – 10% within Class 0 and 0.8 – 3.5% within Class I), with no significant correlation between  $T_{\text{bol}}$  and  $L_{\text{smm}} / L_{\text{bol}}$  within the groups. However, the three most evolved Class I sources, with visible stars and compact (sub)mm emission arising presumably from circumstellar disks, also have the lowest  $L_{\text{smm}} / L_{\text{bol}}$  ratios ( $\leq 1.3\%$ ). We take this as tentative indication that the  $L_{\text{smm}} / L_{\text{bol}}$  ratio, as indicator of envelope dispersal, may better trace the evolution within the Class 0 and Class I phases.
5. The mean FWHM core sizes decrease from 8,000 AU for prestellar cores, to 3,000 AU for Class 0 protostars, to  $< 2,000$  AU for Class I YSOs. The latter group also exhibits extended remnant envelopes with diameters of order 20,000 AU. Source-averaged volume densities,  $n_{\text{H}}$ , increase from  $1 \times 10^7 \text{ cm}^{-3}$  for prestellar cores, to  $7 \times 10^7 \text{ cm}^{-3}$  for Class 0 protostars, to  $> 8 \times 10^7 \text{ cm}^{-3}$  for Class I YSOs. The extended envelopes of the Class I YSOs have a mean density of  $7 \times 10^4 \text{ cm}^{-3}$ .
6. At least two thirds (16 out of 24) of the star-forming globules studied here show evidence of

forming multiple stars on scales between 1,000 and 50,000 AU, either as multiple star-forming cores, wide embedded binaries, or small star clusters. The fraction of closer binaries formed from unresolved mm cores might be higher, but remains unknown from this study.

7. We find that the large majority of these small protostar and star groups in globules with multiple star formation are comprised of sources with different evolutionary stages. This includes neighbouring mm sources with obviously different evolutionary stages, prestellar or protostellar cores with nearby IR sources, presumably more evolved protostars or Class I YSOs, as well as NIR star clusters next to large (sub)mm cores with the potential to form more stars. In only three globules we find coeval pairs, ranging from multiple pre-stellar cores in CB 246, embedded Class 0 protostars in BHR 71, to an embedded Class I YSOs pair in CB 230. This widespread non-coevality possibly suggests a picture of slow and sequential star formation in isolated globules.
8. These findings also call for special attention when compiling SEDs and attempting to derive source properties from flux measurements with insufficient angular resolution. One may easily end up classifying the combined SED of a prestellar core and a nearby, more evolved YSO as a Class 0 protostar.

While this paper presents an extensive, though not complete inventory of star-forming cores in nearby Bok globules, it remains subject of other detailed studies to investigate the physical and chemical properties, multiplicity and evolutionary stages of individual sources, and to evaluate if and how star formation in isolated globules differs from that in larger molecular cloud complexes. We expect soon to obtain spatially resolved mid to far-infrared Herschel data for many of the globule cores presented here and plan to use these data to accurately measure the dust temperature profiles and derive more reliable density profiles. In particular for the prestellar cores, which characterize the initial conditions of the protostellar collapse, this may lead to significant corrections of previous estimates of mass and density distributions which were often hampered by the lack of temperature measurements. Furthermore, we are currently working on detailed studies of two globule cores which characterize the stage of the

onset of the protostellar collapse and which may shed light on the non-coeval evolution of different sub-cores within one globule (Schmalzl et al., in prep.). Last, but not least, this paper shall provide some guidance for further follow-up studies of individual globules, e.g., with Herschel, SCUBA2, and ALMA.

The authors would like to thank the staff at all of the telescopes where data for this paper were obtained. The JCMT is operated by the JAC, Hawaii, on behalf of the UK STFC, the Netherlands OSR, and the National Research Council (NRC) of Canada. This research used the facilities of the Canadian Astronomy Data Centre (CADC) operated by the NRC of Canada with the support of the Canadian Space Agency. This paper is partially based on observations collected at the European Southern Observatory, La Silla, Chile. This work is also based in part on observations made with the Spitzer Space Telescope, which is operated by the Jet Propulsion Laboratory, California Institute of Technology under a contract with NASA. This publication makes use of data products from the Two Micron All Sky Survey, which is a joint project of the University of Massachusetts and the Infrared Processing and Analysis Center/California Institute of Technology, funded by the National Aeronautics and Space Administration and the National Science Foundation. Partial support for T.L.B. was provided by NASA through contracts 1279198 and 1288806 issued by the Jet Propulsion Laboratory, California Institute of Technology, to the Smithsonian Astronomical Observatory. We also thank J. Steinacker and A. Stutz for helpful discussions and critical reading of the manuscript. Last, but not least, we also acknowledge helpful comments by the anonymous referee, which helped to improve the clarity of the paper.

Facilities: IRAM:30m(MPIfR 1-channel, 7-channel, 19-channel bolometers), SEST(SIMBA), JCMT(SCUBA), CAO:3.5m(MAGIC,  $\Omega$ PRIME), Max Planck:2.2m(IRAC-2B), Spitzer(IRAC,MIPS)

### A. Optical depth conversion for JCMT

For the JCMT data, the optical depths quoted in Table 3 refers to 225 GHz. To convert to  $\tau_{850}$  and  $\tau_{450}$ , the following conversions (Archibald et al. 2002) can be used for dates prior to October 1999:

$$\tau_{850} = 3.99(\tau_{225GHz} - 0.004), \quad (\text{A1})$$

$$\tau_{450} = 23.5(\tau_{225GHz} - 0.012). \quad (\text{A2})$$

For dates post December 1999, the following conversions apply:

$$\tau_{850} = 4.02(\tau_{225GHz} - 0.001), \quad (\text{A3})$$

$$\tau_{450} = 26.2(\tau_{225GHz} - 0.014). \quad (\text{A4})$$

The change is due to the different filters which were installed in SCUBA in 1999.

TABLE 1  
TYPICAL PROPERTIES OF BOK GLOBULES AND THEIR DENSE CORES

	Globule	Dense Core
Mass	5 - 50 $M_{\odot}$	0.5 - 5 $M_{\odot}$
Size	0.2 - 1 pc	0.02 - 0.05 pc
Mean density	$10^3 \text{ cm}^{-3}$	$10^7 \text{ cm}^{-3}$
Gas temperature	15 K	10 K
Line widths	0.5 - 2 $\text{km s}^{-1}$	0.4 - 0.7 $\text{km s}^{-1}$

TABLE 2  
COORDINATES AND DISTANCES OF THE OBSERVED GLOBULES

Name	Other names <sup>a</sup>	IRAS source	R.A. <sup>b</sup> (1950)	Dec. <sup>b</sup> (1950)	$D$ (Ref.) [pc]	NIR	Observation codes <sup>c</sup> 450&850 $\mu\text{m}$	1.3 mm
CB 4	...	...	00:36:15.0	+52:35:00	600 (11)	CA02	...	I96/97
CB 6	LBN 613	00465+5028	00:46:33.8	+50:28:25	600 (1)	CA93	J97a	I95
CB 6 N	...	...	00:46:50.0	+50:39:45	600 (1)	...	...	I96/97
CB 17 SW	L 1388	...	03:59:16.4	+56:42:27	250 (1)	...	...	I96
CB 17	L 1389	04005+5647	04:00:31.3	+56:47:58	250 (1)	CA95	J98d	I95
CB 26	L 1439	04559+5200	04:55:54.7	+52:00:15	140 (3)	CA93	J00a	I96
CB 34	...	05440+2059	05:44:04.7	+20:58:54	1500 (2)	CA93	J97d/98a	I95
CB 39	(HD250550)	05591+1630	05:59:06.0	+16:30:58	700 (4)	CA93	...	I95
CB 52	...	06464-1650	06:46:25.3	-16:50:38	1500 (2)	CA93	...	I95
CB 54	LBN 1042	07020-1618	07:02:07.2	-16:18:58	1100 (5)	CA93	J00a	I95
CB 58	...	07161-2336	07:16:08.3	-23:36:19	1500 (2)	CA93	J97d	S02
BHR 12	DC 253.3-1.6	08076-3556	08:07:41.4	-35:56:12	400 (2,6)	LS95	J00a	S02
BHR 36	DC 267.4-7.5	08242-5050	08:24:16.8	-50:50:49	400 (7,6)	LS95	J00a	S02
BHR 41	DC 267.7-7.4	08261-5100	08:26:11.5	-51:00:39	400 (7,6)	LS95	...	S02
BHR 55	DC 275.9+1.9	09449-5052	09:44:56.9	-50:52:07	300 (7,6)	LS95	...	S02
BHR 58	DC 289.3-2.8	10471-6206	10:47:07.2	-62:06:28	250 (7,6)	LS95	...	S02
BHR 71	DC 297.7-2.8	11590-6452	11:59:03.3	-64:52:17	200 (8,6)	LS95	...	S95
BHR 86	DC 303.8-14.2	13036-7644	13:03:38.9	-76:44:11	180 (9,6)	LS95	...	S02
BHR 87	DC 307.3+2.9	13224-5928	13:22:26.0	-59:28:11	400 (7)	LS95	...	S02
CB 68	L 146	16544-1604	16:54:27.6	-16:04:48	160 (2)	CA94	J98b,d	I94/95
BHR 137	DC 344.6-4.3	17181-4405	17:18:08.9	-44:06:02	700 (7,6)	LS95	...	S02
CB 130	L 507	...	18:13:40.0	-02:34:00	200 (2)	CA02	J01a	I97
CB 188	...	19179+1129	19:17:53.9	+11:29:54	300 (2)	CA02	J97b/03c	I95
CB 199	B 335, L 663	19345+0727	19:34:35.3	+07:27:24	100 (10)	...	J07e/98b,d/01a	...
CB 205	L 810	19433+2743	19:43:22.1	+27:43:39	2000 (2)	CA93	J97e/03c	I95
CB 224	L 1100	20355+6343	20:35:30.1	+63:42:58	400 (5)	CA93	J03a,b	I94
CB 230	L 1177	21169+6804	21:16:52.7	+68:05:09	400 (5)	CA93	J97b/01a	I94
CB 232	B 158	21352+4307	21:35:14.2	+43:07:04	600 (2)	CA93	J98b/00b	I95/97
CB 240	L 1192	22317+5816	22:31:44.1	+58:16:21	500 (2)	CA93	J97e/00b	I95
CB 243	L 1246	23228+6320	23:22:54.2	+63:19:54	700 (2)	CA93	J97b,c/98c	I94/95
CB 244	L 1262	23238+7401	23:23:40.0	+74:01:30	200 (12)	CA93	J97b,c/98b/01a,b	I95
CB 246	L 1253	...	23:54:05.0	+58:18:00	140 (2)	CA93	J00b,c/01a	I96/97

<sup>a</sup> L= Lynds (1962); LBN= Lynds (1965); B= Barnard et al. (1927); BHR= Clemens & Barvainis (1988)

<sup>b</sup> Reference position for all Figures; not always identical to IRAS PSC position

<sup>c</sup> Near-IR observing details, see Table 4. (Sub)mm observing details, see Table 3.

References. — (1) this paper (Sect. 5), (2) Launhardt & Henning (1997), (3) Launhardt & Sargent (2001), (4) Testi et al. (1997), (5) Wolf et al. (2003), (6) Henning & Launhardt (1998), (7) Bourke et al. (1995b), (8) Bourke et al. (1997), (9) Whittet et al. (1997), (10) Olofsson & Olofsson (2009), (11) Dickman & Clemens (1983), (12) Hilton & Lahulla (1995)

TABLE 3  
SUBMILLIMETRE AND MILLIMETRE CONTINUUM OBSERVING PARAMETERS

Obs. code	Telescope	Date	Detector	$\lambda_0$ [mm]	HPBW [arcsec]	$\tau_{\text{Zenith}}$	Flux calibrators <sup>a</sup>
J97a	JCMT 15m	06/97	SCUBA	0.45 / 0.85	8.6 / 14.9 <sup>d</sup>	0.062 ± 0.007 <sup>b</sup>	Ur
J97b	JCMT 15m	08/97	SCUBA	0.45 / 0.85	8.5 / 14.8	0.09 ± 0.03 <sup>b</sup>	Ur, Ma
J97c	JCMT 15m	09/97	SCUBA	0.45 / 0.85	9.5 / 15.1	0.105 ± 0.008 <sup>b</sup>	Ur
J97d	JCMT 15m	10/97	SCUBA	0.45 / 0.85	8.6 / 14.9 <sup>d</sup>	0.17 ± 0.03 <sup>b</sup>	Ur, 618
J97e	JCMT 15m	12/97	SCUBA	0.45 / 0.85	8.6 / 14.9 <sup>d</sup>	0.042 ± 0.006 <sup>b</sup>	HL, 10216
J98a	JCMT 15m	02/98	SCUBA	0.45 / 0.85	8.6 / 14.9 <sup>d</sup>	0.052 ± 0.005 <sup>b</sup>	10216, 16293
J98b	JCMT 15m	04/98	SCUBA	0.45 / 0.85	8.2 / 14.6	0.06 ± 0.04 <sup>b</sup>	Ur, 10216, 2668, 618
J98c	JCMT 15m	07/98	SCUBA	0.45 / 0.85	8.0 / 14.4	0.032 ± 0.004 <sup>b</sup>	Ur
J98d	JCMT 15m	08/98	SCUBA	0.45 / 0.85	8.0 / 14.4	0.096 ± 0.006 <sup>b</sup>	Ur, 16293
J00a	JCMT 15m	03/00	SCUBA	0.45 / 0.85	8.6 / 14.9 <sup>d</sup>	0.28 ± 0.05 <sup>b</sup>	10216, 618, 16293
J00b	JCMT 15m	06/00	SCUBA	0.45 / 0.85	8.3 / 14.8	0.107 ± 0.004 <sup>b</sup>	Ur, 16293
J00c	JCMT 15m	09/00	SCUBA	0.45 / 0.85	8.6 / 14.9 <sup>d</sup>	0.088 ± 0.008 <sup>b</sup>	618
J01a	JCMT 15m	09/01	SCUBA	0.45 / 0.85	8.5 / 14.9	0.079 ± 0.009 <sup>b</sup>	Ur, 618
J01b	JCMT 15m	10/01	SCUBA	0.45 / 0.85	8.6 / 14.9 <sup>d</sup>	0.056 ± 0.005 <sup>b</sup>	Ma, 2668
J03a	JCMT 15m	02/03	SCUBA <sup>c</sup>	0.45 / 0.85	9.3 / 15.8	0.042 ± 0.001 <sup>b</sup>	Ur
J03b	JCMT 15m	05/03	SCUBA <sup>c</sup>	0.45 / 0.85	8.6 / 14.9 <sup>d</sup>	0.037 ± 0.001 <sup>b</sup>	Ur
J03c	JCMT 15m	09/03	SCUBA	0.45 / 0.85	9.3 / 15.8	0.080 ± 0.005 <sup>b</sup>	Ur
I94	IRAM 30m	04/94	MPIfR 7-chan.	1.3	10.5	0.26 ± 0.12	Ur, Ma
I95	IRAM 30m	02/95	MPIfR 7-chan.	1.3	10.5	0.23 ± 0.11	Ur, Ma
I96	IRAM 30m	02/96	MPIfR 19-chan.	1.3	10.5	0.20 ± 0.10	Ur
I97	IRAM 30m	03/97	MPIfR 19-chan.	1.3	10.5	0.22 ± 0.12	Ur
S95	SEST 15m	11/95	MPIfR 1-chan.	1.3	23	0.19 ± 0.06	Ur
S02	SEST 15m	11/02	SIMBA	1.3	24	0.20 ± 0.05	Ur, Np

<sup>a</sup>Planets and standard calibration sources. Ur=Uranus, Ma=Mars, Np=Neptune, 618=CRL 618, HL=HL Tau, 10216=IRC+10216, 16293=IRAS 16293-2422, 2668=CRL 2668

<sup>b</sup>Zenith optical depth at 225 GHz, monitored by the Caltech Submillimeter Observatory radiometer. See Sect. A for 450- and 850- $\mu$ m conversions

<sup>c</sup>SCUBA operated in scan-map mode

<sup>d</sup>Planet beam map not available. Quoted beam-sizes are an average

TABLE 4  
NIR OBSERVING PARAMETERS

Obs. code	Telescope	Date	Camera	Pixel scale	Filters <sup>a</sup>	Seeing
CA93	Calar Alto 3.5m	12/93	MAGIC	0''.32	J, H, KS	0''.9 – 2''.2
CA94	Calar Alto 3.5m	08/94	MAGIC	0''.32	KS	1''.4
CA95	Calar Alto 3.5m	01/95	MAGIC	0''.32	KS	0''.5 – 1''.0
CA02	Calar Alto 3.5m	10/02	$\Omega$ Prime	0''.40	J, H, KS	1''.4
LS95	La Silla 2.2m	03/95	IRAC-2B	0''.50	J, H, KP	1''.1 – 1''.4

<sup>a</sup> $\lambda_0 / \Delta\lambda$  in  $\mu$ m: J: 1.25/0.30; H: 1.65/0.30; KS: 2.16/0.32; KP: 2.10/0.34



TABLE 5  
RESULTS OF THE MILLIMETRE AND SUBMILLIMETRE CONTINUUM MAPPING

Name	Peak position <sup>a</sup> (B1950) [h:m:s, °:':"]	450 $\mu$ m		850 $\mu$ m		1.3 mm		Fig.
		$I_{\nu}^{\text{peak}}$ ( $\Omega_b$ ) [Jy/beam]	$S_{\nu}^{\text{totb}}$ [Jy]	$I_{\nu}^{\text{peak}}$ ( $\Omega_b$ ) [Jy/beam]	$S_{\nu}^{\text{totb}}$ [Jy]	$I_{\nu}^{\text{peak}}$ ( $\Omega_b$ ) [Jy/beam]	$S_{\nu}^{\text{totb}}$ [Jy]	
CB 4	...	...	...	...	...	<0.013 <sup>c</sup> (10.5)	...	...
CB 6N	...	...	...	...	...	<0.014 <sup>c</sup> (10.5)	...	...
CB 17SW	...	...	...	...	...	<0.022 <sup>c</sup> (10.5)	...	...
CB 39	...	...	...	...	...	<0.027 <sup>c</sup> (10.5)	...	...
CB 52	...	...	...	...	...	<0.023 <sup>c</sup> (10.5)	...	...
BHR 41	...	...	...	...	...	<0.060 <sup>c</sup> (24)	...	...
CB 6	00:46:33.8, +50:28:25	1.0 (10)	8.0	0.18 (14.9)	0.8	0.058 (10.5)	0.18	1
CB 17	...	...	...	...	1.3	...	0.55	2
SMM1	04:00:33.6, +56:47:52	<1.2 <sup>c</sup> (8.0)	...	0.17 (15)	...	0.039 (10.5)	...	2
SMM2	04:00:31.5, +56:47:58	<1.2 <sup>c</sup> (8.0)	...	0.13 (15)	...	0.029 (10.5)	...	2
CB 26	04:55:54.6, +52:00:15	3.2 (8.6)	6.7	0.48 (14.9)	0.6	0.16 (10.5)	0.24	3
CB 34	...	...	40	...	5.5	...	2.0	4
SMM1	05:44:06.4, +20:59:38	1.2 (8.6)	10	0.44 (14.9)	1.5	0.090 (10.5)	0.70	4
SMM2	05:44:02.5, +20:59:05	1.0 (8.6)	5	0.29 (14.9)	0.7	0.071 (10.5)	0.40	4
SMM3	05:43:59.9, +20:59:31	0.5 (8.6)	2	0.13 (14.9)	0.2	0.045 (10.5)	0.30	4
CB 54	07:02:06.0, -16:18:51	9.3 (8.6)	74.0	1.5 (14.9)	7.3	0.34 (10.5)	2.05	5
CB 58	07:16:09.4, -23:35:52	...	...	<0.27 <sup>c</sup> (14.9)	...	0.12 (10.5)	0.48	6
BHR 12	...	...	27.5	...	6.9	0.67 (24)	1.54	7
SMM1	08:07:40.3, -35:56:05 <sup>d</sup>	3.0 (8.6)	5.9	1.2 (14.9)	1.7	... <sup>e</sup>	0.49 <sup>e</sup>	7
SMM2	08:07:40.0, -35:56:26 <sup>d</sup>	3.7 (8.6)	6.2	1.0 (14.9)	1.2	... <sup>e</sup>	0.36 <sup>e</sup>	7
BHR 36	08:24:15.8, -50:50:44	...	...	1.2 (16)	5.0	0.28 (24)	0.85	8
BHR 55	09:44:57.2, -50:52:11	...	...	...	...	0.19 (24)	0.42	9
BHR 58	10:47:01.0, -62:06:50	...	...	...	...	0.13 (24)	0.12	...
BHR 71	11:59:03.0, -64:51:58	...	...	...	...	1.83 (23)	3.80	10
BHR 86	13:03:41.6, -76:44:23	...	...	...	...	0.26 (24)	1.33	11
BHR 87	13:22:24.5, -59:27:57	...	...	...	...	0.11 (24)	1.00	...
CB 68	16:54:27.2, -16:04:44	2.5 (8.6)	21.0	0.53 (14.6)	4.0	0.15 (10.5)	1.55	12
BHR 137	17:18:08.5, -44:06:17	...	...	...	...	0.38 (24)	1.25	13
CB 130	...	...	12	...	2.2	...	1.20	14
SMM1	18:13:39.6, -02:33:44	1.1 (8.6)	3.0	0.27 (14.9)	0.8	0.051 (10.5)	0.36	14
SMM2	18:13:37.6, -02:33:46	0.8 (8.6)	1.5	0.14 (14.9)	0.3	0.033 (10.5)	0.12	14
CB 188	...	...	8.4	...	1.6	...	0.30	15
SMM1	19:17:54.1, +11:30:02	1.0 (9.3)	2.0	0.21 (15.8)	0.3	0.062 (10.5)	0.10	15
CB 199	19:34:35.3, +07:27:24 <sup>d</sup>	4.2 (8.6)	15.1	1.1 (14.9)	4.0	...	...	16
CB 205	...	...	21.4	...	3.5	...	0.85	17
SMM1	19:43:22.1, +27:43:44	2.4 (9.3)	...	0.48 (15.8)	...	0.078 (10.5)	...	17
SMM2	19:43:19.2, +27:43:19	1.3 (9.3)	...	0.30 (15.8)	...	0.044 (10.5)	...	17
CB 224	...	...	6.0	...	0.8	...	0.30	18
SMM1	20:35:30.6, +63:42:47	1.2 (9.3)	5.7	0.27 (15.8)	0.7	0.067 (10.5)	0.24	18
SMM2	20:35:34.6, +63:43:10	0.4 (9.3)	0.4	0.14 (15.8)	0.1	0.040 (10.5)	0.06	18
CB 230	21:16:53.7, +68:04:55	3.9 (8.6)	16.5	0.92 (14.9)	2.9	0.23 (10.5)	0.88	19
CB 232	...	...	27	...	2.4	...	0.45	20
SMM	21:35:13.3, +43:07:13	1.9 (12)	3.5	0.32 (14.9)	0.9	0.070 (10.5)	0.20	20
IRS1	21:35:14.5, +43:07:07	1.6 (12)	3.3	...	0.3	...	0.08	20
CB 240	22:31:45.9, +58:16:18	<0.5 <sup>c</sup> (8.6)	...	0.14 (14.9)	2.4	0.028 (10.5)	0.39	21
CB 243	...	...	...	...	2.0	...	0.68	22
SMM1	23:22:52.1, +63:20:13	1.6 (8.6)	6.0	0.37 (14.9)	1.2	0.083 (11)	0.38	22
SMM2	23:23:03.4, +63:20:20	<0.5 <sup>c</sup> (8.6)	...	0.15 (14.9)	0.5	0.031 (11)	0.19	22

TABLE 5—*Continued*

Name	Peak position <sup>a</sup> (B1950) [h : m : s, ° : ' : " ]	450 $\mu$ m		850 $\mu$ m		1.3 mm		Fig.
		$I_V^{\text{peak}}$ ( $\Omega_b$ ) [Jy/beam]	$S_V^{\text{totb}}$ [Jy]	$I_V^{\text{peak}}$ ( $\Omega_b$ ) [Jy/beam]	$S_V^{\text{totb}}$ [Jy]	$I_V^{\text{peak}}$ ( $\Omega_b$ ) [Jy/beam]	$S_V^{\text{totb}}$ [Jy]	
CB 244	...	...	...	...	5.1	...	2.0	23
SMM1	23:23:48.5, +74:01:08	1.8 (8.6)	13.0	0.43 (14.9)	1.6	0.11 (10.5)	0.8	23
SMM2	23:23:29.5, +74:01:54	<1.3 <sup>c</sup> (8.6)	...	0.32 (14.9)	3.5	0.06 (10.5)	1.2	23
CB 246	...	...	30	...	3.1	...	2.56	24
SMM1	23:54:11.0, +58:17:15	1.3 (15)	22	0.12 (16)	1.8	0.039 (15)	0.59	24
SMM2	23:54:03.7, +58:18:36	1.6 (15)	8	0.11 (16)	1.3	0.041 (15)	0.58	24

<sup>a</sup>Derived from gaussian fit to the component in the 1.3 mm map (if not stated otherwise).

<sup>b</sup>Flux density measured in a polygon enclosing the  $2\sigma$  contour.

<sup>c</sup> $3\sigma$  detection limit; source not detected.

<sup>d</sup>Source position derived from the 850  $\mu$ m SCUBA map.

<sup>e</sup>The two sub-cores are not resolved in the 1.3 mm map.

TABLE 6  
GLOBULE MORPHOLOGY AND MULTIPLICITY

Name	Size <sup>a</sup> – ['] [pc]		Aspect Ratio	$A_V^b$ [mag]	Globule Morphology <sup>c</sup>	Multiplicity of embedded sources	Projected separations [AU]
CB 6	5.5	0.96	2.6	0.3	I, T, N	Unresolved	...
CB 17	2.2	0.16	1.0	0.4	I, T	Two mm cores and IRS	2,000 – 5,000
CB 26	4.8	0.20	2.0	1.5	CG, C, BR	Unresolved <sup>d</sup>	...
CB 34	3.1	1.35	2.0	1.0	I, N	Three mm cores and NIR star clusters	6,000 – 80,000
CB 54	4.4	1.40	1.6	0.5	I, N	Unresolved mm core and NIR star cluster	10,000
CB 58	5.1	2.22	2.3	1.0	CG, BR	Two mm cores and NIR star cluster	7,500 - 50,000
BHR 12	2.4	0.28	1.5	1.2	CG, BR, N	Two mm cores	8,000
BHR 36	3.5	0.41	1.3	1.5	CG, BR, N	Unresolved	...
BHR 55	3.5	0.30	1.3	1.2	I, C	Unresolved	...
BHR 71	4.9	0.25	2.7	3.4	I	Unresolved mm core, two IRS	3,400
BHR 86	7.7	0.43	1.7	1.3	CG, BR	Unresolved	...
CB 68	3.9	0.18	1.3	1.2	I, T	Unresolved	...
BHR 137	3.9	0.79	1.7	2.0	I, N, T	Unresolved mm core and IRS	2,000 – 15,000
CB 130	3.5	0.20	2.5	3.7	I	Two mm cores and IRS	3,000 – 6,000
CB 188	1.6	0.14	2.0	3.4	I	Unresolved	...
CB 199	5.0	0.14	1.2	0.6	I	Unresolved	...
CB 205	8.2	4.76	1.5	1.5	I, N	Two mm cores and NIR star cluster	4,000 – 60,000
CB 224	3.4	0.39	1.0	1.3	I	Two mm cores	14,000
CB 230	2.7	0.31	1.5	1.5	I, BR, N	Unresolved mm core, two IRS	4,000
CB 232	3.5	0.61	2.5	1.7	CG	MM core and IRS	7,000
CB 240	2.7	0.39	1.5	2.4	I	MM core and NIR star cluster	1,200 – 10,000
CB 243	4.7	0.96	4.6	2.0	F, T	Two mm cores and IRS	7,000 – 50,000
CB 244	7.9	0.46	2.0	2.0	I	Two mm cores	18,000
CB 246	5.9	0.24	1.7	2.7	I, T	Two mm cores	13,000

<sup>a</sup>Characteristic or mean angular size ( $\sqrt{ab}$ ), derived from the optical globule sizes listed by Clemens & Barvainis (1988) for CB (northern) globules and in Bourke et al. (1995b) for BHR (southern) globules. Mean linear size derived by using the distances listed in Table 2. At the globule centres, the extinction is likely to be higher than this.

<sup>c</sup>Globule morphology, based on visual inspection of DSS2-red optical images: (I) isolated; (CG) cometary globule; (F) filamentary; (C) complex, multiple cores; (BR) bright rim; (N) nebula associated; (T) tail.

<sup>d</sup>CB 26: contains possible a 20 AU binary with a circumbinary disk (Launhardt et al. 2009).

TABLE 7  
PHYSICAL PARAMETERS OF SELECTED SOURCES

Name	$L_{\text{bol}}$ [ $L_{\odot}$ ]	$\frac{L_{\text{dust}}}{L_{\text{bol}}}$ [%]	$T_{\text{bol}}$ [K]	$\alpha_{\text{IR}}^a$	$T_d^b$ [K]	$M_H^c$ [ $M_{\odot}$ ]	$n_H^d$ [ $\text{cm}^{-3}$ ]	$N_H^e$ [ $\text{cm}^{-2}$ ]	Size <sup>f</sup> [AU]	Evol. stage	Remark
CB 6	6.4	2.9	178	+0.6	20	1.0/1.8	>3E7/3E4	1.1E23	<3,000/36,000	Class I	NIR nebula, MIR source, outflow
CB 17 - SMM1+2	0.07	>30	15	...	10	4.0	6E6	2.0E23	8,000	pre-stellar	No IR counterpart, 8 $\mu\text{m}$ shadow
CB 17 - IRS	0.6	<2.6	>55	+0.8	20	...	...	...	...	Class I	NIR nebula, MIR source, low-velocity outflow?
CB 26	0.25	2.5	137	-0.1	20	0.1/0.1	>2E8/1E5	2.9E23	<700/7,500	Class I	NIR nebula, edge-on disk, outflow
BHR 12 - SMM1	11	1.6	126	+1.1	20	0.7	6E7	2.6E23	2,000	Class I	NIR source and jet, outflow
BHR 12 - SMM2	1.9	5.3	50	+0.1	15	0.8	7E7	3.4E23	2,000	Class 0	No NIR counterpart, MIR source, outflow
BHR 36	16	2.4	149	+0.9	20	5.9	4E6	9.8E22	10,000	Class I	NIR jet, MIR source, outflow
BHR 55	2.2	4.4	39	+1.1	15	2.4	6E7	9.8E22	<3,000	Class 0	No NIR counterpart, MIR source, no outflow data
BHR 71 <sup>g</sup>	10	3.4	53	+1.7	15	9.7	1E8	1.0E24	3,600	Class 0	No NIR counterpart, 2 MIR sources, 2 outflows
BHR 86	1.5	6.2	61	+1.4	15	3.4	2E6	1.3E23	10,000	Class 0	No NIR counterpart, MIR source, outflow
CB 68	1.3	3.9	50	+2.4	15	0.6/1.9	5E7/1E6	4.1E23	2,000/10,000	Class 0	No NIR counterpart, MIR source, outflow
BHR 137	...	...	...	...	20	26	5E6	1.3E23	16,000	...	No NIR or IRAS counterpart, no <i>Spitzer</i> data
CB 130 - SMM1	0.15	11	55	+1.0	15	0.9/1.8	5E6/2E5	1.4E23	5,000/20,000	Class 0	NIR nebula, MIR source, no outflow data
CB 130 - SMM2	...	...	...	...	10/15	0.6/1.8	3E7/2E5	1.7E23	2,400/20,000	pre-stellar	No IR counterpart, no outflow data
CB 130 - IRS	$\geq 0.04$	...	...	-0.7	20	...	...	...	...	Class I	Red star with nebulosity, outside mm core
CB 188	1.5	1.3	307	+0.2	20	0.3/1.0	>4E7/8E4	1.1E23	<1500/20,000	Class I	Red star, outflow
CB 199	0.5	4.8	37	+1.6	15	0.6	1E8	3.7E23	1500	Class 0	No NIR counterpart, MIR source, outflow
CB 224 - SMM1	6.6	2.2	56	+1.8	15	2.4	4E7	1.8E23	3600	Class 0	Very faint NIR nebula, no <i>Spitzer</i> data, outflow
CB 224 - SMM2	2.4	0.8	337	+0.2	20	0.4	>4E7	7.7E22	<2000	Class I	Red star, disk, no outflow detected
CB 230 - IRS 1 <sup>g</sup>	9	3.5	214	-0.3	20	6.1	7E7	4.2E23	4000	Class I	NIR nebula, MIR source, outflow
CB 230 - IRS 2 <sup>g</sup>	$\geq 0.1$	...	...	-0.7	20	...	...	...	...	Class I	NIR nebula, MIR source, outflow
CB 232 - SMM	...	...	...	...	10	9	2E7	3.5E23	7000	pre-stellar	No IR counterpart, close proximity to IRS
CB 232 - IRS 1	13	1.0	166	+1.7	20	1.0	...	...	...	Class I	Red star, outflow, close proximity to SMM1
CB 243 - SMM1	<7.2 <sup>h</sup>	4.1 <sup>h</sup>	123 <sup>h</sup>	...	10	22	2E7	4.0E23	10,000	pre-stellar	No IR counterpart, close proximity to IRS
CB 243 - IRS	<7.2 <sup>h</sup>	4.1 <sup>h</sup>	123 <sup>h</sup>	+0.8	20	...	...	...	...	Class I	Red star, outflow, close proximity to SMM1
CB 243 - SMM2	...	...	...	...	10	11	2E6	1.4E23	15,000	pre-stellar	No IR source, 8 $\mu\text{m}$ shadow
CB 244 - SMM1	1.3	4.0	69	+2.4	15	3.1	7E7	3.0E23	2,700	Class 0	NIR nebula, MIR source, outflow
CB 244 - SMM2	...	...	...	...	10	5.7	8E6	3.0E23	8,000	pre-stellar	No IR counterpart, 8 $\mu\text{m}$ shadow
CB 246 - SMM1	...	...	...	...	10	1.4	8E6	1.0E23	5,000	pre-stellar	No IR counterpart, 8 $\mu\text{m}$ shadow
CB 246 - SMM2	...	...	...	...	10	1.4	2E6	1.0E23	7,500	pre-stellar	No IR counterpart, 8 $\mu\text{m}$ shadow

<sup>a</sup>NIR spectral index  $\alpha_{\text{IR}} = -\frac{d \log(F_{\nu})}{d \log(\nu)}$  (Adams et al. 1987) and  $\lambda_1 = 2.2 \mu\text{m}$ ,  $\lambda_2 = 24 \mu\text{m}$ , except for BHR 12-SMM2, BHR 55, BHR 71, BHR 86, CB 68, CB 199 ( $\lambda_1 = 3.6 \mu\text{m}$ ), CB 230-IRS2 ( $\lambda_2 = 5.8 \mu\text{m}$ ), and CB 224-SMM1 ( $\lambda_2 = 60 \mu\text{m}$ ).

<sup>b</sup>Assumed mass-averaged dust temperature  $T_d$  (see Sect. 3.6).

<sup>c</sup> $M_H$  computed from integrated 1.3 mm flux (Table 5), assuming  $\kappa_{\text{dust}}(1.3 \text{ mm}) = 0.5 \text{ g cm}^{-3}$ , H-to-dust mass ratio 110, and mass-averaged dust temperature from col. 6 (see Sect. 3.6). If two values are given, the first one refers to the core, the second one to the envelope only. For CB 199, we used the 850  $\mu\text{m}$  flux with  $\kappa_{\text{dust}}(850 \mu\text{m}) = 1.1 \text{ g cm}^{-3}$ .

<sup>d</sup>Source-averaged number density,  $n_H$ , computed from  $M_H$  (col. 7) and FWHM size (col. 10) (see Sect. 3.6). If two values are given, the first one refers to the core, the second one to the envelope

only.

<sup>e</sup>Beam-averaged peak column density,  $N_H$ , computed from 1.3 mm peak flux densities and beam sizes listed in Table 5 (see Sect. 3.6).

<sup>f</sup>FWHM size (mean diameter of the 50% contour), deconvolved with the beam and projected at the distance listed in Table 3. If two values are given, the first one refers to the core only, the second one to the envelope.

<sup>g</sup>The dust cores in BHR 71 and CB 230 both have two embedded IR sources each, which are not resolved in the (sub)mm maps.

<sup>h</sup>Values refer to the combined SED and are not representative of the individual sources.

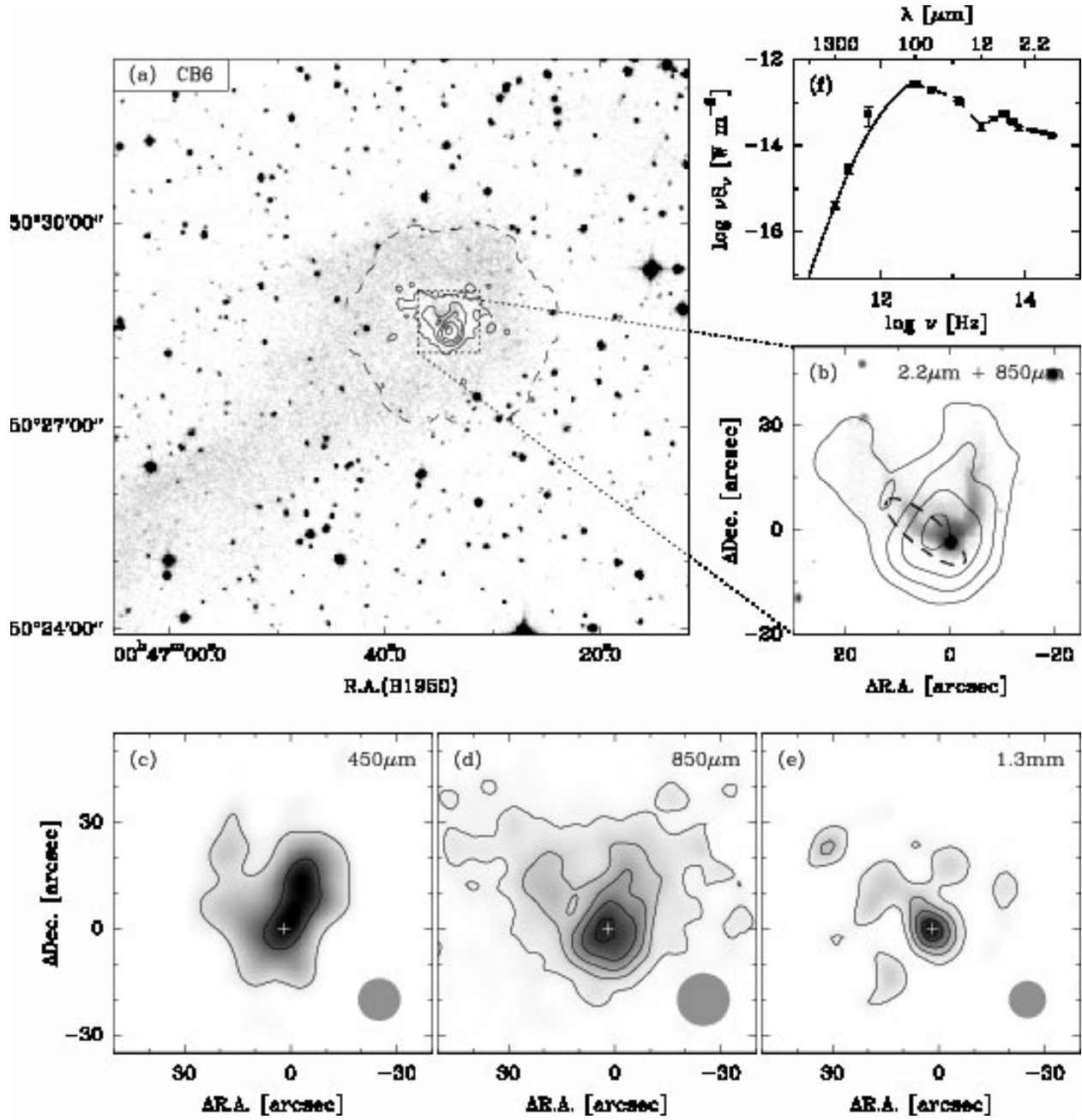


Fig. 1.— CB 6: a) Optical image (DSS2 red) with contours of the 850  $\mu\text{m}$  dust continuum emission overlaid. b) NIR K-band image with 850  $\mu\text{m}$  dust continuum contours. The IRAS PSC position is marked by a dashed ellipse. c) 450  $\mu\text{m}$  dust continuum emission; grey scale and contours at 1.1 and 1.5 Jy/beam. d) 850  $\mu\text{m}$  dust continuum emission; grey scale and contours at 35 to 175 by 35 mJy/beam. e) 1.3 mm dust continuum emission; grey scale and contours at 12 to 48 by 12 mJy/beam. Beam sizes are indicated as grey ellipses. The cross marks the position of the 1.3 mm peak. f) Spectral energy distribution showing the IRAM 1.3 mm, SCUBA 850 and 450  $\mu\text{m}$ , IRAS PSC, Spitzer MIPS and IRAC, and ground-based NIR data.

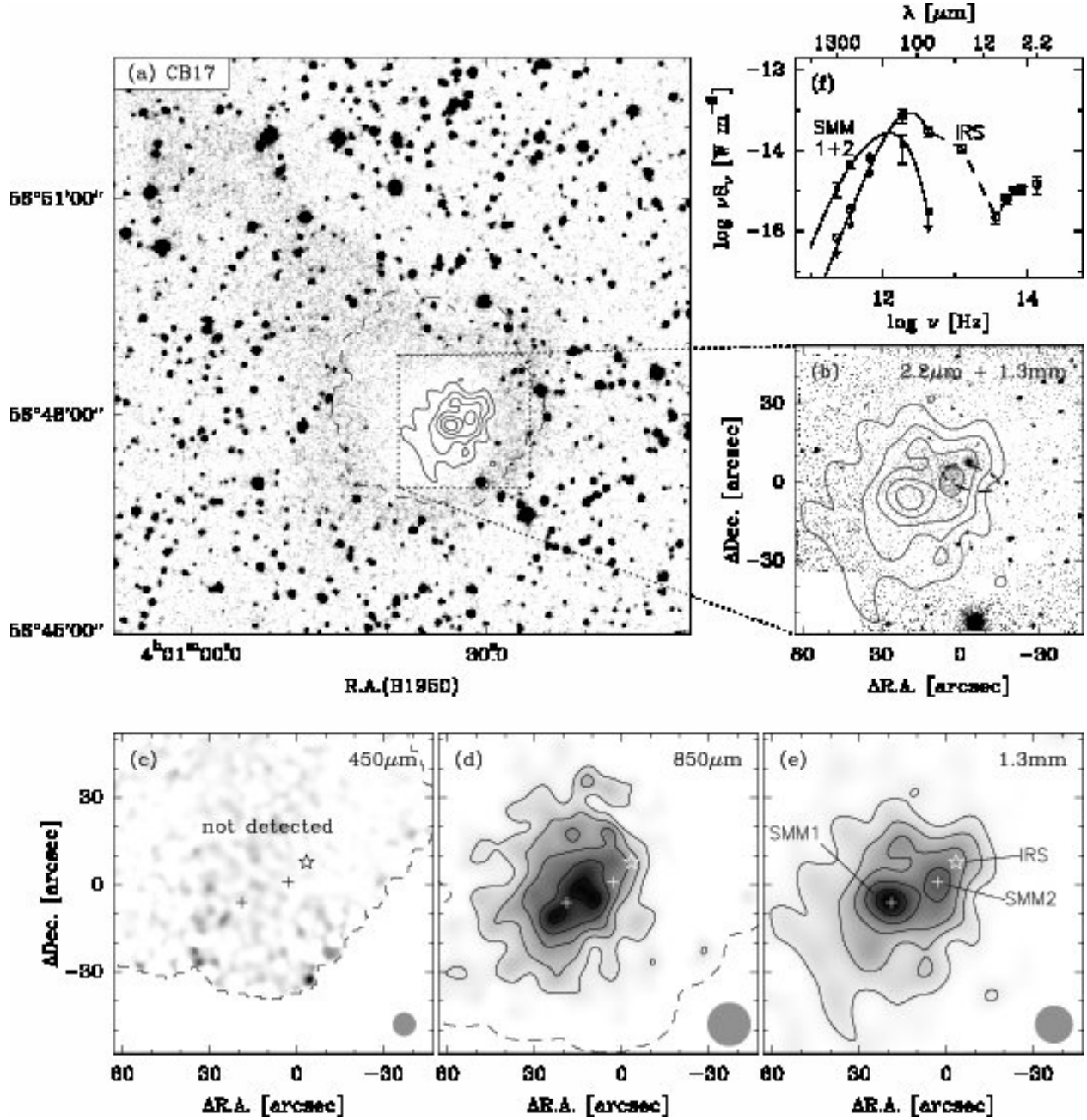


Fig. 2.— CB 17: a) Optical image (DSS2 red) with contours of the 1.3 mm dust continuum emission overlaid. b) NIR K-band image with 1.3 mm dust continuum contours. The IRAS PSC position is marked by a dashed ellipse. c) 450  $\mu\text{m}$  dust continuum map; the source is not detected at rms 400 mJy/beam. d) 850  $\mu\text{m}$  dust continuum emission; grey scale and contours at 50 to 170 by 30 mJy/beam. e) 1.3 mm dust continuum emission; grey scale and contours at 12 to 44 by 8 mJy/beam. Beam sizes are indicated as grey ellipses. Crosses mark the positions of SMM1 and SMM2 in the 1.3 mm map. The asterisk marks the position of the Spitzer source IRS. f) Spectral energy distributions of SMM(1+2) and IRS, showing the IRAM 1.3 mm, SCUBA 850  $\mu\text{m}$ , IRAS PSC, Spitzer MIPS and IRAC, and ground-based NIR data. Note that the 160  $\mu\text{m}$  data points result only from a coarse flux splitting (85% IRS and 15% SMM) since the two sources are not resolved in the MIPS3 map.

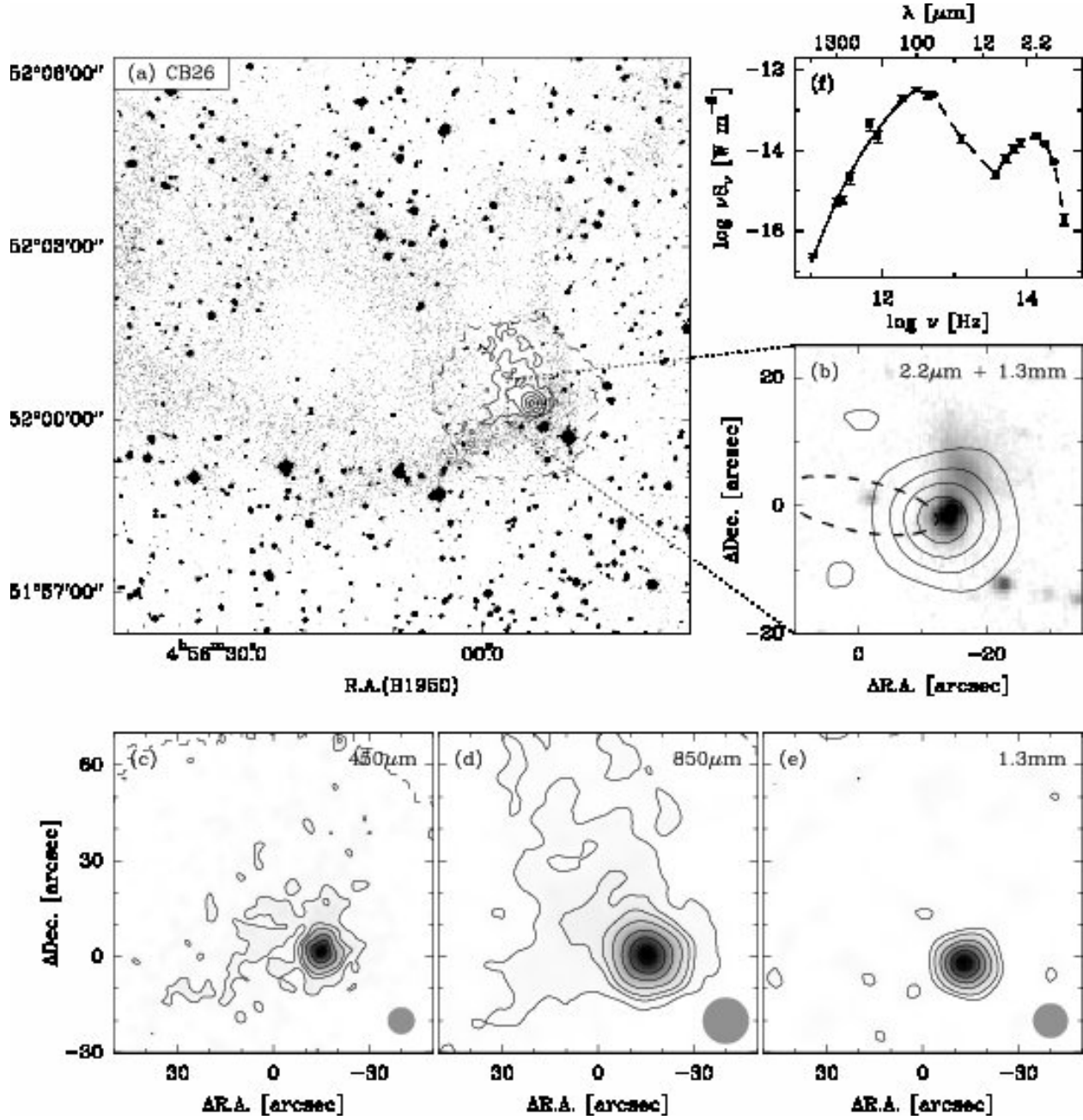


Fig. 3.— CB 26: a) Optical image (DSS2 red) with contours of the 850  $\mu\text{m}$  dust continuum emission overlaid. b) NIR K-band image with 1.3 mm dust continuum contours. The IRAS PSC position is marked by a dashed ellipse. c) 450  $\mu\text{m}$  dust continuum emission; grey scale and contours at 350, 700, 1050 to 3150 by 700 mJy/beam. d) 850  $\mu\text{m}$  dust continuum emission; grey scale and contours at 30, 60, 90, 150 to 400 by 100 mJy/beam. e) 1.3 mm dust continuum emission; grey scale and contours at 15, 30 to 150 by 30 mJy/beam. Beam sizes are indicated as grey ellipses. f) Spectral energy distributions, showing the OVRO 3 mm, IRAM 1.3 mm, SMA 1.1 mm, SCUBA 850 and 450  $\mu\text{m}$ , CSO 350  $\mu\text{m}$ , IRAS PSC, Spitzer MIPS and IRAC, and ground-based NIR data.

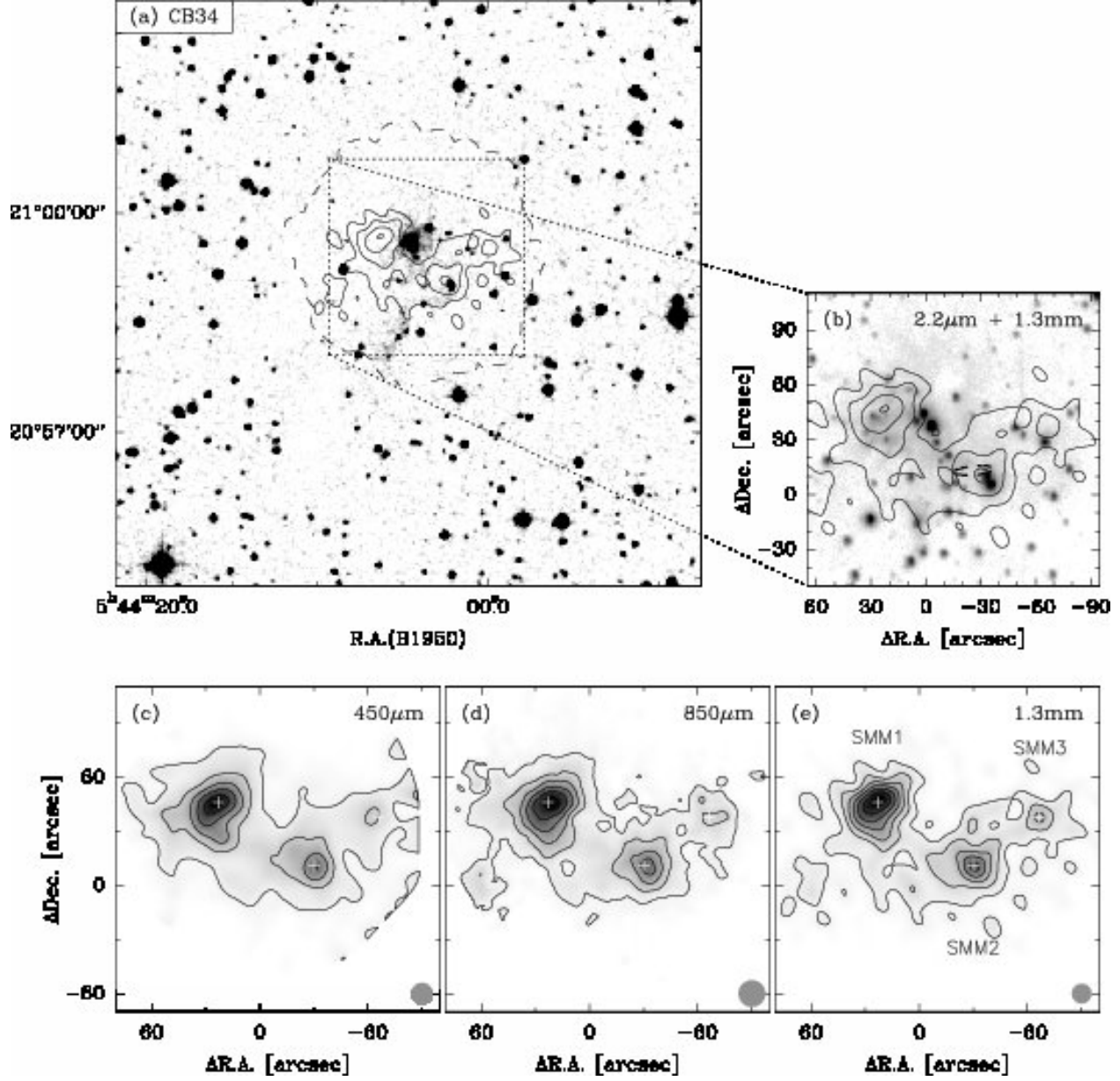


Fig. 4.— CB 34: a) Optical image (DSS2 red) with contours of the 1.3 mm dust continuum emission overlaid. b) NIR K-band image with 1.3 mm dust continuum contours. The IRAS PSC position is marked by a dashed ellipse. c) 450  $\mu\text{m}$  dust continuum emission; grey scale and contours at 500 to 1700 by 300 mJy/beam. d) 850  $\mu\text{m}$  dust continuum emission; grey scale and contours at 75 to 450 by 75 mJy/beam. e) 1.3 mm dust continuum emission; grey scale and contours at 18 to 108 by 15 mJy/beam. Beam sizes are indicated as grey ellipses. Crosses mark the positions of the three 1.3 mm peaks. No spectral energy distribution is shown since many different, partially unresolved sources contribute to the measured flux densities.



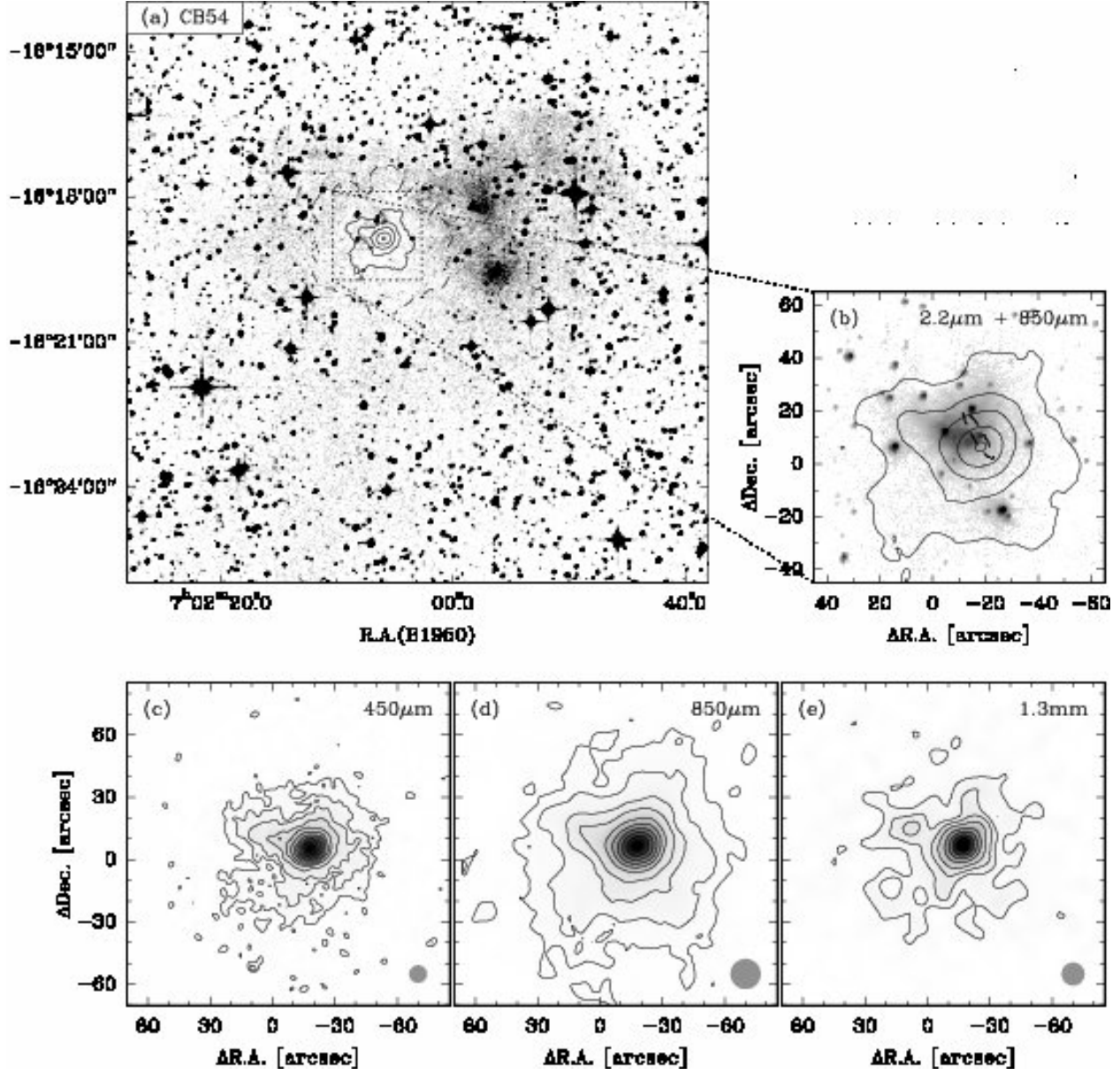


Fig. 5.— CB 54: a) Optical image (DSS2 red) with contours of the 850  $\mu\text{m}$  dust continuum emission overlaid. b) NIR K-band image with 850  $\mu\text{m}$  dust continuum contours. The IRAS PSC position is marked by a dashed ellipse. c) 450  $\mu\text{m}$  dust continuum emission; grey scale and contours at 0.4, 0.8, 1.2 to 9 0.8 Jy/beam. d) 850  $\mu\text{m}$  dust continuum emission; grey scale and contours at 50, 100, 200, 300, to 1500 by 200 mJy/beam. e) 1.3 mm dust continuum emission; grey scale and contours at 20, 40, 60, 90, 140, 190, 240, and 290 mJy/beam. Beam sizes are indicated as grey ellipses. No spectral energy distribution is shown since many different, partially unresolved sources contribute to the measured flux densities.

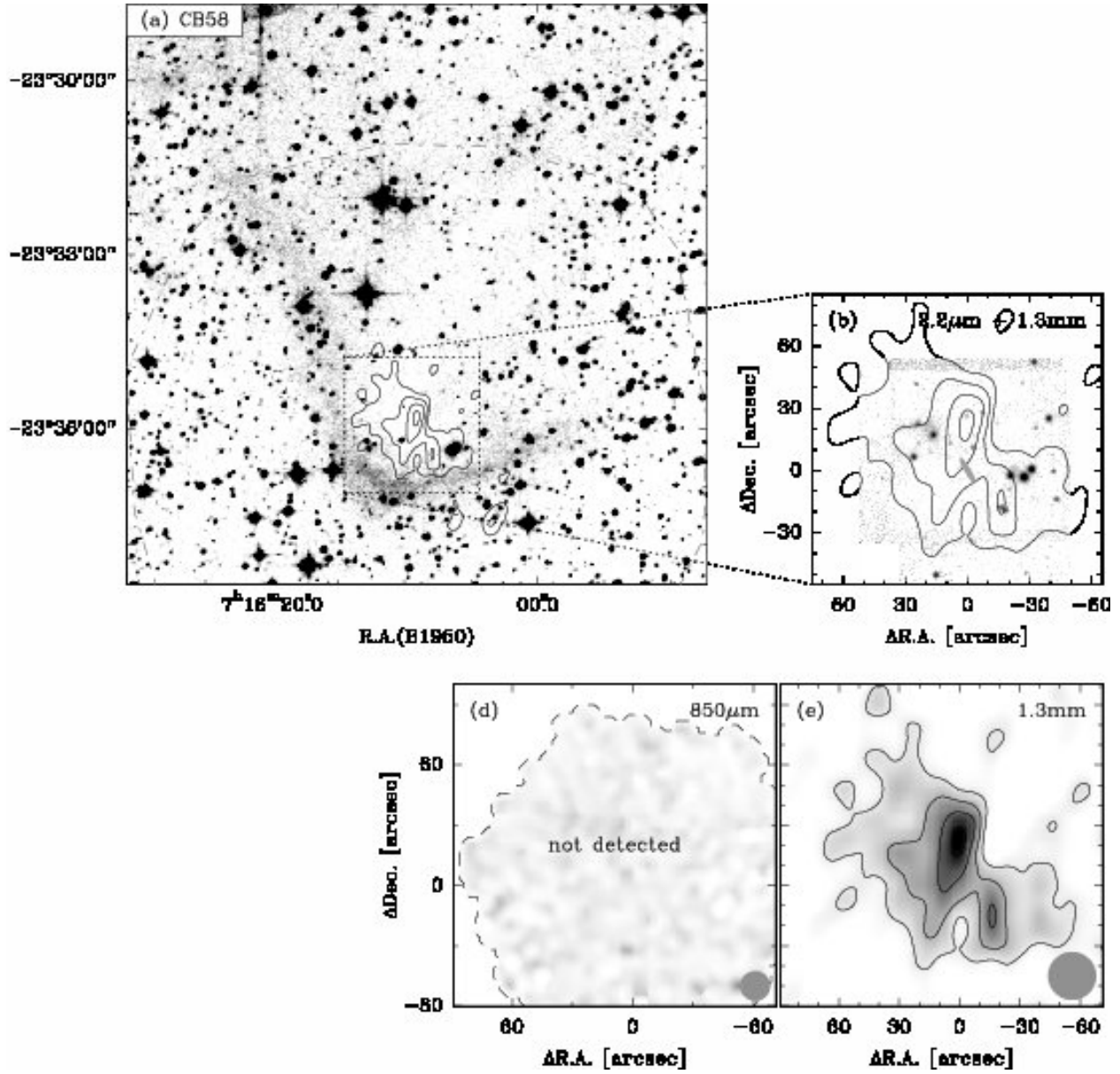


Fig. 6.— CB 58: a) Optical image (DSS2 red) with contours of the 1.3 mm dust continuum emission overlaid. b) NIR K-band image with 1.3 mm dust continuum contours. The IRAS PSC position is marked by a grey ellipse. d) 850  $\mu$ m dust continuum map; the source is not detected at rms 90 mJy/beam. e) 1.3 mm dust continuum emission; grey scale and contours at 33 to 132 by 33 mJy/beam. Beam sizes are indicated as grey ellipses. No spectral energy distribution is shown since many different, partially unresolved sources contribute to the measured flux densities.

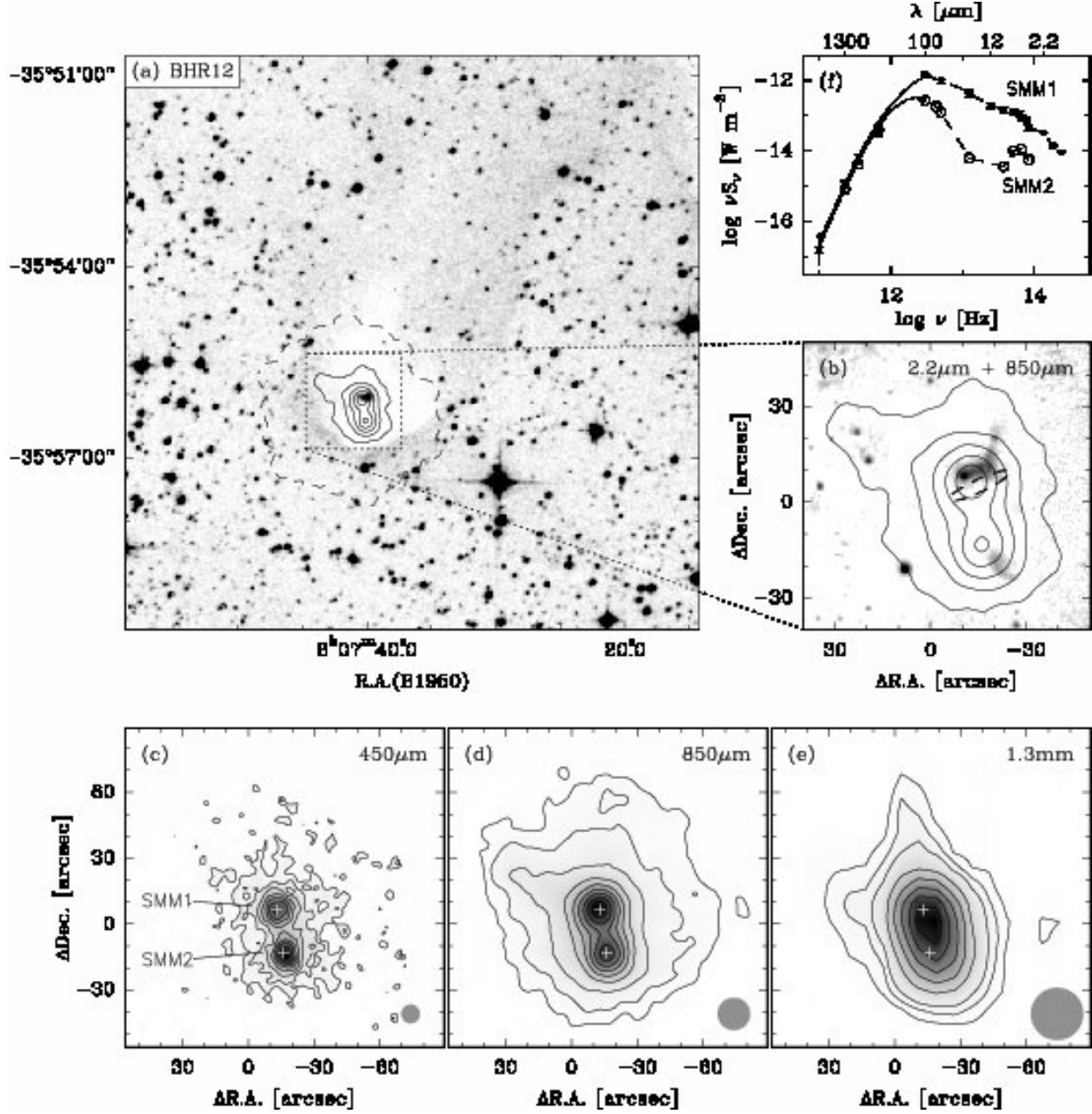


Fig. 7.— BHR 12: a) Optical image (DSS2 red) with contours of the 850  $\mu\text{m}$  dust continuum emission overlaid. b) NIR K-band image with 850  $\mu\text{m}$  dust continuum contours. The IRAS PSC position is marked by a dashed ellipse. c) 450  $\mu\text{m}$  dust continuum emission; grey scale and contours at 0.3, 0.6, 1 to 3.5 by 0.5 Jy/beam. d) 850  $\mu\text{m}$  dust continuum emission; grey scale and contours at 40, 100, 200 to 1200 by 150 mJy/beam. e) 1.3 mm dust continuum emission; grey scale and contours at 25, 60, 100 to 600 by 100 mJy/beam. Beam sizes are indicated as grey ellipses. Crosses mark the positions of the two 850  $\mu\text{m}$  peaks. f) Spectral energy distributions of SMM1 (filled squares) and SMM2 (empty circles) showing the ATCA 3 mm, SEST 1.3 mm, SCUBA 850 and 450  $\mu\text{m}$ , IRAS PSC, Spitzer MIPS and IRAC, and ground-based NIR data. The 1.3 mm fluxes (sources not resolved in the SEST map) are derived by fitting two Gaussian sources to the map.

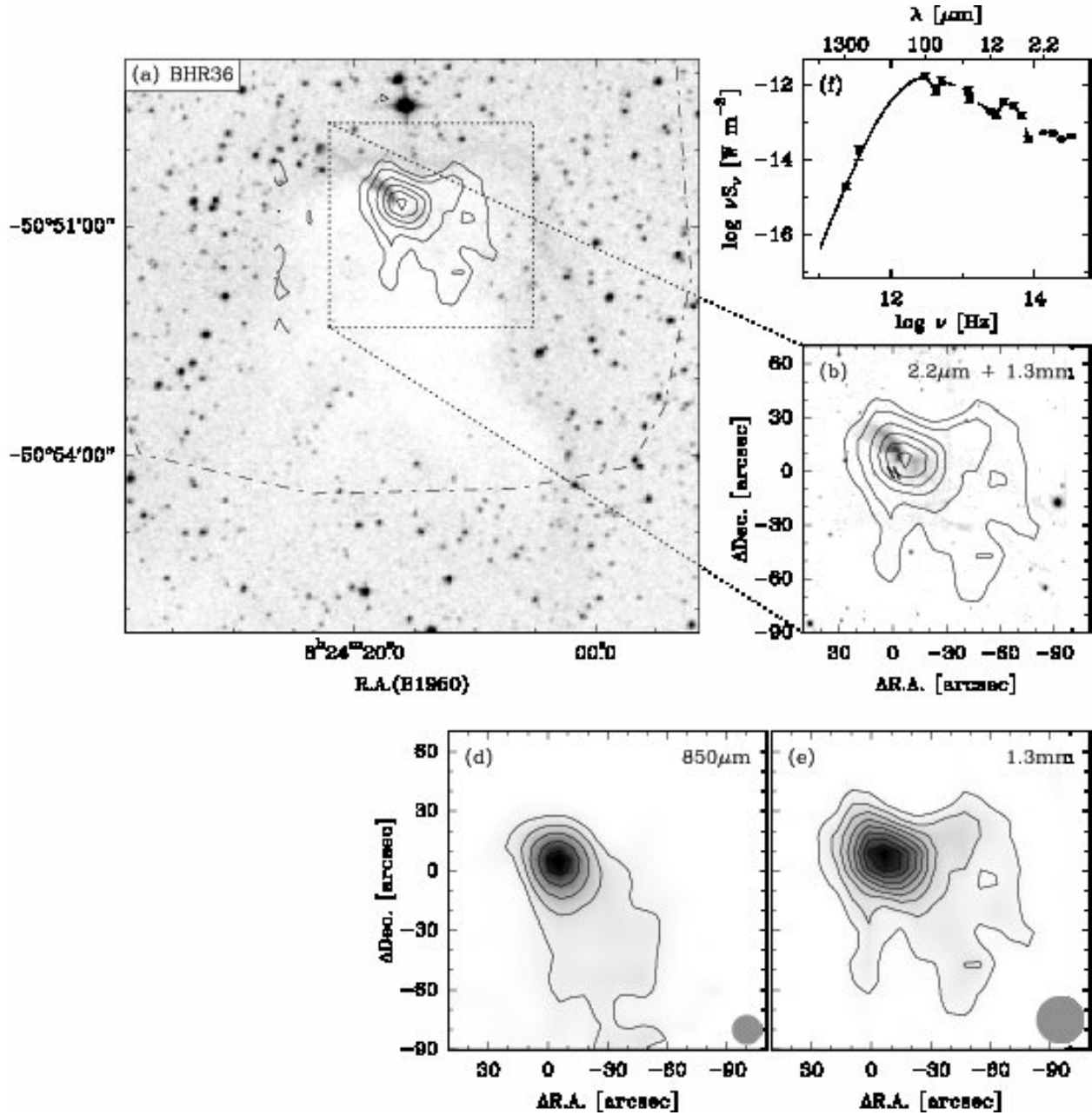


Fig. 8.— BHR 36: a) Optical image (DSS2 red) with contours of the 1.3 mm dust continuum emission overlaid. b) NIR K-band image with 1.3 mm dust continuum contours. The IRAS PSC position is marked by a dashed ellipse. d) 850  $\mu\text{m}$  dust continuum emission; grey scale and contours at 0.15, 0.3, 0.5, 0.75, and 1 Jy/beam. e) 1.3 mm dust continuum emission; grey scale and contours at 30 to 280 by 30 mJy/beam. Beam sizes are indicated as grey ellipses. f) Spectral energy distribution showing the SEST 1.3 mm, SCUBA 850  $\mu\text{m}$  IRAS PSC, Spitzer MIPS and IRAC, and ground-based NIR data.

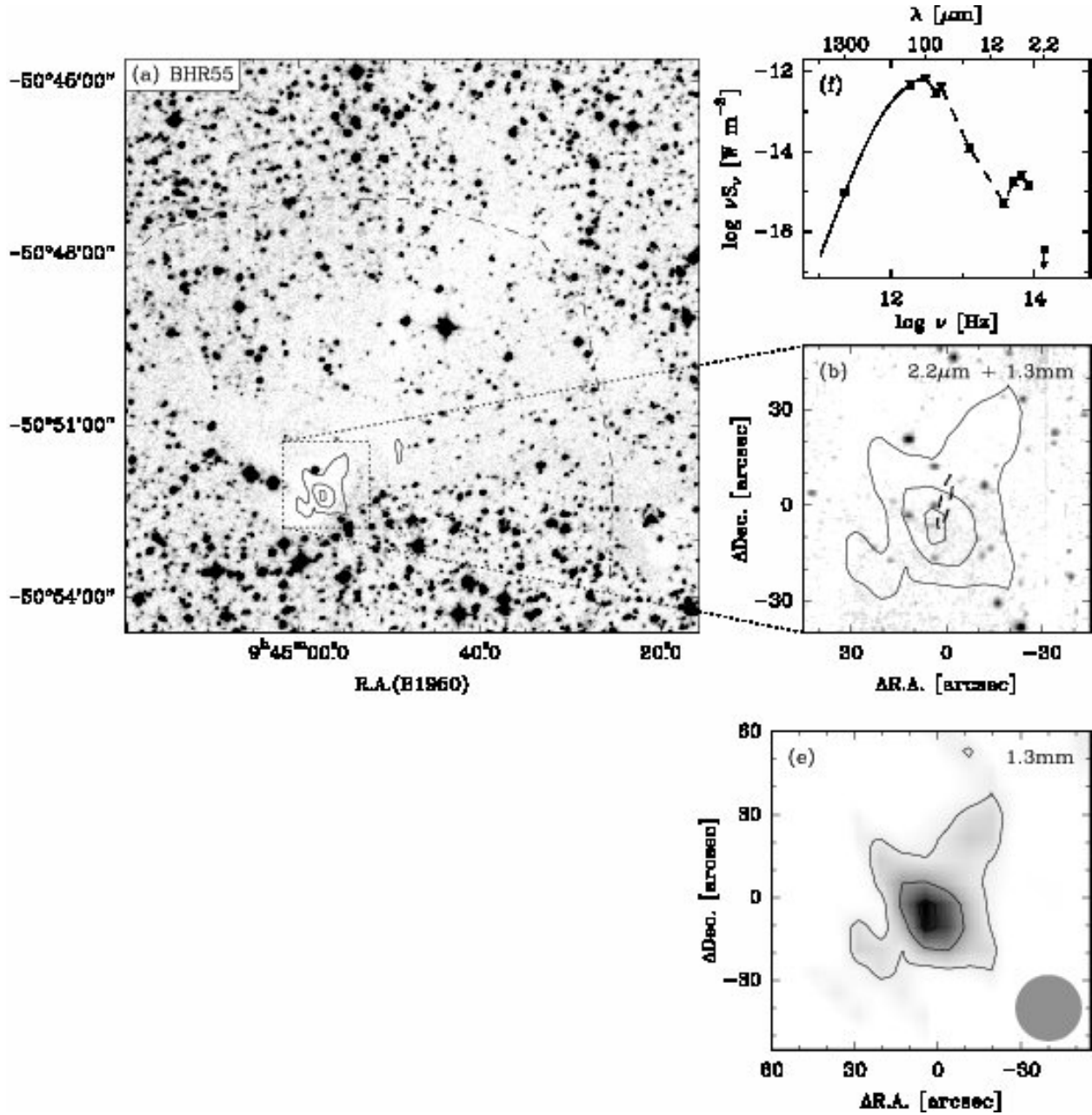


Fig. 9.— BHR 55: a) Optical image (DSS2 red) with contours of the 1.3 mm dust continuum emission overlaid. b) NIR K-band image with 1.3 mm dust continuum contours. The IRAS PSC position is marked by a dashed ellipse. c) 1.3 mm dust continuum emission; grey scale and contours at 55, 110, 165 mJy/beam. The beam size is indicated as a grey ellipse. d) Spectral energy distribution showing the SEST 1.3 mm, IRAS PSC, Spitzer MIPS and IRAC, and ground-based NIR data. Note that the association of the IRAC fluxes with the FIR/mm source is somewhat uncertain.

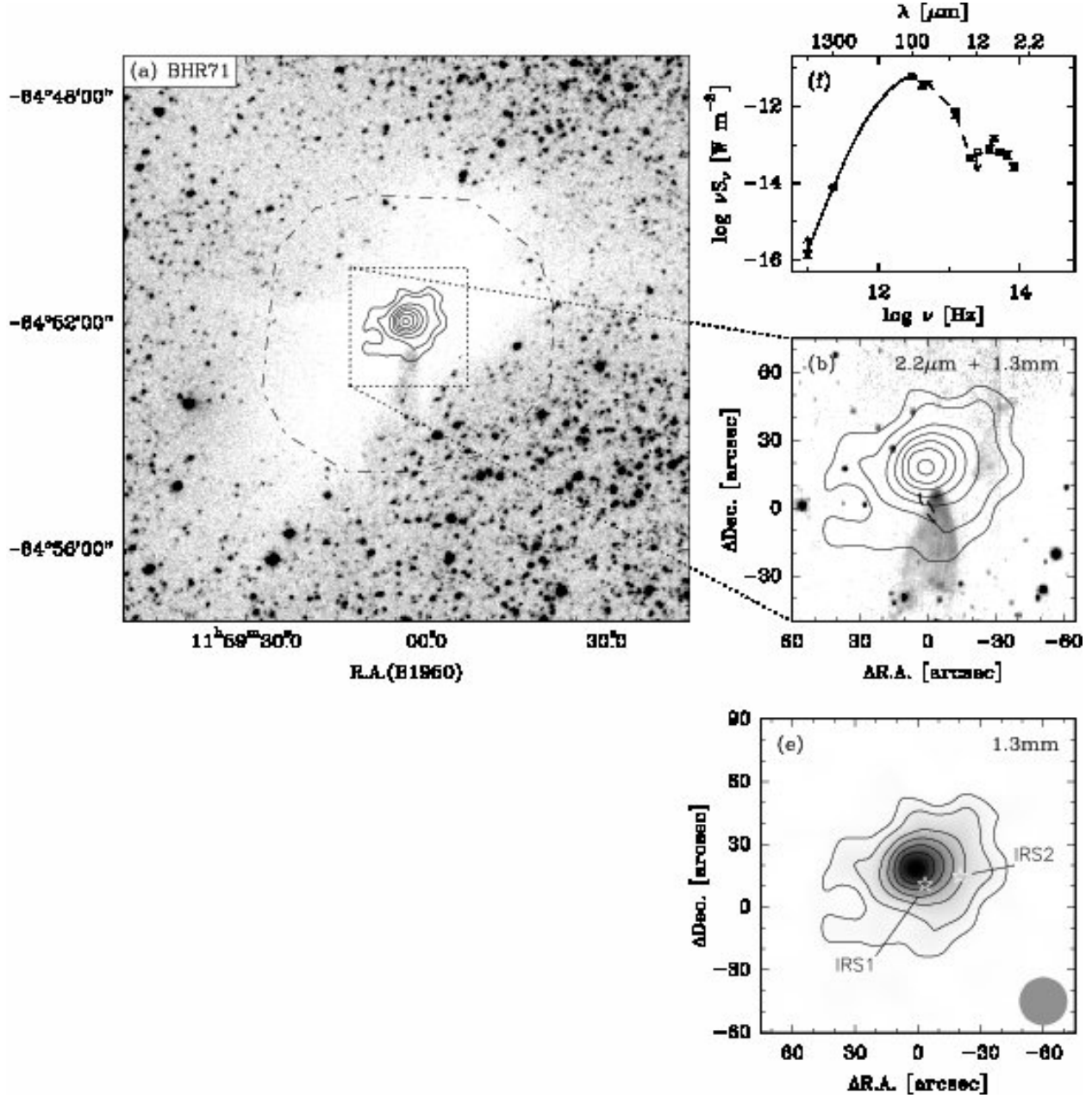


Fig. 10.— BHR 71: a) Optical image (DSS2 red) with contours of the 1.3 mm dust continuum emission overlaid (see Bourke et al. 1997). b) NIR K-band image with 1.3 mm dust continuum contours. The IRAS PSC position is marked by a dashed ellipse. c) 1.3 mm dust continuum emission; grey scale and contours at 100, 250 to 1750 by 300 mJy/beam. The beam size is indicated as a grey ellipse. Embedded infrared sources IRS1 and IRS2 refer to Bourke (2001). d) Spectral energy distribution showing the ATCA 3 mm, SEST 1.3 mm, SMA 1.1 mm, SCUBA 850 and 450  $\mu\text{m}$ , CSO 350  $\mu\text{m}$ , IRAS 100 to 12  $\mu\text{m}$ , MIPS 70 and 24  $\mu\text{m}$ , IRAC 8 to 3.6  $\mu\text{m}$ , as well as ISOCAM 15 and 7  $\mu\text{m}$  data. Note that this is a composite SED containing the sum of flux contributions from both IRS1 and IRS2.

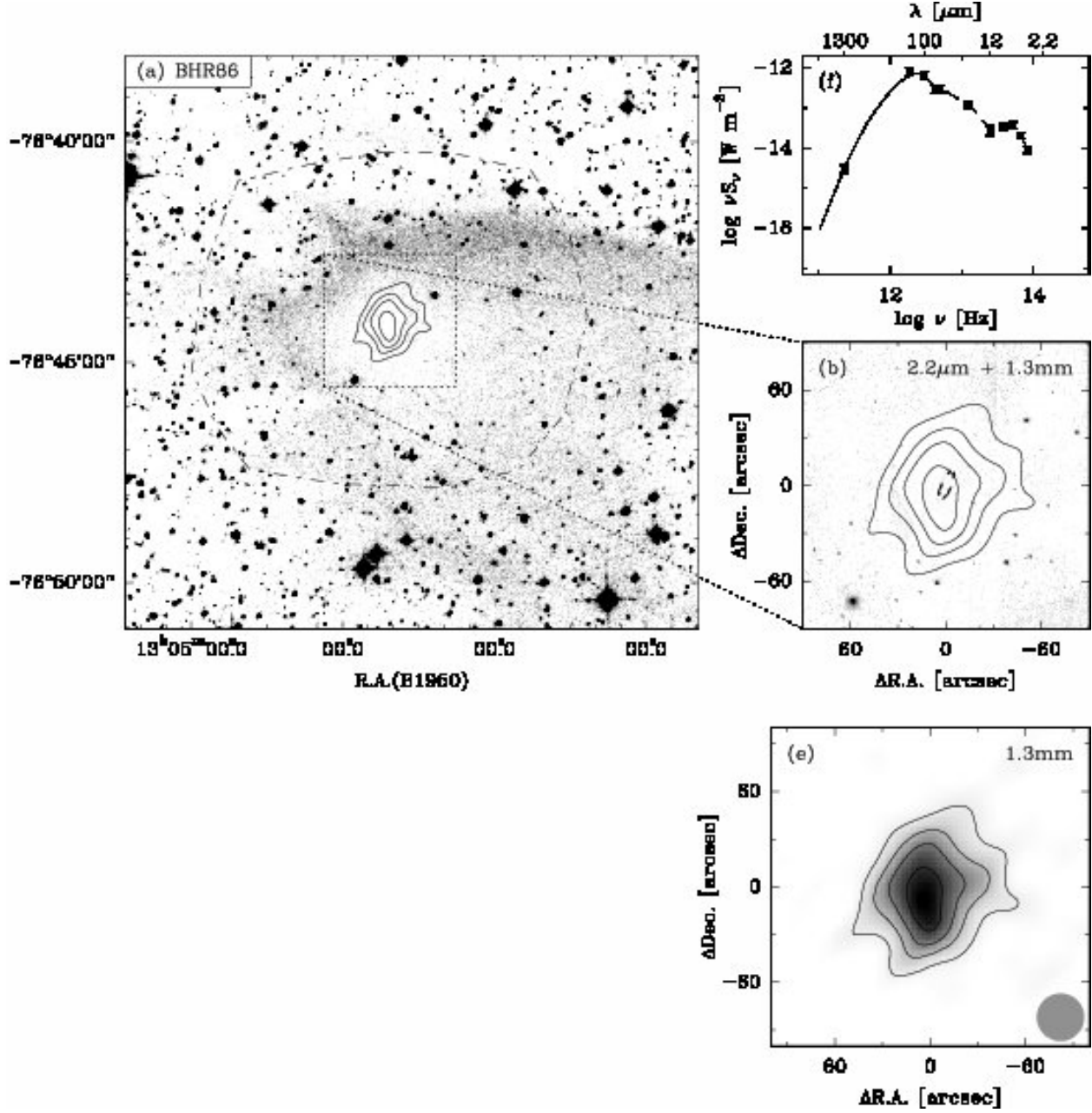


Fig. 11.— BHR 86: a) Optical image (DSS2 red) with contours of the 1.3 mm dust continuum emission overlaid. b) NIR K-band image with 1.3 mm dust continuum contours. The IRAS PSC position is marked by a dashed ellipse. c) 1.3 mm dust continuum emission; grey scale and contours at 75 to 315 by 80 mJy/beam. The beam size is indicated as a grey ellipse. d) Spectral energy distribution showing the SEST 1.3 mm, IRAS FSC, and Spitzer MIPS and IRAC data.



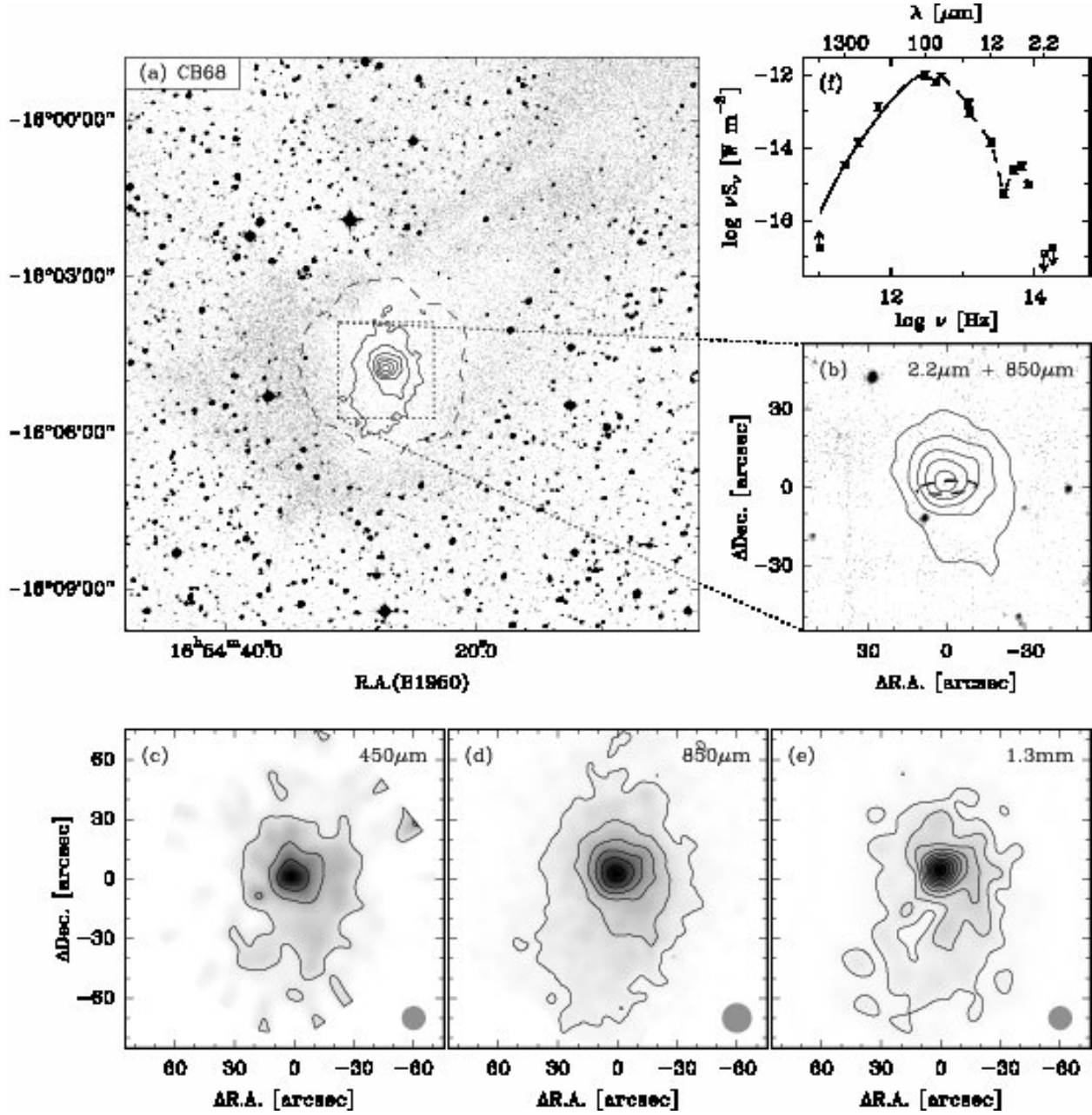


Fig. 12.— CB 68: a) Optical image (DSS2 red) with contours of the 850  $\mu\text{m}$  dust continuum emission overlaid. b) NIR K-band image with 850  $\mu\text{m}$  dust continuum contours. The IRAS PSC position is marked by a dashed ellipse. c) 450  $\mu\text{m}$  dust continuum emission; grey scale and contours at 1.2, 2.2, and 3.2 Jy/beam. d) 850  $\mu\text{m}$  dust continuum emission; grey scale and contours at 90 to 540 by 90 mJy/beam. e) 1.3 mm dust continuum emission; grey scale and contours at 18 to 162 by 18 mJy/beam. Beam sizes are indicated as grey ellipses. f) Spectral energy distribution showing the OVRO 3 mm, IRAM 1.3 mm, SCUBA 850 and 450  $\mu\text{m}$ , IRAS PSC and FSC, Spitzer MIPS and IRAC, and ground-based NIR data.



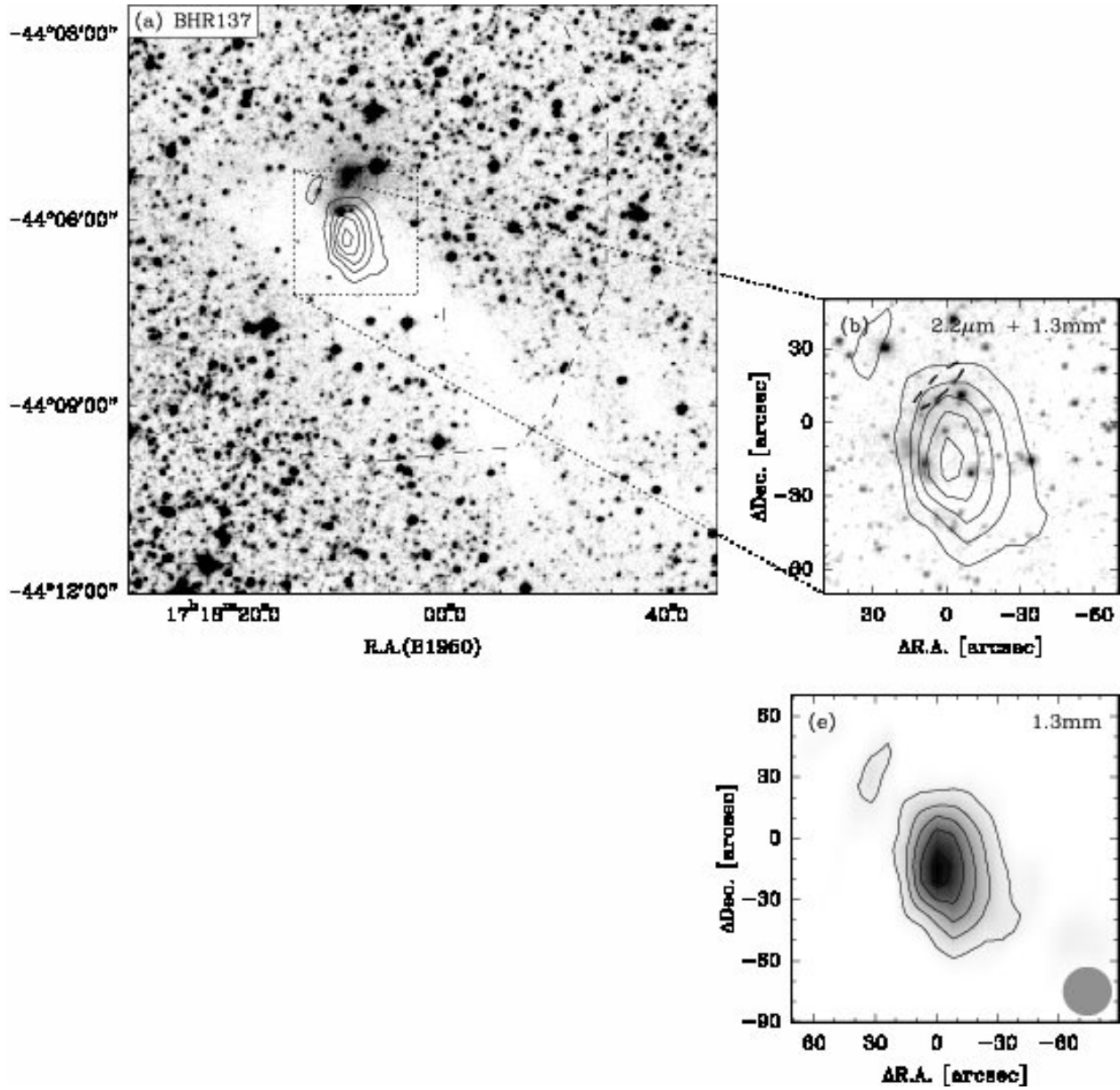


Fig. 13.— BHR 137: a) Optical image (DSS2 red) with contours of the 1.3 mm dust continuum emission overlaid. b) NIR K-band image with 1.3 mm dust continuum contours. The IRAS PSC position is marked by a dashed ellipse. c) 1.3 mm dust continuum emission; grey scale and contours at 70 to 350 by 70 mJy/beam. The beam size is indicated as a grey ellipse. No spectral energy distribution is shown since it is not clear which of the sources emitting at shorter wavelengths, if any, is associated with the mm source.

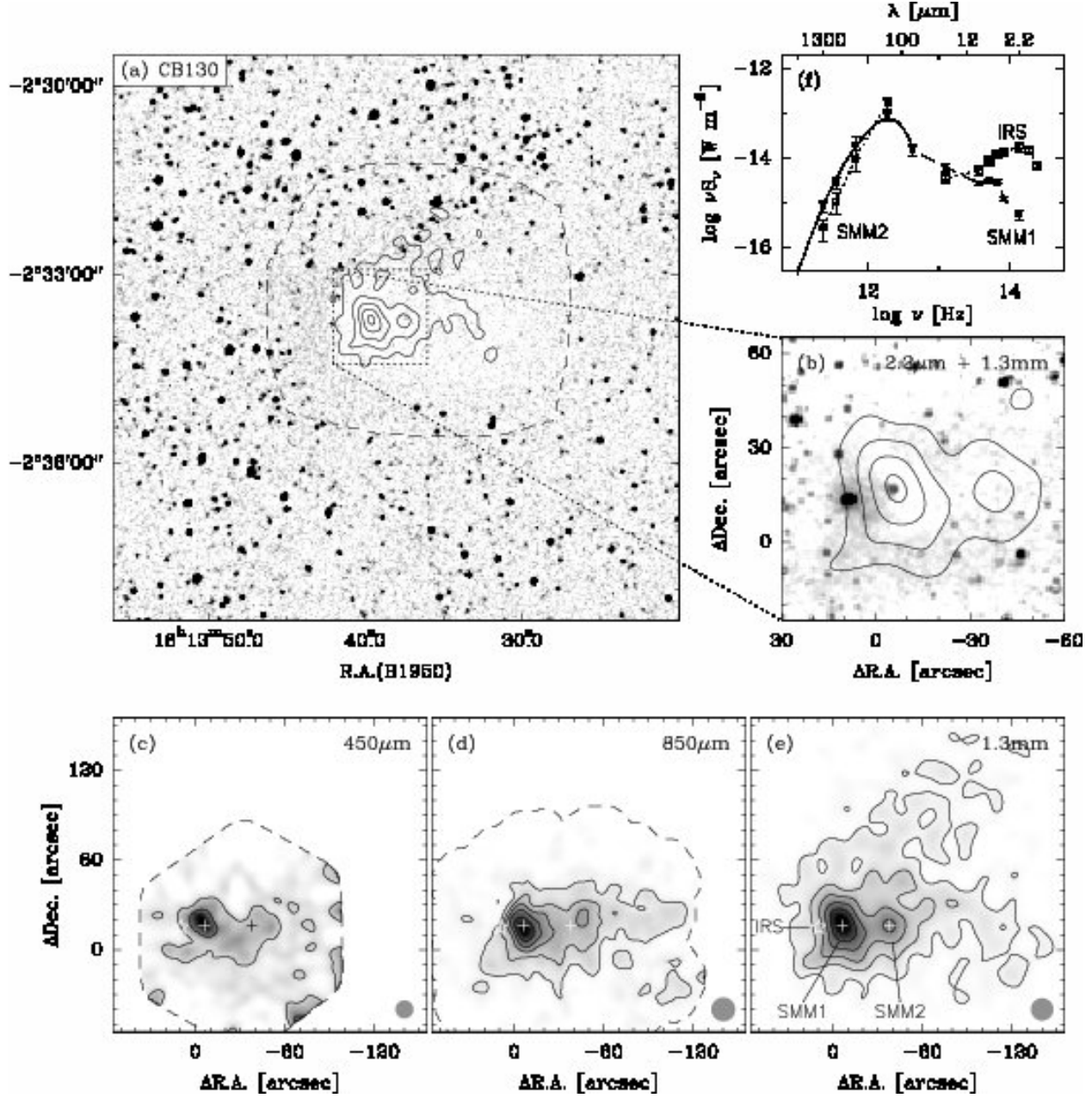


Fig. 14.— CB130: a) Optical image (DSS2 red) with contours of the 1.3 mm dust continuum emission overlaid. b) NIR K-band image with 1.3 mm continuum contours. c) 450 μm dust continuum emission; grey scale and contours at 0.5 and 1 Jy/beam. d) 850 μm dust continuum emission; grey scale and contours at 45 to 270 by 45 mJy/beam. e) 1.3 mm dust continuum emission; grey scale and contours at 12 to 72 by 12 mJy/beam. Beam sizes are indicated as grey ellipses. f) Spectral energy distribution of SMM1 (filled squares), SMM2 (submm only, empty squares), and IRS (NIR to MIR only, open circles), showing the IRAM 1.3 mm, SCUBA 850 and 450 μm, Spitzer MIPS and IRAC, and ground-based NIR data.

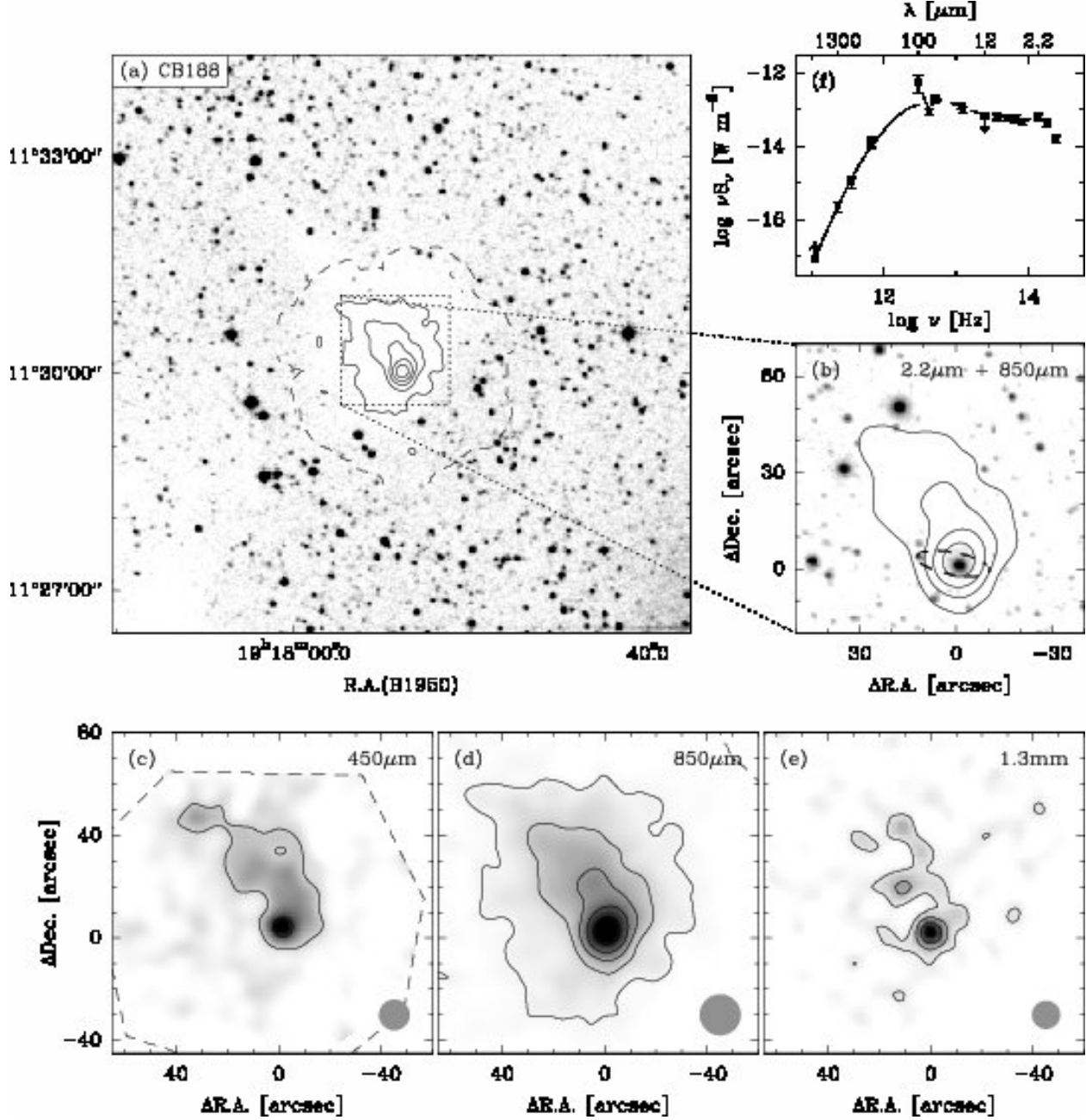


Fig. 15.— CB 188: a) Optical image (DSS2 red) with contours of the 850  $\mu\text{m}$  dust continuum emission overlaid. b) NIR K-band image with 850  $\mu\text{m}$  dust continuum contours. The IRAS PSC position is marked by a dashed ellipse. c) 450  $\mu\text{m}$  dust continuum emission; grey scale and contours at 0.45 and 0.9 Jy/beam. d) 850  $\mu\text{m}$  dust continuum emission; grey scale and contours at 40 to 160 by 40 mJy/beam. e) 1.3 mm dust continuum emission; grey scale and contours at 15 to 60 by 15 mJy/beam. Beam sizes are indicated as grey ellipses. f) Spectral energy distribution showing the OVRO 3 mm, IRAM 1.3 mm, SCUBA 850 and 450  $\mu\text{m}$ , IRAS PSC, Spitzer MIPS and IRAC, and ground-based NIR data.

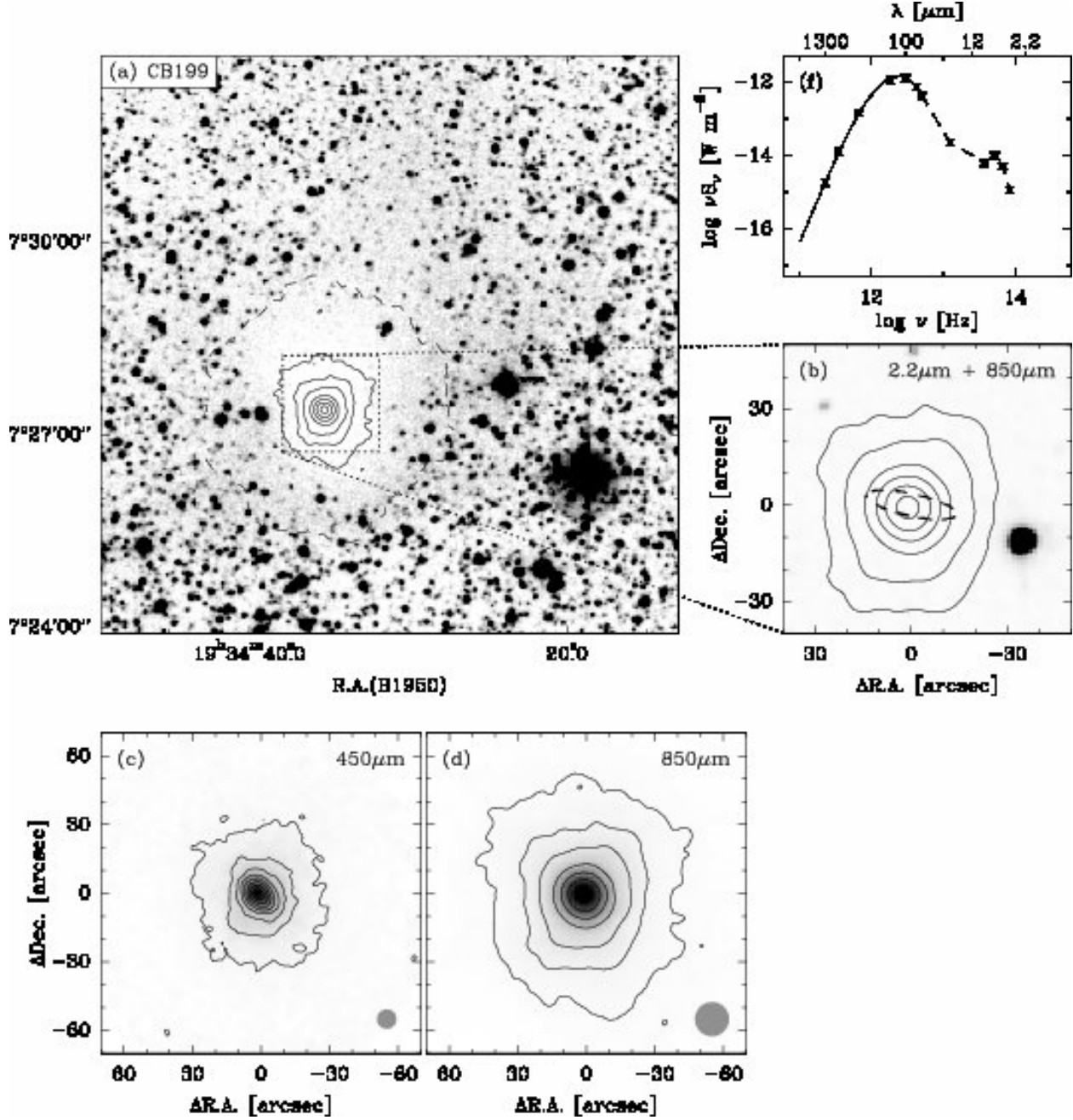


Fig. 16.— CB 199 (B 335): a) Optical image (DSS2 red) with contours of the 850  $\mu\text{m}$  dust continuum emission overlaid. b) NIR K-band image with 850  $\mu\text{m}$  dust continuum contours. The IRAS PSC position is marked by a dashed ellipse. c) 450  $\mu\text{m}$  dust continuum emission; grey scale and contours at 0.4 to 4.4 by 0.5 Jy/beam. d) 850  $\mu\text{m}$  dust continuum emission; grey scale and contours at 60, 120, 200 to 1000 by 200 mJy/beam. Beam sizes are indicated as grey ellipses. f) Spectral energy distribution showing the IRAM 1.3 mm (Motte & André 2001), SCUBA 850 and 450  $\mu\text{m}$ , IRAS PSC, and Spitzer MIPS and IRAC data.

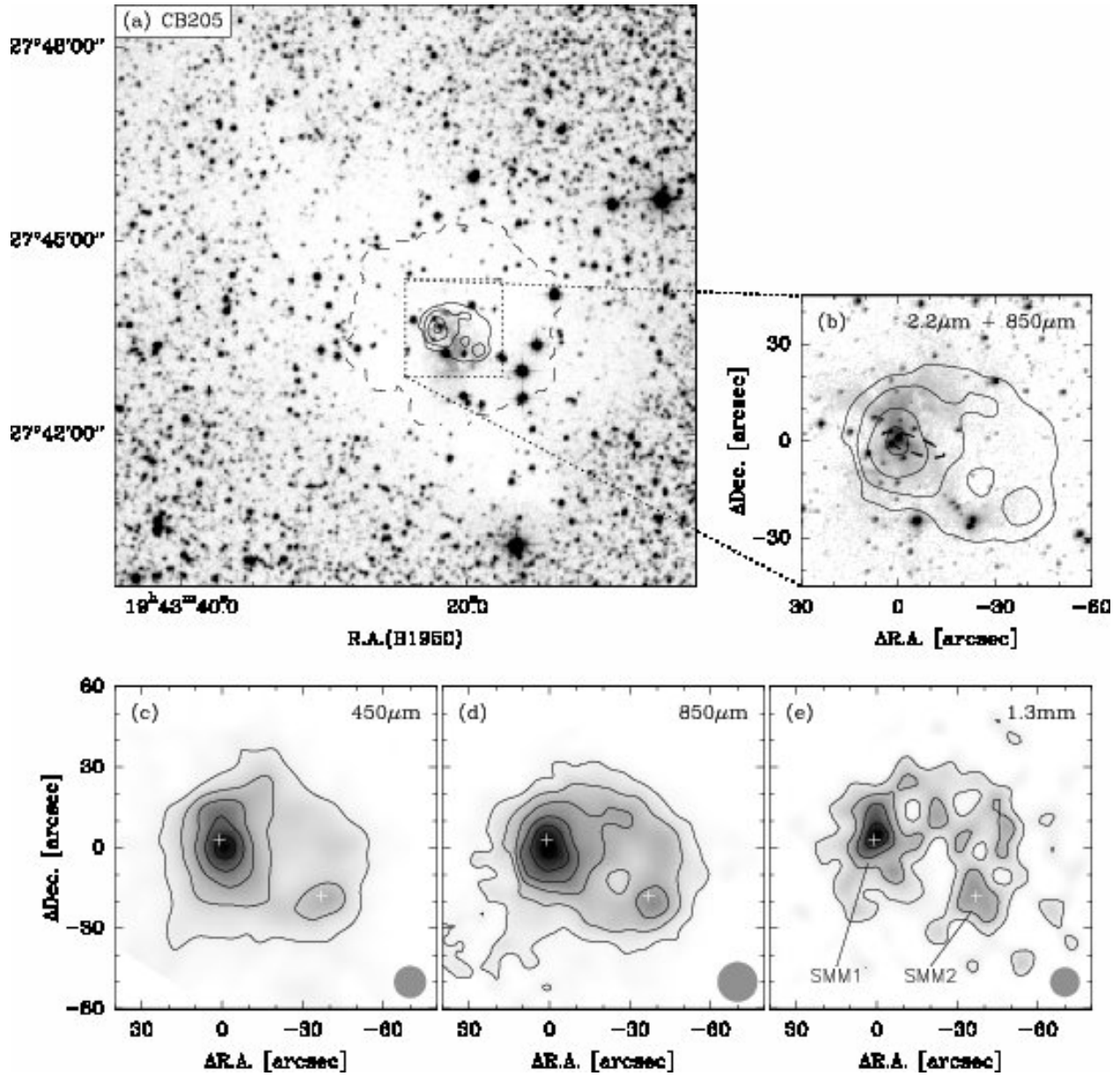


Fig. 17.— CB205: a) Optical image (DSS2 red) with contours of the  $850\mu\text{m}$  dust continuum emission overlaid. b) NIR K-band image with  $850\mu\text{m}$  dust continuum contours. The IRAS PSC position is marked by a dashed ellipse. c)  $450\mu\text{m}$  dust continuum emission; grey scale and contours at 0.65 to 3.05 by  $0.6\text{Jy/beam}$ . d)  $850\mu\text{m}$  dust continuum emission; grey scale and contours at 120 to 470 by  $70\text{mJy/beam}$ . e)  $1.3\text{mm}$  dust continuum emission; grey scale and contours at 16 to 64 by  $16\text{mJy/beam}$ . Beam sizes are indicated as grey ellipses. Crosses mark the positions of the two main  $1.3\text{mm}$  peaks. No spectral energy distribution is shown since many different, partially unresolved sources contribute to the measured flux densities.

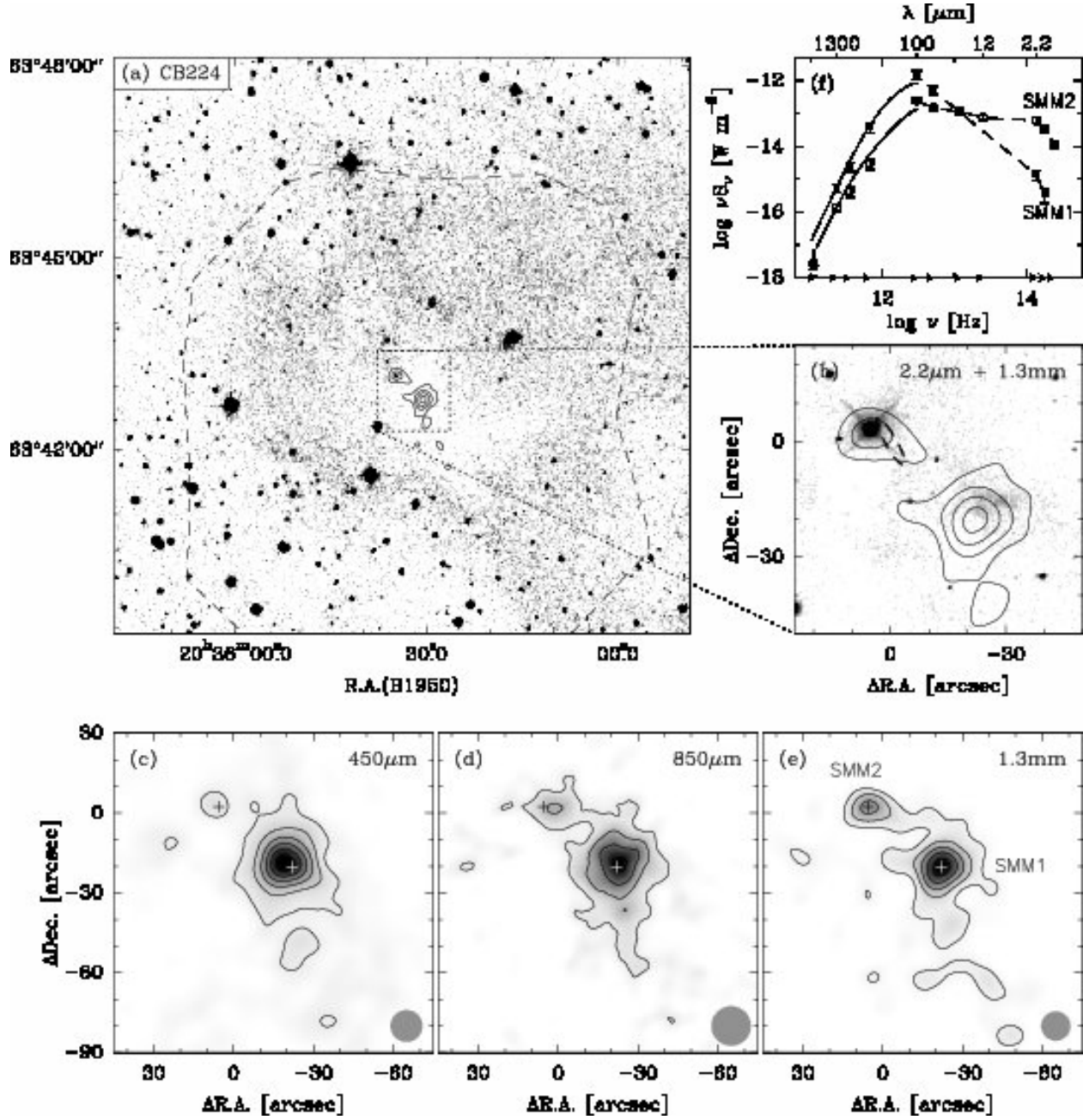


Fig. 18.— CB224: a) Optical image (DSS2 red) with contours of the 1.3 mm dust continuum emission overlaid. b) NIR K-band image with 1.3 mm dust continuum contours. The IRAS PSC position is marked by a dashed ellipse. c) 450  $\mu\text{m}$  dust continuum emission; grey scale and contours at 0.24 to 1.44 by 0.24 Jy/beam. d) 850  $\mu\text{m}$  dust continuum emission; grey scale and contours at 60 to 240 by 60 mJy/beam. e) 1.3 mm dust continuum emission; grey scale and contours at 12 to 60 by 12 mJy/beam. Beam sizes are indicated as grey ellipses. Crosses mark the positions of the two 1.3 mm peaks. f) Spectral energy distribution of SMM1 (filled squares) and SMM2 (open circles) showing the OVRO 3 mm, IRAM 1.3 mm, SCUBA 850 and 450  $\mu\text{m}$ , IRAS PSC and FSC, and ground-based NIR data.

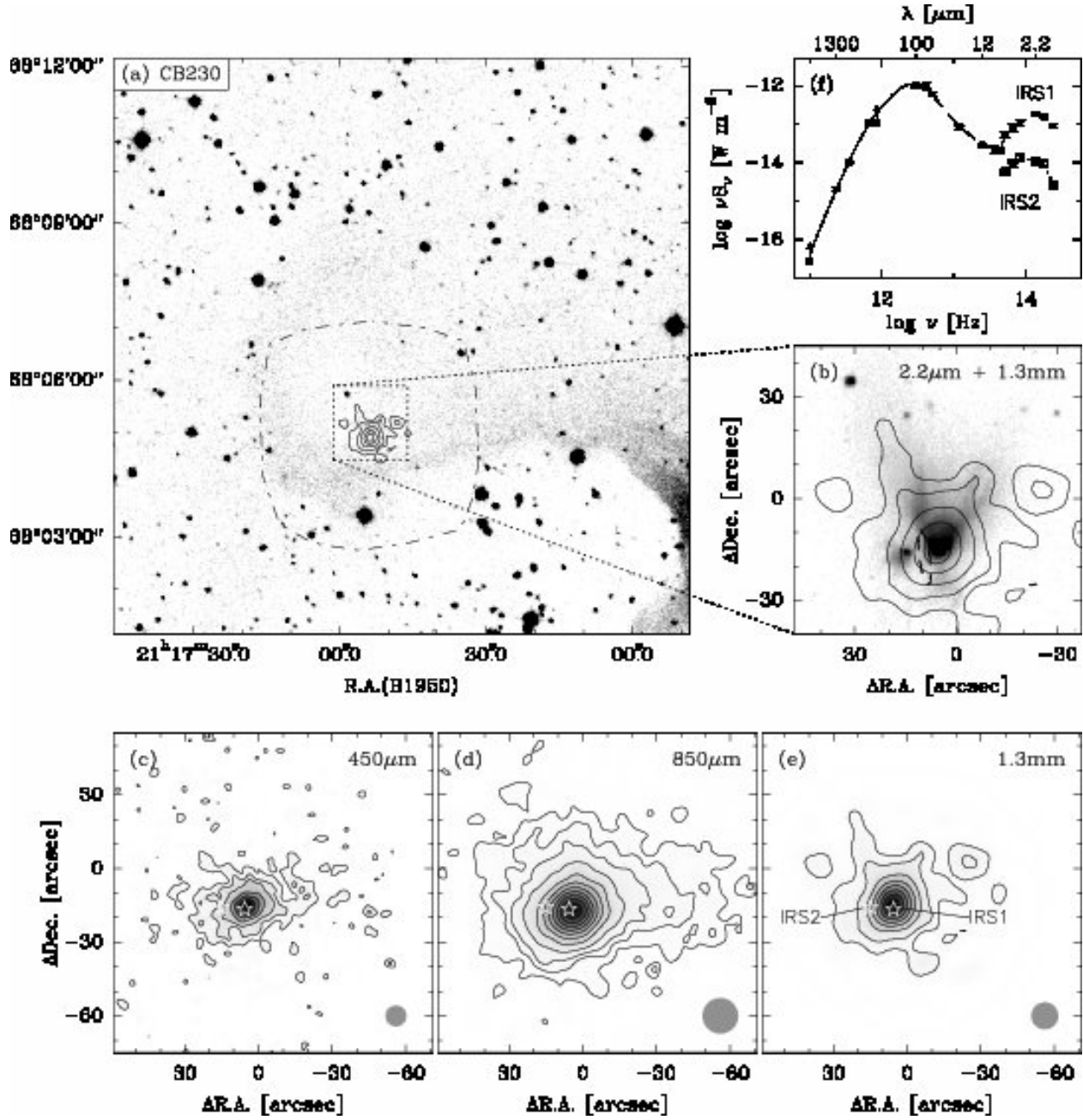


Fig. 19.— CB230: a) Optical image (DSS2 red) with contours of the 1.3 mm dust continuum emission overlaid. b) NIR K-band image with 1.3 mm dust continuum contours. The IRAS PSC position is marked by a dashed ellipse. c) 450  $\mu\text{m}$  dust continuum emission; grey scale and contours at 350, 700, 1050 to 3850 by 700 mJy/beam. d) 850  $\mu\text{m}$  dust continuum emission; grey scale and contours at 30, 60, 90, 150 to 900 by 100 mJy/beam. e) 1.3 mm dust continuum emission; grey scale and contours at 15, 30 to 210 by 30 mJy/beam. Beam sizes are indicated as grey ellipses. f) Spectral energy distributions of IRS1 (filled squares) and IRS2 (open circles, NIR to MIR only), showing the OVRO 3 mm, IRAM 1.3 mm, SCUBA 850 and 450  $\mu\text{m}$ , UKT14 350  $\mu\text{m}$ , IRAS PSC and FSC, Spitzer MIPS and IRAC 8 to 3.6  $\mu\text{m}$ , ISOCAM 6.7  $\mu\text{m}$ , and ground-based NIR data. Note that contributions from both IRS1 and IRS2 are included in the submm SED of SMM1 because the source is not resolved at wavelengths longward of 10  $\mu\text{m}$ . However, IRS1 dominates at all wavelengths.



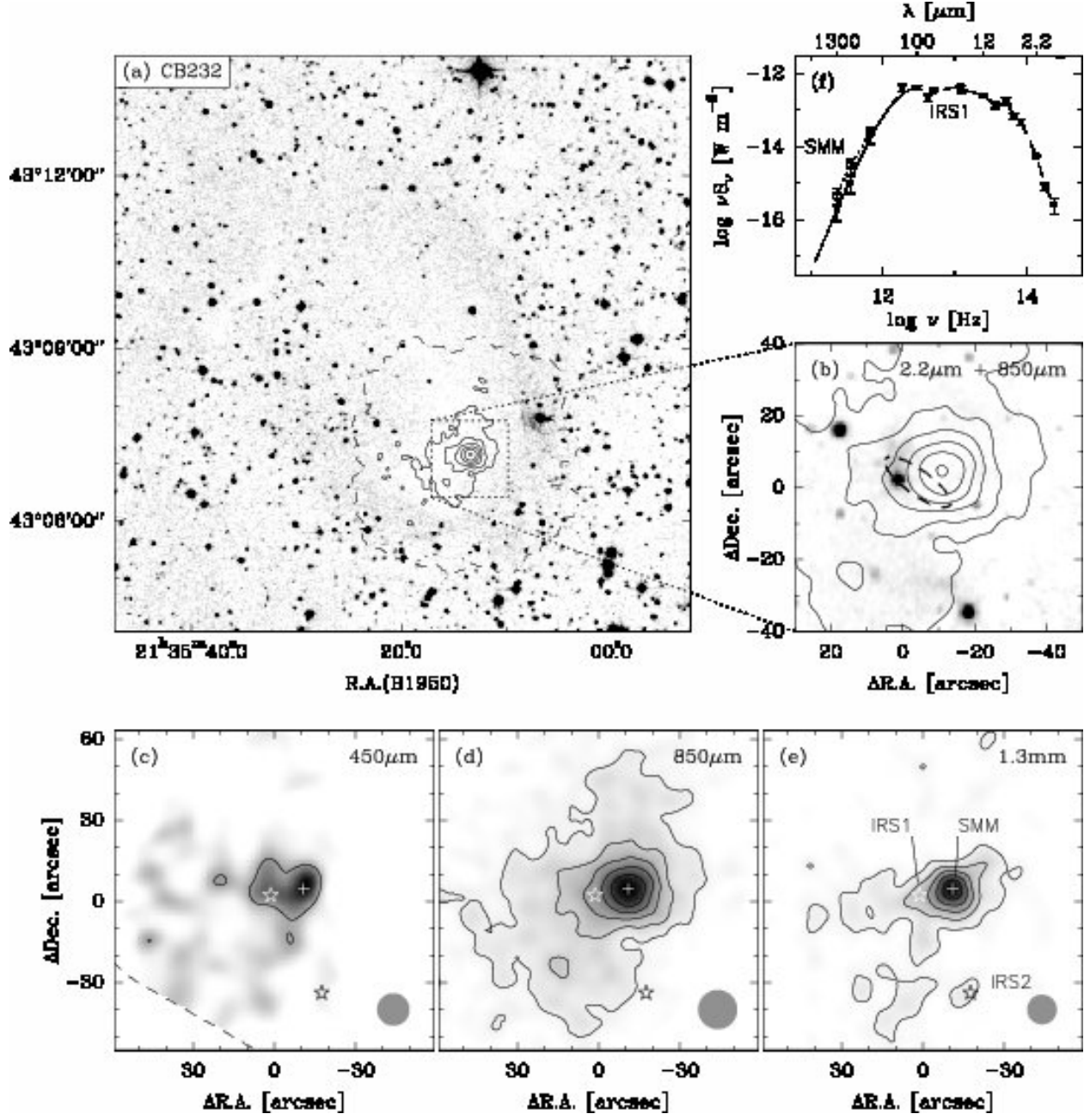


Fig. 20.— CB 232: a) Optical image (DSS2 red) with contours of the 850  $\mu\text{m}$  dust continuum emission overlaid. b) NIR K-band image with 850  $\mu\text{m}$  dust continuum contours. The IRAS PSC position is marked by a dashed ellipse. c) 450  $\mu\text{m}$  dust continuum emission; grey scale and contour at 1.4 mJy/beam. d) 850  $\mu\text{m}$  dust continuum emission; grey scale and contours at 70 to 320 by 50 mJy/beam. e) 1.3 mm dust continuum emission; grey scale and contours at 12 to 60 by 12 mJy/beam. Beam sizes are indicated as grey ellipses. The cross marks the position of SMM1 in the 1.3 mm map. Asterisks mark the position of the two nearby Spitzer IRS. f) Spectral energy distribution of CB 232 IRS1 (filled squares) and SMM (open circles, submm only), showing the IRAM 1.3 mm, SCUBA 850 and 450  $\mu\text{m}$ , IRAS PSC, Spitzer MIPS and IRAC, and ground-based NIR data.



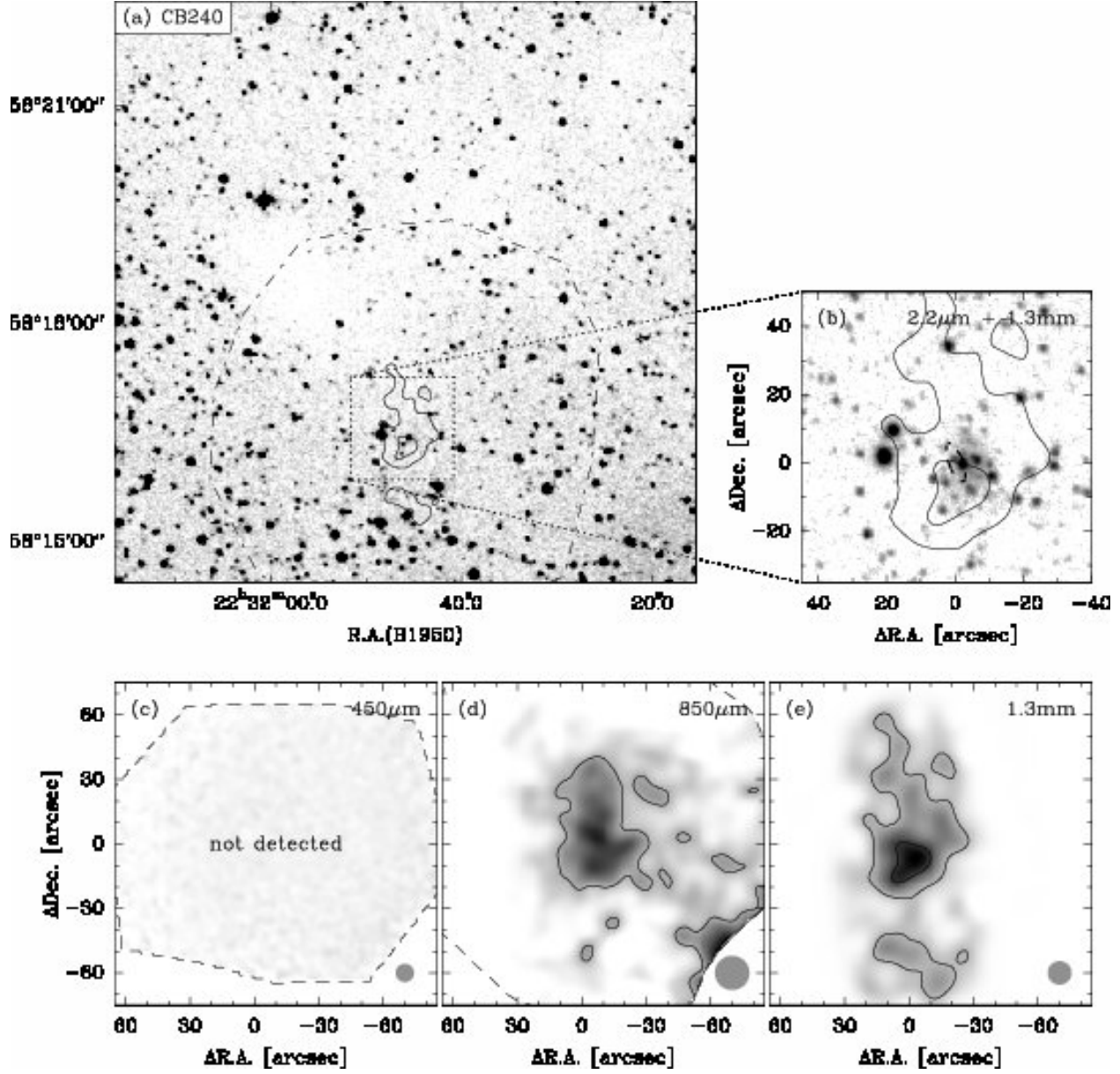


Fig. 21.— CB 240: a) Optical image (DSS2 red) with contours of the 1.3 mm dust continuum emission overlaid. b) NIR K-band image with 1.3 mm dust continuum contours. The IRAS PSC position is marked by a dashed ellipse. c) 450  $\mu\text{m}$  dust continuum map; the source is not detected at rms 170 mJy/beam. d) 850  $\mu\text{m}$  dust continuum emission; grey scale and contour at 100 mJy/beam. e) 1.3 mm dust continuum emission; grey scale and contours at 16 and 32 mJy/beam. Beam sizes are indicated as grey ellipses. No spectral energy distribution is shown since many different, partially unresolved sources contribute to the measured flux densities.

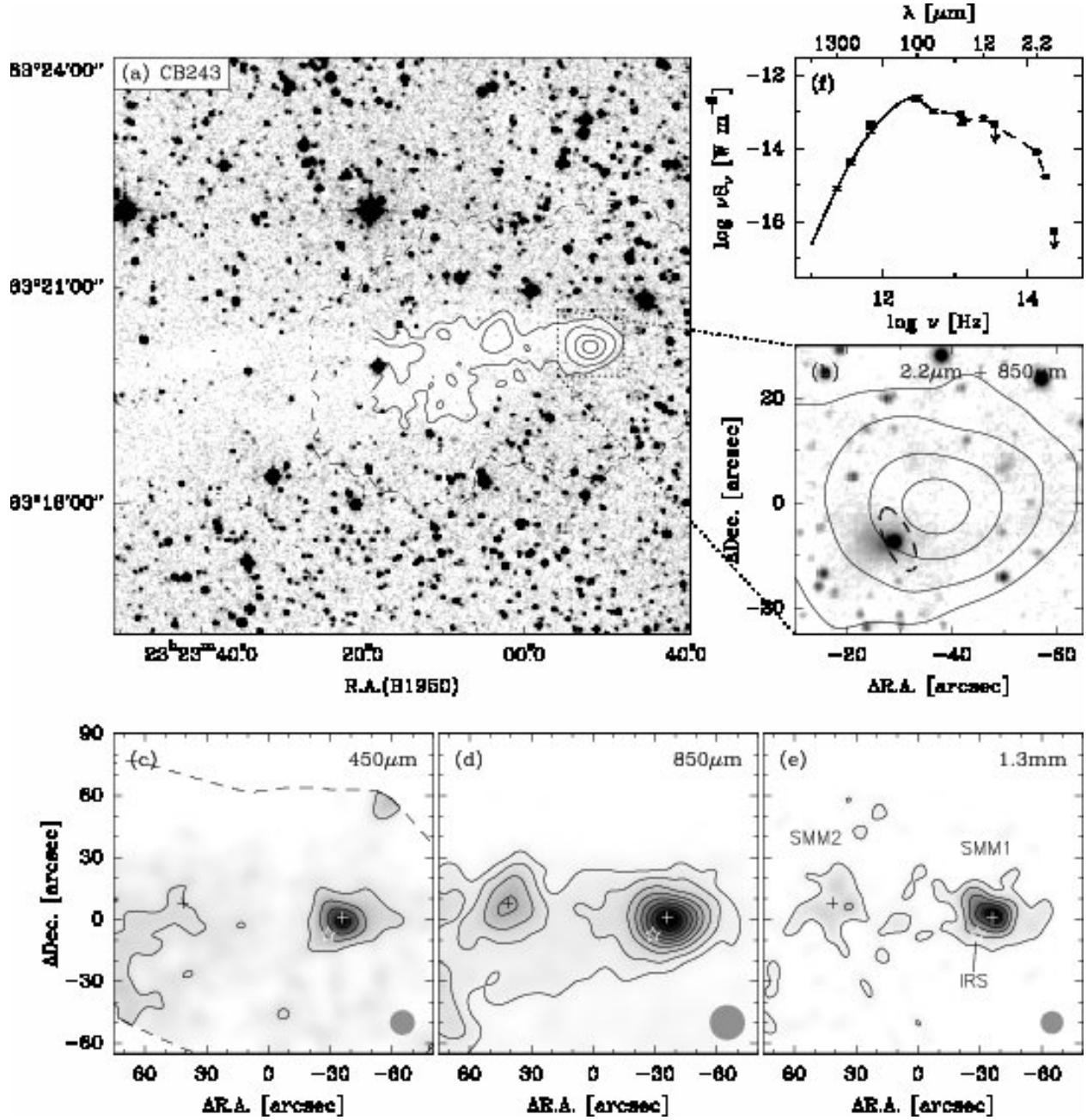


Fig. 22.— CB243: a) Optical image (DSS2 red) with contours of the 1.3 mm dust continuum emission overlaid. b) NIR K-band image with 1.3 mm dust continuum contours. The IRAS PSC position is marked by a dashed ellipse. c) 450  $\mu\text{m}$  dust continuum emission; grey scale and contours at 0.5 to 2 by 0.5 Jy/beam. d) 850  $\mu\text{m}$  dust continuum emission; grey scale and contours at 15 to 75 by 15 mJy/beam. Beam sizes are indicated as grey ellipses. Crosses mark the positions of SMM1 and SMM2. The asterisk marks the position of the reddened star and IRAS point source. f) Combined spectral energy distribution of SMM1 and IRS, showing the IRAM 1.3 mm, SCUBA 850 and 450  $\mu\text{m}$ , IRAS PSC, Spitzer MIPS, MSX, and ground-based NIR data. Fluxes are dominated by SMM1 at  $\lambda \geq 450 \mu\text{m}$  and by IRS at  $\lambda \leq 100 \mu\text{m}$ , but the two SEDs could not be separated.

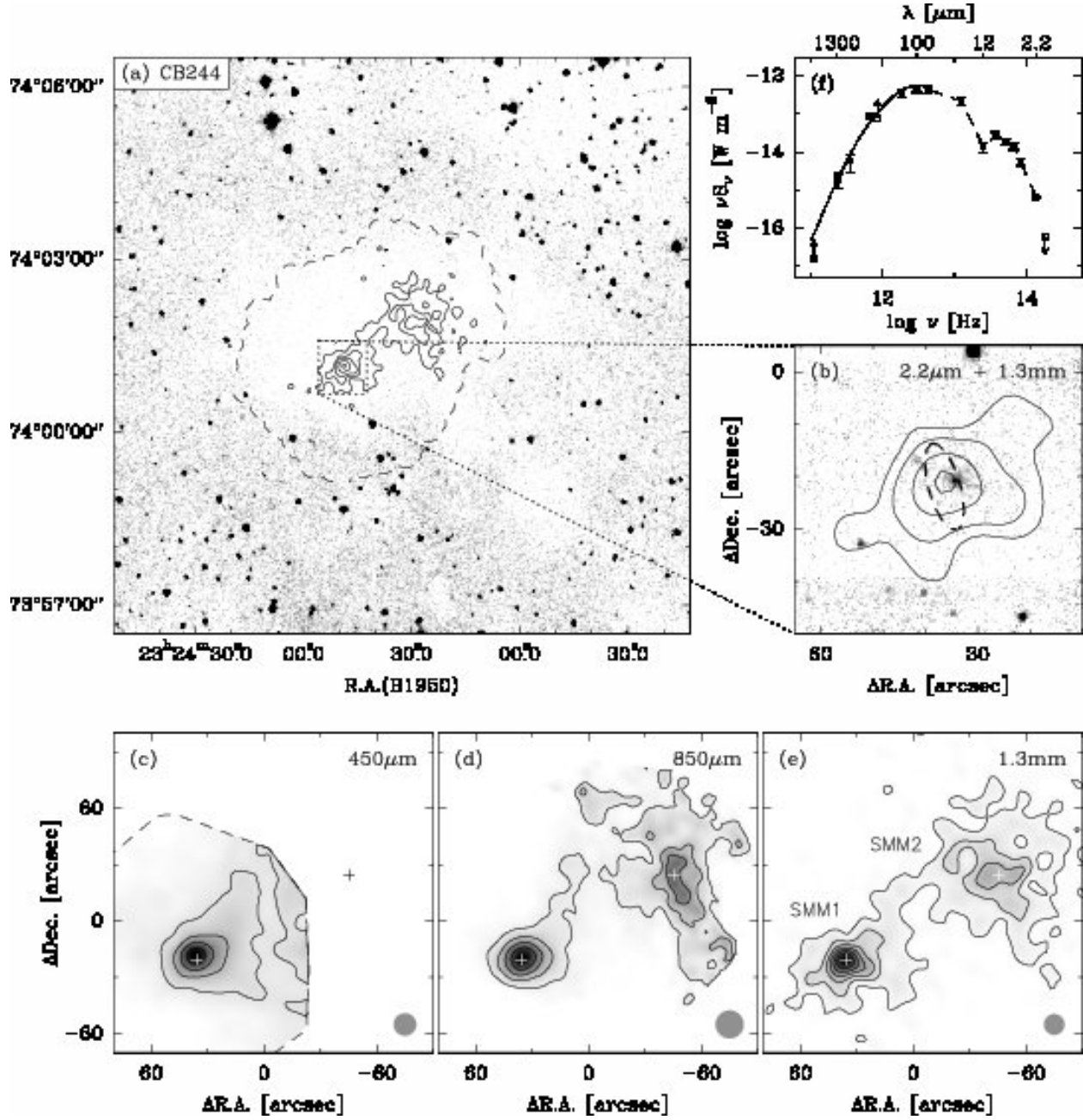


Fig. 23.— CB 244: a) Optical image (DSS2 red) with contours of the 1.3 mm dust continuum emission overlaid. b) NIR K-band image with 1.3 mm dust continuum contours. The IRAS PSC position is marked by a dashed ellipse. c) 450  $\mu\text{m}$  dust continuum emission; grey scale and contours at 0.6 to 2.2 by 0.5 Jy/beam. d) 850  $\mu\text{m}$  dust continuum emission; grey scale and contours at 100 to 500 by 80 mJy/beam. e) 1.3 mm dust continuum emission; grey scale and contours at 15 to 105 by 15 mJy/beam. Beam sizes are indicated as grey ellipses. Crosses mark the positions of SMM1 and SMM2. f) Spectral energy distribution of CB 244 MM 1 showing the OVRO 3 mm, IRAM 1.3 mm, SMA 1.1 mm, SCUBA 850 and 450  $\mu\text{m}$ , UKT14 350  $\mu\text{m}$ , IRAS PSC and FSC, Spitzer MIPS and IRAC, and ground-based NIR data.

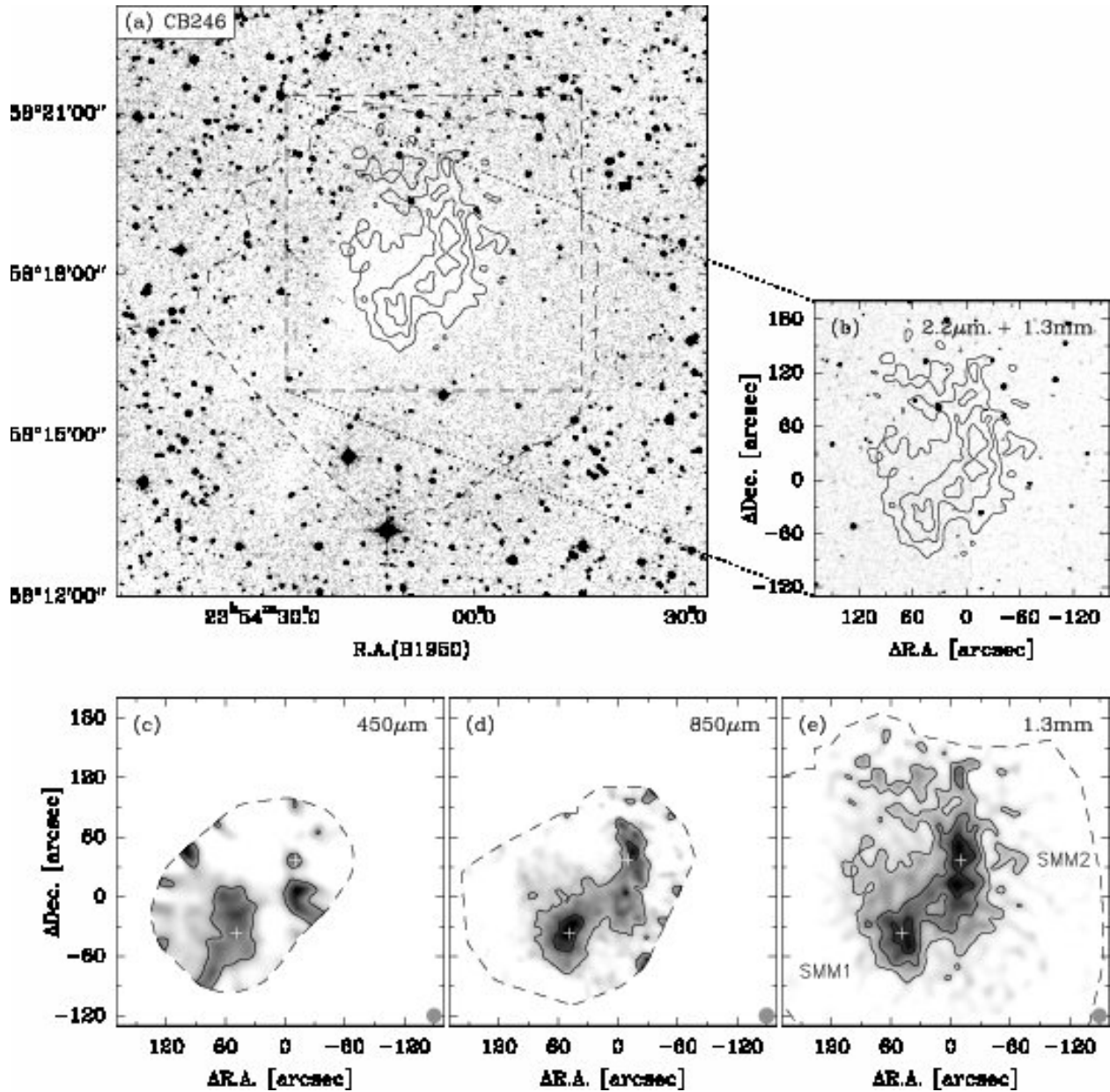


Fig. 24.— CB246: a) Optical image (DSS2 red) with contours of the 1.3 mm dust continuum emission overlaid. b) NIR K-band image with 1.3 mm dust continuum contours. c) 450  $\mu m$  dust continuum emission; grey scale and contour at 1.0 Jy/beam. d) 850  $\mu m$  dust continuum emission; grey scale and contours at 60 and 100 mJy/beam. e) 1.3 mm dust continuum emission; grey scale and contours at 15, 25, and 35 mJy/beam. Beam sizes are indicated as grey ellipses. Crosses mark the approximate central positions of the two main submm cores. No spectral energy distribution is shown because no fluxes are detected at wavelengths shortward of 450  $\mu m$ .

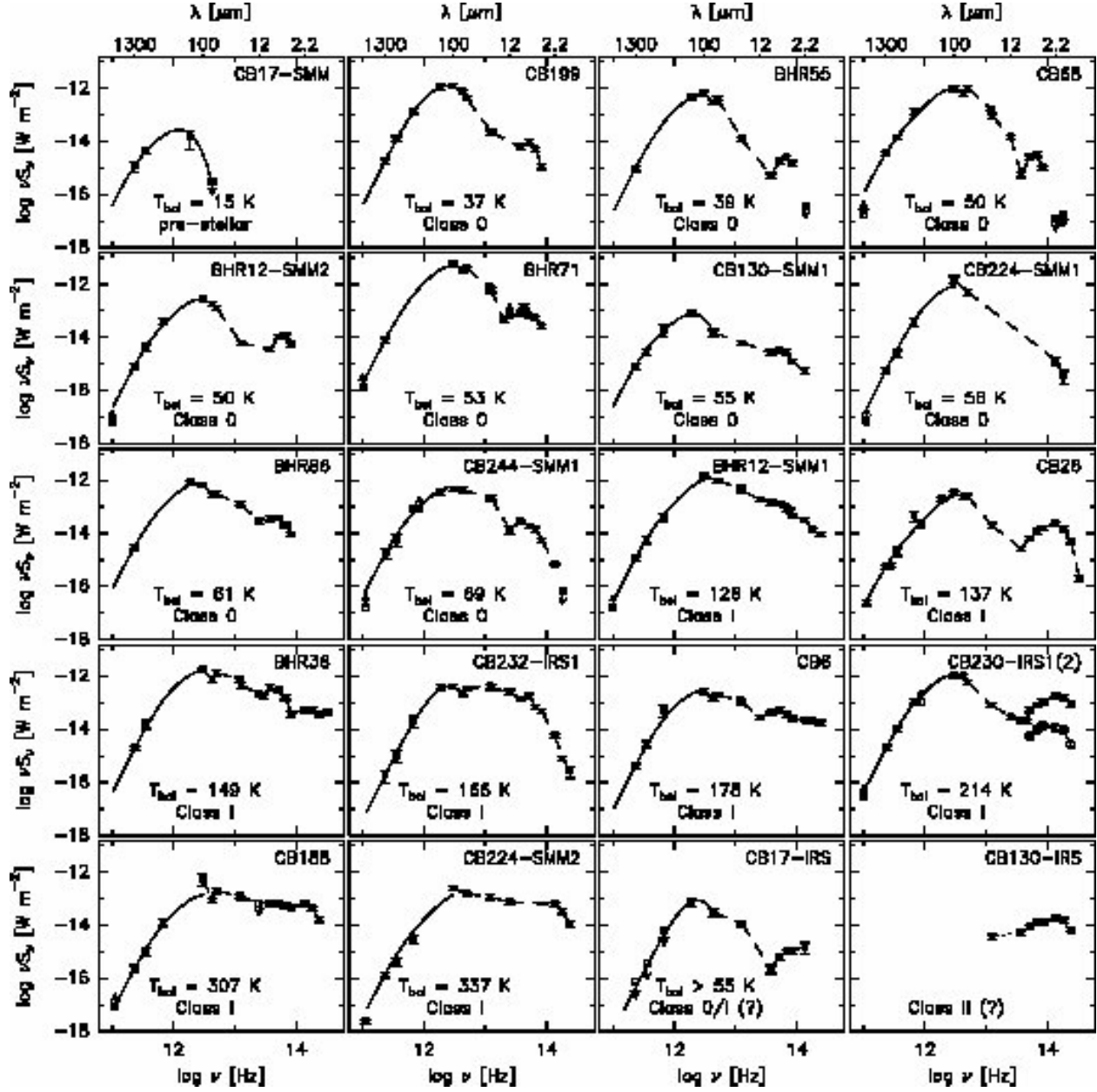


Fig. 25.— Compilation of SEDs (same as in Figs. 1 through 23), ordered by  $T_{\text{bol}}$  and evolutionary stage (cf. Table 7). Note that the classification of the last two sources (CB 17-IRS and CB 130-IRS) is uncertain because of missing long-wavelengths constraints to the SED.

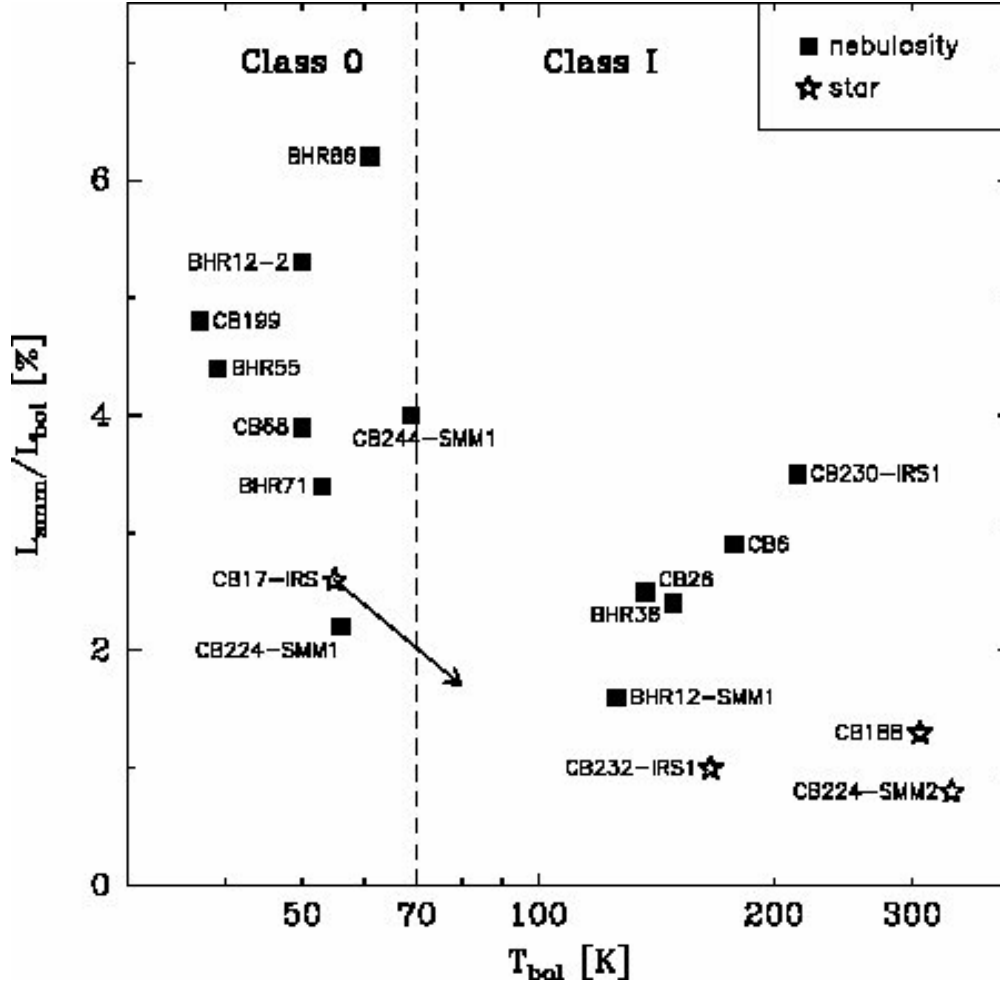


Fig. 26.— Ratio of submm to bolometric luminosity vs. bolometric temperature for the sources compiled in Table 7. The vertical dashed line marks the  $T_{\text{bol}} = 70$  K boundary between Class 0 and Class I sources proposed by Myers et al. (1998). Sources with NIR/MIR nebulosity only (i.e. no star-like point source) are marked as filled squares. Sources with NIR point source (star) are marked as open asterisks. See Sect. 4.1 for a discussion of evolutionary tracers.

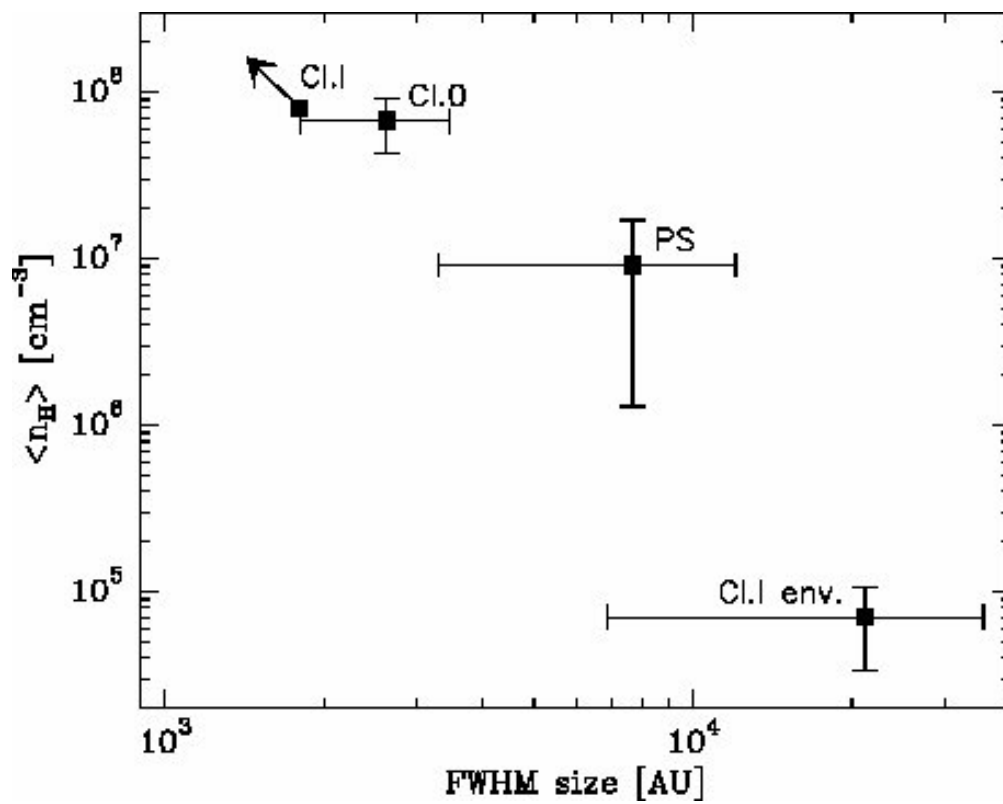


Fig. 27.— Mean FWHM core size and source-averaged density in globule cores as function of evolutionary stage (PS = prestellar core, Class 0 protostars, Class I YSO cores and extended envelopes). Note that most Class I sources exhibit unresolved (sub)mm sources with presumably significant flux contributions from circumstellar disks.

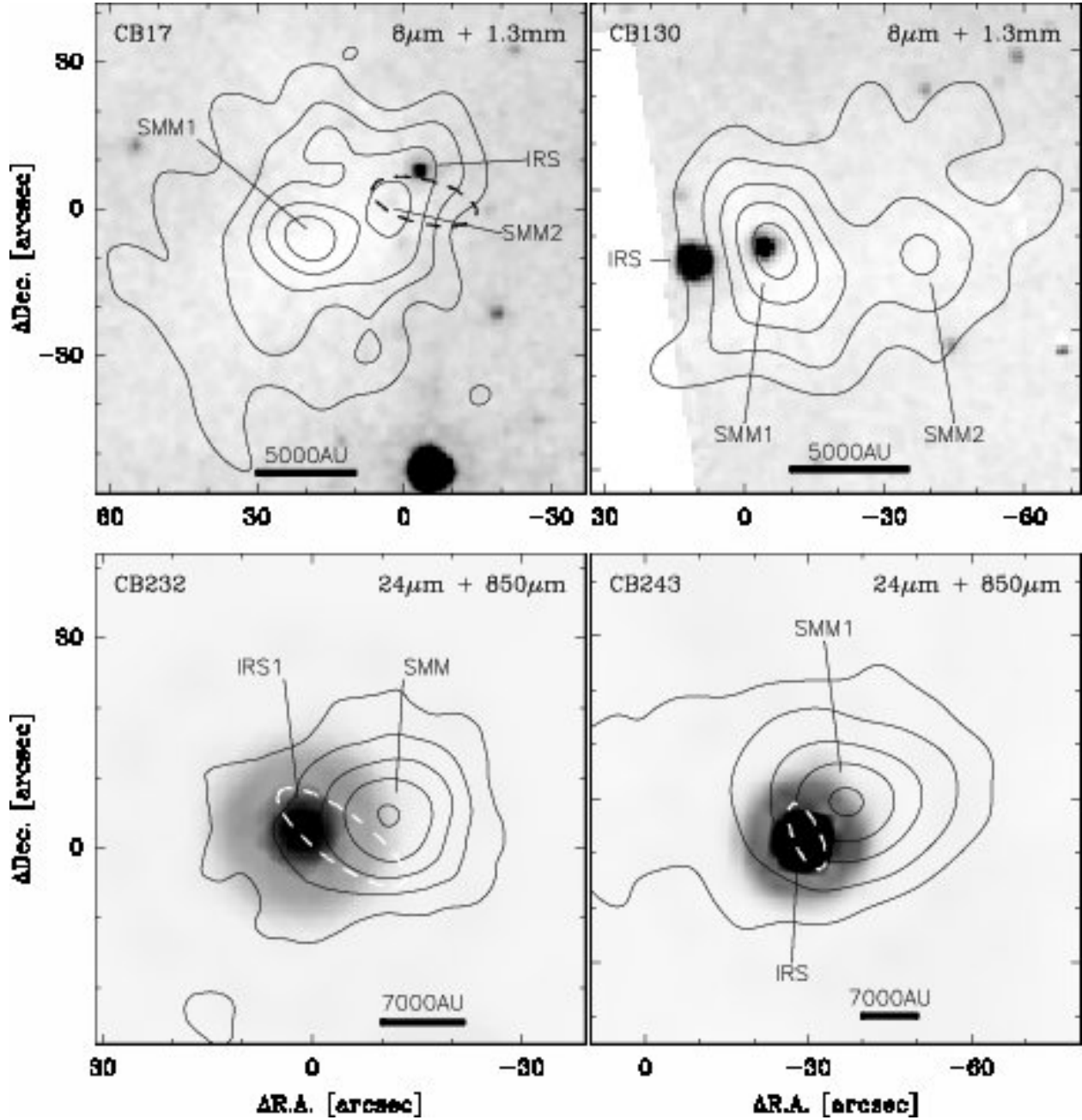


Fig. 28.— Four examples of globule cores in which MIR and submm sources are not identical and which obviously contain two or more sources of different evolutionary stage with a few thousand AU: *Top left*: CB 17, *IRAC*  $8\mu\text{m}$  image (greyscale) and  $1.3\text{ mm}$  dust continuum contours (see Fig. 2). *Top right*: CB 130, *IRAC*  $8\mu\text{m}$  image (greyscale) and  $1.3\text{ mm}$  dust continuum contours (see Fig. 14). *Bottom left*: CB 232, *MIPS*  $24\mu\text{m}$  image (greyscale) and  $850\mu\text{m}$  dust continuum contours (see Fig. 20). *Bottom right*: CB 243, *MIPS*  $24\mu\text{m}$  image (greyscale) and  $850\mu\text{m}$  dust continuum contours (see Fig. 22). IRAS PSC positions are marked by dashed error ellipses, where applicable. Linear scale bars refer to the distances listed in Table 2. See Sect. 4.2 for discussion.



## REFERENCES

- Adams, F. C., Lada, C. J., & Shu, F. H. 1987, *ApJ*, 312, 788
- Afonso, J. M., Yun, J. L., & Clemens, D. P. 1998, *AJ*, 115, 1111
- Alves, J., Hartmann, L., Briceno, C., & Lada, C. J. 1997, *AJ*, 113, 1395
- André, P. & Montmerle, T. 1994, *ApJ*, 420, 837
- André, P., Ward-Thompson, D., & Barsony, M. 1993, *ApJ*, 406, 122
- . 2000, *Protostars and Planets IV*, 59
- Archibald, E. N., Jenness, T., Holland, W. S., Coulson, I. M., Jessop, N. E., Stevens, J. A., Robson, E. I., Tilanus, R. P. J., Duncan, W. D., & Lightfoot, J. F. 2002, *MNRAS*, 336, 1
- Barnard, E. E., Frost, E. B., & Calvert, M. R. 1927, *A photographic atlas of selected regions of the Milky way* ([Washington] Carnegie institution of Washington, 1927.)
- Beckwith, S. V. W., Henning, T., & Nakagawa, Y. 2000, *Protostars and Planets IV*, 533
- Bergin, E. A. & Tafalla, M. 2007, *ARA&A*, 45, 339
- Bonnell, I. A. & Bate, M. R. 2006, *MNRAS*, 370, 488
- Bontemps, S., Ward-Thompson, D., & Andre, P. 1996, *A&A*, 314, 477
- Bourke, T. L. 2001, *ApJ*, 554, L91
- Bourke, T. L., Garay, G., Lehtinen, K. K., Koehnenkamp, I., Launhardt, R., Nyman, L., May, J., Robinson, G., & Hyland, A. R. 1997, *ApJ*, 476, 781
- Bourke, T. L., Hyland, A. R., & Robinson, G. 1995a, *MNRAS*, 276, 1052
- Bourke, T. L., Hyland, A. R., Robinson, G., James, S. D., & Wright, C. M. 1995b, *MNRAS*, 276, 1067
- Brouillet, N., Kaufman, M., Combes, F., Baudry, A., & Bash, F. 1998, *A&A*, 333, 92
- Caselli, P., Benson, P. J., Myers, P. C., & Tafalla, M. 2002, *ApJ*, 572, 238
- Cecchi-Pestellini, C., Casu, S., & Scappini, F. 2001, *MNRAS*, 326, 1255
- Chabrier, G. 2003, *ApJ*, 586, L133
- Chandler, C. J., Gear, W. K., Sandell, G., Hayashi, S., Duncan, W. D., Griffin, M. J., & Hazella, S. 1990, *MNRAS*, 243, 330
- Chandler, C. J. & Sargent, A. I. 1993, *ApJ*, 414, L29
- Chen, H., Myers, P. C., Ladd, E. F., & Wood, D. O. S. 1995, *ApJ*, 445, 377
- Chen, X., Bourke, T. L., Launhardt, R., & Henning, T. 2008a, *ApJ*, 686, L107
- Chen, X., Launhardt, R., Bourke, T. L., Henning, T., & Barnes, P. J. 2008b, *ApJ*, 683, 862
- Chen, X., Launhardt, R., & Henning, T. 2007, *ApJ*, 669, 1058
- Chini, R., Kämpgen, K., Reipurth, B., Albrecht, M., Kreysa, E., Lemke, R., Nielbock, M., Reichertz, L. A., Sievers, A., & Zylka, R. 2003, *A&A*, 409, 235
- Clemens, D. P. & Barvainis, R. 1988, *ApJS*, 68, 257
- Clemens, D. P., Yun, J. L., & Heyer, M. H. 1991, *ApJS*, 75, 877
- Codella, C., Brand, J., Massi, F., Wouterloot, J. G. A., & Davis, G. R. 2006, *A&A*, 457, 891
- Codella, C. & Muters, D. 1997, *MNRAS*, 291, 337
- Codella, C. & Scappini, F. 1998, *MNRAS*, 298, 1092
- . 2003, *MNRAS*, 344, 1257
- Cohen, M. 1980, *AJ*, 85, 29
- Corporon, P. & Reipurth, B. 1997, in *IAU Symposium*, Vol. 182, *Herbig-Haro Flows and the Birth of Stars*, ed. B. Reipurth & C. Bertout, 85
- Crapsi, A., Caselli, P., Walmsley, C. M., Myers, P. C., Tafalla, M., Lee, C. W., & Bourke, T. L. 2005, *ApJ*, 619, 379
- Dame, T. M., Ungerechts, H., Cohen, R. S., de Geus, E. J., Grenier, I. A., May, J., Murphy, D. C., Nyman, L.-A., & Thaddeus, P. 1987, *ApJ*, 322, 706
- De Vries, C. H., Narayanan, G., & Snell, R. L. 2002, *ApJ*, 577, 798

- Dickman, R. L. & Clemens, D. P. 1983, *ApJ*, 271, 143
- Dopita, M. A., Evans, I., & Schwartz, R. D. 1982, *ApJ*, 263, L73
- Draine, B. T. & Lee, H. M. 1984, *ApJ*, 285, 89
- Duquennoy, A. & Mayor, M. 1991, *A&A*, 248, 485
- Eiroa, C., Torrelles, J. M., Miranda, L. F., Anglada, G., & Estalella, R. 1994, *A&AS*, 108, 73
- Eisenhardt, P., Dickinson, M., Stanford, S., Ward, J., & Valdes, F. 1996, DIMSUM - IRAF external package
- Elias, J. H., Frogel, J. A., Matthews, K., & Neugebauer, G. 1982, *AJ*, 87, 1029
- Emerson, D. T., Klein, U., & Haslam, C. G. T. 1979, *A&A*, 76, 92
- Enoch, M. L., Evans, N. J., Sargent, A. I., & Glenn, J. 2009, *ApJ*, 692, 973
- Frerking, M. A. & Langer, W. D. 1982, *ApJ*, 256, 523
- Froebrich, D. 2005, *ApJS*, 156, 169
- Gezari, D. Y., Pitts, P. S., & Schmitz, M. 1999, *VizieR Online Data Catalog*, 2225, 0
- Gómez, J. F., de Gregorio-Monsalvo, I., Suárez, O., & Kuiper, T. B. H. 2006, *AJ*, 132, 1322
- Goodwin, S. P., Nutter, D., Kroupa, P., Ward-Thompson, D., & Whitworth, A. P. 2008, *A&A*, 477, 823
- Griffin, M. J. & Orton, G. S. 1993, *Icarus*, 105, 537
- Hawarden, T. G., Leggett, S. K., Letawsky, M. B., Balantyne, D. R., & Casali, M. M. 2001, *MNRAS*, 325, 563
- Henning, T. & Launhardt, R. 1998, *A&A*, 338, 223
- Henning, T., Wolf, S., Launhardt, R., & Waters, R. 2001, *ApJ*, 561, 871
- Hilton, J. & Lahulla, J. F. 1995, *A&AS*, 113, 325
- Hodapp, K. 1998, *ApJ*, 500, L183
- Hodapp, K.-W. & Ladd, E. F. 1995, *ApJ*, 453, 715
- Holland, W. S., Robson, E. I., Gear, W. K., Cunningham, C. R., Lightfoot, J. F., Jenness, T., Ivison, R. J., Stevens, J. A., Ade, P. A. R., Griffin, M. J., Duncan, W. D., Murphy, J. A., & Naylor, D. A. 1999, *MNRAS*, 303, 659
- Huard, T. L., Sandell, G., & Weintraub, D. A. 1999, *ApJ*, 526, 833
- Huard, T. L., Weintraub, D. A., & Sandell, G. 2000, *A&A*, 362, 635
- Jenness, T. & Lightfoot, J. F. 1998, in *ASP Conf. Ser. 145: Astronomical Data Analysis Software and Systems VII*, 216
- Jenness, T., Lightfoot, J. F., & Holland, W. S. 1998, in *Proc. SPIE Vol. 3357, p. 548-558, Advanced Technology MMW, Radio, and Terahertz Telescopes*, Thomas G. Phillips; Ed., 548–558
- Kainulainen, J., Lehtinen, K., Väisänen, P., Bronfman, L., & Knude, J. 2007, *A&A*, 463, 1029
- Kane, B. D., Clemens, D. P., Leach, R. W., & Barvainis, R. 1995, *ApJ*, 445, 269
- Kane, B. D., Clemens, D. P., & Myers, P. C. 1994, *ApJ*, 433, L49
- Keene, J., Davidson, J. A., Harper, D. A., Hildebrand, R. H., Jaffe, D. T., Loewenstein, R. F., Low, F. J., & Pernic, R. 1983, *ApJ*, 274, L43
- Khanzadyan, T., Smith, M. D., Gredel, R., Stanke, T., & Davis, C. J. 2002, *A&A*, 383, 502
- Knude, J., Jönch-Sørensen, H., & Nielsen, A. S. 1999, *A&A*, 350, 985
- Kreysa, E., Gemuend, H.-P., Gromke, J., Haslam, C. G., Reichertz, L., Haller, E. E., Beeman, J. W., Hansen, V., Sievers, A., & Zylka, R. 1998, in *Presented at the Society of Photo-Optical Instrumentation Engineers (SPIE) Conference, Vol. 3357, Proc. SPIE Vol. 3357, p. 319-325, Advanced Technology MMW, Radio, and Terahertz Telescopes*, Thomas G. Phillips; Ed., ed. T. G. Phillips, 319–325
- Kroupa, P. 2002, *Science*, 295, 82
- Lada, C. J. 1987, in *IAU Symposium, Vol. 115, Star Forming Regions*, ed. M. Peimbert & J. Jugaku, 1–17
- Launhardt, R. 1996, PhD thesis, University of Jena

- Launhardt, R. 2001, in IAU Symposium, Vol. 200, The Formation of Binary Stars, ed. H. Zinnecker & R. Mathieu, 117
- Launhardt, R. 2005, in The Young Local Universe, Proc. of the 39th Rencontres de Moriond, ed. A. Chalabaev, T. Montmerle, & J. Trân Thanh Vân, 181
- Launhardt, R., Evans, N. J., Wang, Y., Clemens, D. P., Henning, T., & Yun, J. L. 1998, ApJS, 119, 59
- Launhardt, R. & Henning, T. 1997, A&A, 326, 329
- Launhardt, R., Pavlyuchenkov, Y., Gueth, F., Chen, X., Dutrey, A., Guilloteau, S., Henning, T., Piétu, V., Schreyer, K., & Semenov, D. 2009, A&A, 494, 147
- Launhardt, R., Sargent, A., & Zinnecker, H. 2001, in Astronomical Society of the Pacific Conference Series, Vol. 235, Science with the Atacama Large Millimeter Array, ed. A. Wootten, 134
- Launhardt, R. & Sargent, A. I. 2001, ApJ, 562, L173
- Launhardt, R., Sargent, A. I., Henning, T., Zylka, R., & Zinnecker, H. 2000, in IAU Symposium, Vol. 200, IAU Symposium, 103
- Launhardt, R., Ward-Thompson, D., & Henning, T. 1997, MNRAS, 288, L45
- Lee, C. W., Myers, P. C., & Tafalla, M. 2001, ApJS, 136, 703
- Lehtinen, K. 1997, A&A, 317, L5
- Lehtinen, K., Mattila, K., & Lemke, D. 2005, A&A, 437, 159
- Lemme, C., Wilson, T. L., Tieftrunk, A. R., & Henkel, C. 1996, A&A, 312, 585
- Lindblad, P. O., Grape, K., Sandqvist, A., & Schober, J. 1973, A&A, 24, 309
- Löhr, A., Bourke, T. L., Lane, A. P., Myers, P. C., Parshley, S. C., Stark, A. A., & Tothill, N. F. H. 2007, ApJS, 171, 478
- Lynds, B. T. 1962, ApJS, 7, 1
- . 1965, ApJS, 12, 163
- Mardones, D., Myers, P. C., Tafalla, M., Wilner, D. J., Bachiller, R., & Garay, G. 1997, ApJ, 489, 719
- Massi, F., Codella, C., & Brand, J. 2004, A&A, 419, 241
- Maury, A. J., Andre, P., Hennebelle, P., Motte, F., Stamatellos, D., Bate, M., Belloche, A., Duchene, G., & Whitworth, A. 2010, ArXiv e-prints
- Motte, F. & André, P. 2001, A&A, 365, 440
- Motte, F., Andre, P., & Neri, R. 1998, A&A, 336, 150
- Myers, P. C., Adams, F. C., Chen, H., & Schaff, E. 1998, ApJ, 492, 703
- Myers, P. C. & Ladd, E. F. 1993, ApJ, 413, L47
- Myers, P. C. & Mardones, D. 1998, in Astronomical Society of the Pacific Conference Series, Vol. 132, Star Formation with the Infrared Space Observatory, ed. J. Yun & R. Liseau, 173
- Neckel, T., Chini, R., Guesten, R., & Wink, J. E. 1985, A&A, 153, 253
- Neckel, T. & Staude, H. J. 1990, A&A, 231, 165
- Nutter, D. & Ward-Thompson, D. 2007, MNRAS, 374, 1413
- Olofsson, S. & Olofsson, G. 2009, A&A, 498, 455
- Orton, G. S., Griffin, M. J., Ade, P. A. R., Nolt, I. G., & Radostitz, J. V. 1986, Icarus, 67, 289
- Ossenkopf, V. & Henning, T. 1994, A&A, 291, 943
- Padoan, P. & Nordlund, . 2002, ApJ, 576, 870
- Parise, B., Belloche, A., Leurini, S., Schilke, P., Wyrowski, F., & Güsten, R. 2006, A&A, 454, L79
- Pavlyuchenkov, Y., Wiebe, D., Launhardt, R., & Henning, T. 2006, ApJ, 645, 1212
- Reipurth, B. 1983, A&A, 117, 183
- Reipurth, B., Heathcote, S., & Vrba, F. 1992, A&A, 256, 225
- Sandell, G. 1994, MNRAS, 271, 75
- Scappini, F. & Codella, C. 1996, MNRAS, 282, 587
- Scheepmaker, R. A., Lamers, H. J. G. L. M., Anders, P., & Larsen, S. S. 2009, A&A, 494, 81
- Sen, A. K., Mukai, T., Gupta, R., & Das, H. S. 2005, MNRAS, 361, 177

- Shirley, Y. L., Evans, II, N. J., & Rawlings, J. M. C. 2002, *ApJ*, 575, 337
- Simpson, R. J., Nutter, D., & Ward-Thompson, D. 2008, *MNRAS*, 391, 205
- Stecklum, B., Launhardt, R., Fischer, O., Henden, A., Leinert, C., & Meusinger, H. 2004, *ApJ*, 617, 418
- Stutz, A. M., Launhardt, R., Henning, T., Kainulainen, J., Krause, O., Linz, H., Nielbock, M., Steinacker, J., & André, P. 2010, submitted to *A&A*
- Stutz, A. M., Rieke, G. H., Bieging, J. H., Balog, Z., Heitsch, F., Kang, M., Peters, W. L., Shirley, Y. L., & Werner, M. W. 2009, *ApJ*, 707, 137
- Stutz, A. M., Rubin, M., Werner, M. W., Rieke, G. H., Bieging, J. H., Keene, J., Kang, M., Shirley, Y. L., Su, K. Y. L., Velusamy, T., & Wilner, D. J. 2008, *ApJ*, 687, 389
- Terebey, S., Vogel, S. N., & Myers, P. C. 1989, *ApJ*, 340, 472
- Testi, L., Palla, F., Prusti, T., Natta, A., & Maltagliati, S. 1997, *A&A*, 320, 159
- Tobin, J. J., Hartmann, L., Looney, L. W., & Chiang, H. 2010, *ApJ*, 712, 1010
- Turner, B. E. 1995a, *ApJ*, 444, 708
- . 1995b, *ApJ*, 455, 556
- . 1995c, *ApJ*, 449, 635
- Turner, B. E., Pirogov, L., & Minh, Y. C. 1997, *ApJ*, 483, 235
- Vallée, J. P., Bastien, P., & Greaves, J. S. 2000, *ApJ*, 542, 352
- van Leeuwen, F., ed. 2007, *Astrophysics and Space Science Library*, Vol. 350, *Hipparcos, the New Reduction of the Raw Data*
- Velusamy, T., Kuiper, T. B. H., & Langer, W. D. 1995, *ApJ*, 451, L75
- Vilas-Boas, J. W. S., Myers, P. C., & Fuller, G. A. 2000, *ApJ*, 532, 1038
- Visser, A. E., Richer, J. S., & Chandler, C. J. 2001, *MNRAS*, 323, 257
- . 2002, *AJ*, 124, 2756
- Vrba, F. J., Luginbuhl, C. B., Strom, S. E., Strom, K. M., & Heyer, M. H. 1986, *AJ*, 92, 633
- Wang, Y., Evans, N. J., Zhou, S., & Clemens, D. P. 1995, *ApJ*, 454, 217
- Ward-Thompson, D., André, P., Crutcher, R., Johnstone, D., Onishi, T., & Wilson, C. 2007, in *Protostars and Planets V*, ed. B. Reipurth, D. Jewitt, & K. Keil, 33–46
- Ward-Thompson, D., Chini, R., Krugel, E., Andre, P., & Bontemps, S. 1995, *MNRAS*, 274, 1219
- Ward-Thompson, D., Scott, P. F., Hills, R. E., & Andre, P. 1994, *MNRAS*, 268, 276
- Ward-Thompson, D., Sen, A. K., Kirk, J. M., & Nutter, D. 2009, *ArXiv e-prints*
- Whittet, D. C. B., Prusti, T., Franco, G. A. P., Gerakines, P. A., Kilkenny, D., Larson, K. A., & Wesselius, P. R. 1997, *A&A*, 327, 1194
- Wolf, S., Launhardt, R., & Henning, T. 2003, *ApJ*, 592, 233
- Wood, D. O. S., Myers, P. C., & Daugherty, D. A. 1994, *ApJS*, 95, 457
- Wu, Y., Huang, M., & He, J. 1996, *A&AS*, 115, 283
- Young, C. H., Shirley, Y. L., Evans, II, N. J., & Rawlings, J. M. C. 2003, *ApJS*, 145, 111
- Yun, J. L. 1996, *AJ*, 111, 930
- Yun, J. L. & Clemens, D. P. 1992, *ApJ*, 385, L21
- . 1994a, *AJ*, 108, 612
- . 1994b, *ApJS*, 92, 145
- . 1995, *AJ*, 109, 742
- Yun, J. L., Clemens, D. P., McCaughrean, M. J., & Rieke, M. 1993, *ApJ*, 408, L101
- Yun, J. L., Moreira, M. C., Afonso, J. M., & Clemens, D. P. 1999, *AJ*, 118, 990
- Yun, J. L., Moreira, M. C., Torrelles, J. M., Afonso, J. M., & Santos, N. C. 1996, *AJ*, 111, 841
- Zhou, S., Evans, N. J., Mundy, L. G., & Kutner, M. L. 1993, *ApJ*, 417, 613